Technische Universität München

TUM School of Natural Sciences

Chemically fueled self-assembly approach toward life-like materials

Michaela Angela Würbser

Vollständiger Abdruck der von der TUM School of Natural Sciences der Technischen

Universität München zur Erlangung einer

Doktorin der Naturwissenschaften (Dr. rer. nat.)

genehmigten Dissertation.

Vorsitz: Hon.-Prof. Dr. Richard W. Fischer

Prüfer*innen der Dissertation:

1. Prof. Dr. Job Boekhoven
2. Prof. Dr. Angela Casini

Die Dissertation wurde am 06.04.2023 bei der Technischen Universität München eingereicht

und durch die TUM School of Natural Sciences am 29.04.2023 angenommen.

I. Abstract

Nature displays countless unique biological systems that are ideally synchronized and optimized in functionality. By orchestrating complex regulatory mechanisms, biology exhibits sophisticated behavior, e.g., spatiotemporal control, adaptivity, information processing, or self-healing. Even though scientists progressively unravel underlying molecular mechanisms responsible for these unique properties, applying these mechanisms to design life-like materials on a synthetic level remains a major challenge.

Therefore, the thesis aimed to create life-like supramolecular materials based on a chemically fueled self-assembly.

In chapter one, I introduce my thesis with a selection of concrete and inspiring biological examples demonstrating essential functionalities of nature, e.g., responding, sensing, self-healing, and temporal control. It emphasizes how complex functions can evolve and that different mechanistic pathways can result in similar features.

In chapter two, I outline the aims of my thesis.

Chapter three focuses on designing a material with life-like behavior, e.g., a material that can be temporally controlled by displaying transient functionality. Chemically fueled self-assembly can be a versatile and accurate approach for inducing life-like behavior. The chemical fuel acts as an energy supply, enabling structure formation as long as fuel is provided. The energy supply can be accomplished directly or indirectly, i.e., based on dissipative self-assembly or self-assembly operating under dissipative conditions. By coupling the assembly and disassembly process to an energy-consuming reaction cycle, the assemblies and, thus, the material's lifetime is regulated by dictating activation and deactivation kinetics of the building blocks. Numerous cellular biological systems, like the GTP-driven microtubules, function based on this dissipative pathway. The energy-dependent nature is especially appealing for implementing temporal control since the fuel gives a first trigger to stimulate the assembly formation and, therefore, initiates a time-programmed function. The building blocks' deactivation results in the disassembly and, finally, the material's decay of function. A carbodiimide-driven reaction cycle has proven to be particularly powerful in creating a temporally controlled material. In chapter four, this concept was applied to form diblock copolymer micelles that can act as transient nanoreactors to accelerate a Diels-Alder reaction. Moreover, I selected the ability to self-heal upon external damage to design an adaptive and smart material. In chapter five, I introduce the first discoveries illustrating the inherent self-healing of artificial matter. I give a broad classification showing that, inter alia, self-healing can proceed autonomously, without any stimuli triggering the healing effect, or non-autonomously. Specifically, the design of intrinsically and autonomously self-healing materials has been a

main approach of material scientists over the last decades. Though they demonstrated self-healing materials based on healing agent-filled microcapsules, dynamic covalent bond formation, or supramolecular interactions, these systems showed restrictions and drawbacks, still far away from performing in a life-like manner. Therefore, chemically fueled self-assembly can be a tool to exert the ability to self-heal, as demonstrated by biological systems, such as microtubules, but also by one rare synthetic chemically fueled example. However, the underlying mechanism of how self-healing proceeds based on chemically fueled self-assembly remains unresolved. Hence, I present another artificial chemically fueled system that can self-heal after external damage (chapter six). This system showed strongly increased dynamic behavior in the case of damage and worked assumably with a chemically fueled supramolecular glue. By understanding the underlying mechanisms of chemically fueled self-healing, we may be able to narrow the gap between synthetic and biological systems and solidify the already existing conceptual knowledge.

In conclusion, this thesis demonstrates that life-like supramolecular materials can be developed using a chemically fueled self-assembly approach. By orchestrating activation and deactivation kinetics and the amount of fuel, the material's properties are transient, i.e., temporally controlled. This way, exciting materials like transient micellar nanoreactors can be designed. Furthermore, chemically fueled self-assemblies are inherently dynamic, making them a promising tool for creating self-healing features.

II. Zusammenfassung

Die Natur bringt einzigartige, biologische Systeme hervor, deren Funktionalitäten auf einem hohen Grad an Synchronisation und Komplexität basieren. Durch das Zusammenspiel komplexer Regulationsmechanismen zeigen sie ein ausgeklügeltes Verhalten wie beispielsweise räumlich-zeitliche Kontrolle, Adaptivität, Informationsverarbeitung oder die Fähigkeit zur Selbstheilung. Obwohl Wissenschaftler auf einem guten Weg sind, die zugrunde liegenden molekularen Mechanismen, die diese einzigartigen Eigenschaften hervorbringen, schrittweise zu lösen, bleibt die Anwendung dieser Mechanismen zur Entwicklung synthetischer, lebensechter Materialien immer noch eine große Herausforderung.

Das Ziel meiner Dissertation war daher die Entwicklung von supramolekularen Materialien mit lebensechten Eigenschaften, basierend auf einer chemisch-angetriebenen Selbstassemblierung.

Ich beginne daher meine Dissertation mit einer Auswahl konkreter und inspirierender, biologischer Beispiele, die wesentliche Funktionalitäten der Natur demonstrieren, zum Beispiel, Ansprechverhalten, Sensorik, Selbstheilung und zeitliche Kontrolle (Kapitel eins). Es wird gezeigt, wie sich komplexe Funktionen entwickeln können und dass verschiedene mechanistische Wege zu ähnlicher Funktionalität führen können.

Kapitel zwei führt die Ziele meiner Thesis auf.

In Kapitel drei verdeutliche ich, wie ein Material so konzipiert wird, dass es zeitlich gesteuert werden kann und eine zeitlich-begrenzte Funktionalität aufweist. Die chemisch-angetriebene Selbstorganisation, i.e., Selbstassemblierung, ist ein vielseitiger Ansatz zur Erzeugung von lebensähnlichen Verhalten. Der chemische Treibstoff dient hierbei als Energiequelle und ermöglicht die Strukturbildung, solange Treibstoff bereitgestellt wird. Die Energieversorgung kann direkt oder indirekt erfolgen, i.e., basierend auf einer dissipativen Selbstassemblierung oder einer unter dissipativen Bedingungen operierende Selbstassemblierung. Indem Aktivierungs- und Deaktivierungsprozesse an einen Energie-verbrauchenden Reaktionszyklus gekoppelt werden, können die Strukturbildung, und somit die Lebensdauer des Materials, reguliert werden. In zahlreichen biologischen Systemen, wie zum Beispiel den GTP-angetriebenen Mikrotubuli, basiert deren Funktionalität auf diesem dissipativen Prinzip. Dies ist besonders attraktiv hinsichtlich der Entwicklung eines temporär-kontrollierten Materials, da der Brennstoff eine erste Stimulation setzt, um die Selbstassemblierung in Gang zu setzen (Aktivierung der Bausteine). Es wird eine zeitprogrammierte Funktion eingeleitet. Die Deaktivierung der Bausteine führt zum Strukturabbau und schließlich zum Funktionsverlust des Materials. Ein Carbodiimid-getriebener Reaktionszyklus wurde als besonders vielversprechend evaluiert, um ein zeitlich-kontrolliertes Material zu kreieren.

In Kapitel vier wurde daher das zuvor erarbeitete Konzept auf die Erzeugung von Diblock-copolymermizellen angewendet, welche als zeitlich-begrenzte Nanoreaktoren zur Beschleunigung einer Diels-Alder Reaktion fungierten.

Die Fähigkeit der Selbstheilung nach Schaden wurde als Nächstes ausgewählt, um ein anpassungsfähiges und intelligentes Material zu entwerfen. In Kapitel fünf stelle ich die ersten Entdeckungen vor, die die inhärente Selbstheilung künstlicher Materialien veranschaulichen. Ich gebe eine grobe Einteilung, die zeigt, dass, unter anderem, Selbstheilung autonom stattfinden kann, oder nicht-autonom. Insbesondere die Herstellung von intrinsisch- und autonom-selbstheilender Materialien war ein Hauptansatz der Materialwissenschaft in den letzten Jahrzenten. Obwohl selbstheilende Materialien auf Grundlage von, zum Beispiel, mit Heilmittel gefüllten Mikrokapseln, der Bildung dynamischer, kovalenter Bindungen oder supramolekularer Wechselwirkungen, demonstriert wurden, zeigten diese Systeme Einschränkungen und waren zunehmend davon entfernt, lebensecht zu funktionieren. Daher kann die Treibstoff-angetriebene Selbstassemblierung ein Werkzeug sein, um die Fähigkeit zur Selbstheilung auszuüben. Dies wurde anhand von biologischen Systemen, wie den Mikrotubuli, aber auch durch ein seltenes, synthetisches, selbstheilendes Hydrogel veranschaulicht. Der zugrundeliegende Mechanismus Letzteres, wie Selbstheilung auf Grundlage einer Treibstoff-angetriebenen Selbstassemblierung abläuft, bleibt jedoch ungelöst. Daher stelle ich in Kapitel sechs ein synthetisches, Treibstoff-betriebenes System vor, welches sich nach Beschädigung selbst heilt. Durch das Verständnis der zugrunde liegenden Mechanismen der chemisch-angetriebenen Selbstheilung, könnten wir in der Lage sein, die Lücke zwischen synthetischen und biologischen Systemen zu schließen und das bereits vorhandene konzeptionelle Wissen zu festigen.

Diese Arbeit veranschaulicht, dass mithilfe von chemisch-angetriebener Selbstassemblierung lebensechte supramolekulare Materialien entwickelt werden können. Durch Orchestrierung von Aktivierungs- und Deaktivierungskinetik, sowie der Menge des Treibstoffes, wird das Material mit einer vorübergehenden Eigenschaft versehen, i.e., es ist zeitlich-kontrolliert. Materialien, wie z.B. zeitlich-begrenzte mizellare Nanoreaktoren, können somit kreiert werden. Chemisch-angetriebene Selbstassemblierungen sind zudem inhärent dynamisch und daher ideal, selbstheilende Eigenschaften vorzuweisen.

III. Abbreviations

A	alanine
AA	acrylic acid
ACN	acetonitrile
ADP	adenosine-5'-diphosphate
AIBN	2,2-azobis(2-methyl propionitrile)
Am	acrylic amide
AMP	adenosine-5'-monophosphate
ATP	adenosine-5'-triphosphate
BA	benzylamine
BCP1	blockcopolymer-1
Bz	benzoyl
c	concentration
$c_{sol.}$	solubility concentration
CAC	critical aggregation concentration
CAN	covalent adaptable networks
CD	cyclodextrin
CGC	critical gelation concentration
circa diem	about a day
CMC	critical micelle concentration
CoA	coenzyme A
Đ	polydispersity
D	aspartic acid
DA	Diels-Alder
DBZ	*N,N'*-dibenzoyl-L-cystine
DCC	*N,N'*-dicyclohexylcarbodiimide
DCM	dichloromethane
DCPD	dicyclopentadiene
DDMAT	2-(dodecylthiocarbonothioyl)-2-methyl propionic acid
DIC	*N,N*-diisopropyl carbodiimide
DGCBA	diglycidyl ether of bisphenol A
DIEA	diisopropylethylamine
DLS	dynamic light scattering
DMAP	4-dimethylamino pyridine
DMF	*N,N*-dimethylformamide
DMSO	dimethyl sulfoxide
DNA	deoxyribonucleic acid
D_f	degree of functionalization
E	glutamic acid
EDC	1-ethyl-3-(3-dimethyl aminopropyl)carbodiimide hydrochloride
e.g.	exempli gratia, for example
EMMA	poly(ethylene-*co*-methacrylic acid)
ESI-MS	electrospray ionization mass spectrometry
et al.	et alii, and others
F	phenylalanine or fuel
Fc	ferrocene
Fmoc	fluorenyl methoxycarbonyl
GDP	guanosine 5'-diphosphate
GTP	guanosine 5'-triphosphate
HPLC	high-performance liquid chromatography
HPP	hard polypropylene
i	intercalated

i	*iso*
I	isoleucine
i.e.	id est, that is to say
IFT	interfacial surface tension
k	reaction rate
$k_{hydrol.}$	hydrolysis rate
L	leucine
M	monomer
MD	molecular dynamics
Mebip	2,6-bis(1'-methylbenzimidalyl)pyridine
MES	2-(*N*-morpholino)ethane sulfonic acid
Mmt	monomethyoxytrityl
M_n	molar weight
MQ	MilliQ-water, double deionized water
NADH	nicotinamide adenine dinucleotide
NBD	nitrobenzooxadiazole
Nm	Newton meter
NMM	*N*-methyl morpholine
NMR	nuclear magnetic resonance
ns	nanoseconds
PA-F	polyamide furan
PA-MI	polyamide maleimide
PEG	poly(ethylene glycol)
P_i	orthophosphate
PS	polystyrene
r	reaction rate
RAFT	reversible addition-fragmentation chain transfer reaction
RP	reversed-phase
r_m	migration rate
R_t	retention time
SBS	poly(styrene-butadiene-styrene)
SEC	size-exclusion chromatography
t_0	starting time
T_g	glass transition temperature
$t_{migrat.}$	migration time
T_v	freezing transition temperature
TACN	triazacyclononane
TCEP	tris-(2-carboxyethyl) phosphine
TEM	transmission electron microscopy
TFA	trifluoroacetic acid
TIPS	triisopropylsilane
UPy	ureidopyrimidone
UV	ultraviolet
v	volume
W	waste
W_t	width over time
$W_{t=0}$	width at t_0
Y	tyrosine

IV. Table of contents

1 Materials science: Learning from biology

Abstract

Life responds, senses, adapts, regulates in a spatiotemporal manner, self-replicates, processes information, self-heals, and acts autonomously. The list of functions that living systems exert is as versatile as mesmerizing. Although we make a great effort to understand how biological functions emerge and solve fundamental principles, realizing artificial life-like materials remains challenging. Nature provides a medley of nearly perfectly orchestrated and regulated processes and demonstrates that functions originate in the urge to reproduce, ensure long-term competitiveness, and sustain their existence. Biology also shows that function can be realized through several mechanisms or pathways. Before we can design and create materials mimicking life-like features in an equal manner, we first need to have a close look at conceptual requirements and guidelines directly conveyed by biology. This way, we might be rewarded by learning from living systems, e.g., a pinecone or a salamander.

1.1 Concepts of living systems

"Taking lessons from nature on our next journey into uncharted territories of molecular materials, we cannot avoid dreaming about the astonishing way living systems sense, function autonomously and respond to their environment". Ben Feringa[1]

This statement made by Nobel Laureate Ben Feringa outlines what material scientists have aimed for ever since: How to mimic living organisms with their plethora of sophisticated features and principles. But it also clarifies the current state of possibilities and foremost restrictions we are yet confronted with in material science. Indeed, we can merely dream about, though still not rudimentarily understand how living systems sense and respond to their environment, communicate with it, process the received information, and consequently (re)-act autonomously. That way, nature secures its existence by self-controlling its conditions, healing in case of traumas, and self-replication. By unraveling underlying mechanisms and discovering how self-regulated processes dictate life, we can create materials inherently possessing life-like features. Hence, according to which concepts does nature utilize, and more importantly, what can it teach us in designing life-like materials? Although nature provides a variety of nearly perfectly orchestrated functions and conditions, the systems differ in underlying concepts, consequently yielding functionalities with a varying degree of complexity. In the following, I describe selected functions of biological examples (with different complexity) that demonstrate how life can function, e.g., respond, sense, self-heal, or temporally regulate, and which lessons it can hold for us.

Responsive as a pinecone. Natural hygromorphs are systems able to respond to humidity changes in the environment, reacting with shrinkage or swelling of their system, specifically of their tissue structure.[2] Examples include the dwelling of specific mosses, curling of drying leaves on the ground, or seed-dispersing wheat awes. But one of the most robust and active hygromorphs represents a pinecone (*strobilus*).[2, 3] Pinecones are in a closed state while hanging on the tree, in contrast to their open structure if fallen off (dried state). This way, the increased humidity suggests favorable growth and reproduction conditions resulting in the preservation of the cone kind. Interestingly, if the already opened and dried cone is moved to a surrounding of high humidity, e.g., by wetting, it closes again. This open-close actuation mechanism occurs through a humidity-triggered swelling of hygroscopic bilayers provoking an anisotropic actuation response.[4, 5] This hygroscopic response significantly depends on the geometry of the tissue structure and, thus, on the evaporation rate or water intake based on capillary forces in tissues. Though this is a gradual process, since the needed energy for this motion is achieved by the uptake of water (and thus linked to mass transport), a sharp on-off response could be possible in synthetic doubly-curved bilayer-structures.[6, 7]

Sensing as a fly trap. The endemic carnivorous Venus fly trap (*Dionaea muscipula Ellis)* depicts a system consisting of such a shell-like layer.[2] It sustains its existence by eating living insects it captures by immediate closure of a trap: Only 100 ms is needed to close its trap, constituting one of the quickest motions in the whole plant kingdom.[4] Although rapid movement is not an outstanding feature of most plants, it is an important trade for, e.g., seed and pollen dispersal, resistance, or as in the case of the Venus fly trap, nutrition.[4] The closing process is performed in three main steps: 1) a restrained phase exerting no movement, 2) a fast movement of the leaves and 3) the relaxation of the leaves returning to the closed state. In specific, trap closure occurs according to a contact-induced provoke of trigger hairs located at the upper leaf epidermis.[8] Triggering of the hairs leads to an activation of mechanosensitive ion channels, initiating a receptor potential and consequently causes an action potential (and thus an electrical one).[9] Mechanosensitive channels appear in a variety of cells, e.g., animal, plant, fungi, or bacteria, and transduce sensed physiologically important mechanical forces or stimuli into electrical signals.[10] At this state, the source of the trigger can be a mechanical or electrical one; both create an electrical potential leading to further actuation of the system.[11, 12] On an energetic level, the closed state can be considered as the equilibrium state compared to the open state being a metastable one.[12] This is presumably caused by the high elastic energy as a consequence of the difference in hydrostatic pressure between the hydraulic layers at the leaf edge. The contact with an insect stimulates a signal leading to the opening of the water pores between these layers, causing a configurational change and the relaxation to the preferred energy-low, equilibrium state. Not less fascinating is that the sensed contact and, thus, signal input are temporally connected to a form of information processing.[5] For instance, at room temperature, two contacts with the sensory hairs within a certain time window will lead to closure. Though the purpose serves to maintain appropriate closure as, e.g., a stronger breeze would lead to unsuccessful prey capture and a waste of energy, it demonstrates the presence of an electrical memory and the ability to process incoming signals in a defined temporal frame. Specifically, the Venus fly trap cannot be considered to function in simply a sensing manner, but overall presents an adaptive system that senses, responds, and processes incoming information.[12]

Self-healing as a salamander. Living organisms ensure their existence and longevity not only by reproduction and environmental adaption but also by the ability to restore damage or fatigue through self-healing. Some organisms take this to the extreme. For instance, the salamander Axolotl or "water monster" (*Ambystoma mexicanum*), shows excellent regeneration potential in completely healing full body parts, e.g., limbs, or the spinal cord, even far after the child stage.[13-15] Ever since the last 250 years, scientists have shown great interest in the self-restoring ability of salamanders, though being probably not one of the most common or

straightforward self-healing processes to be identified. However, due to the salamander's great similarity to human limbs, regenerative medicine could gain insight into the underlying self-restoring principles by using them as a powerful regeneration model. The healing proceeds as follows: After amputation of, e.g., the salamander's limb, self-healing is initiated by blood clotting and coverage of the cut stump with epithelial cells.[16] Next, these cells, as well as cut vascular and nerve systems at the connection plane, send molecular signals or cues to migrate fibroblasts, cells that produce extracellular matrix, to the center of the wound. Immune cells additionally supervise the removal of the damaged matrix on the connection plane.[14] On this now cleaned area, proliferation (multiplication) starts forming the blastema, an organization of cells able to regenerate and re-grow matrix and a progenitor of a new limb.[17] This blastema initiates re-organization and differentiation resulting in a newly grown limb. Whereas previously it was assumed that blastema solely consists of undifferentiated pluripotent cells (a form of regenerative cells), recent research indicates that the salamander's unique self-regenerating ability is grounded in the re-programming of cells at the amputation site, allowing them to enter an embryonic-like stage of tissue formation.[16] If the limb blastema was transplanted to other receptive areas of the body, limb growth would be pursued there.[18, 19] This emphasizes that the blastema acts as an autonomous segment capable of regenerating entire body parts. The underlying concepts of how these regenerative processes work have not been fully described yet. However, tissue regeneration is assumed to occur according to multiple synchronized processes based on temporally regulated bioactive cues combined with spatiotemporally regulated extracellular matrix guiding cells to perform functions, e.g., migration, adhesion, multiplication, or differentiation.[20]

Temporal regulation as in circadian clock cells. The earth rotates daily around its axis, the moon monthly rotates around the earth, and the earth annually orbits the sun. These are just a few examples of how living systems are surrounded by a diversity of periodic events. These events are coherently related to or induce fluctuations in the environment. Not surprisingly, biological systems show preferred or restricted activity depending on the state of these periodic circumstances. To enhance the adaption of organisms to these periodic events, every living organism, eukaryotic or even procaryotic nature, inherently owns a significant temporal program, the so-called "circadian" clock (*circa diem* – about a day).[21 22 23] These clocks are said to be as old as the earth's geological history, depicting an autonomous oscillating system emerging 24-hour-rhythms.[24] Specifically, they orchestrate physiological processes, e.g., sleep rhythm and food intake, or metabolic processes, e.g., glucose degradation in living systems.[25] Thus, they enable the organisms' adaptivity to environmental changes, e.g., temperature, light, or humidity, enhancing the survival of the system, which is referred to as homeostasis. For instance, various insects perform eclosion, the transformation from pupal to adult stage, or

actions of high activity mostly during dawn, when humidity is the greatest.[21, 26, 27] Based on circadian rhythm, migratory birds, e.g., the European Starling, do not lose track of their climatically favorable location, despite the obstacle of quickly changing day lengths and the constantly changing position of the sun.[28] This concept was excessively studied on a cellular and genetic level, demonstrating that cells themselves are a complex organization of clock machinery.[23] Scientists assume that molecular clocks or oscillators genetically encode circadian periodicity within almost every cell.[29] Subordinately, these molecular clocks are instructed by a master clock network (core oscillator) found in the suprachiasmatic nucleus of the hypothalamus.[30] The molecular oscillators regulate circadian rhythm using multiple feedback loops based on an auto-regulatory transcription-(post)-translation process. These transcriptional genes and proteins oscillation behave according to a 24-hour periodicity without external triggers.[23, 31-33] For instance, repairing UV-damaged DNA based on the nucleotide excision restoration pathway is preferred during the late afternoon and early evening rather than before dawn.[29] This rhythm is temporally controlled by the circadian periodicity using xeroderma pigmentosum A protein expression.[34, 35] On the one hand, the oscillation is actuated by transcriptional control by cryptochrome and further clock proteins. On the other hand, it is enabled by proteolysis according to the ubiquitin-proteasome process.[34] The deep understanding of circadian clock rhythm in living systems, especially on a cellular level, could help to enhance, e.g., chrono chemotherapeutical approaches, which already consider that uptake or known side effects of chemotherapeutical drugs are known to be influenced by circadian factors.[34]

1.2   Conclusion and outlook

The highlighted examples caught a mere glimpse of the rich abundance nature holds in functionality on different levels. The presented concepts particularly differ substantially in the type of function, complexity, and implementation but can serve as a fundamental inspiration for designing synthetic-based materials owning life-like properties. Life combines and orchestrates essential key-features, e.g., self-regulation, temporal control, adaptivity, autonomy, motion, or information processing. In living systems, these essential key features inherently rely on non-equilibrium processes and thus require the input of an energy source to occur. This input of energy can be realized, for example, via the conversion of chemical fuels, e.g., ATP and GTP. Biology uses chemical fuels to control where and when functions, such as self-assembly or other processes, need to be regulated, i.e., spatiotemporally controlled. After highlighting the aims of this thesis, I, therefore, introduce the concept of chemically fueled self-assembly and demonstrate how it can be applied to control a system temporally.

2 Aims of the thesis

The overreaching goal of this thesis was to create supramolecular materials that display life-like features by introducing a fuel-driven chemical reaction cycle to the self-assembly process. Life itself beautifully demonstrates versatility in function. Although we are well on track to understanding these biological principles, we are still limited in applying them and endowing synthetic materials with comparable life-distinguishing properties.

In chapter one, I thus introduced concepts of living systems that could serve as inspiration for synthetic approaches in order to design materials with unique life-like behavior. The different examples demonstrated the range in complexity and that diverse mechanisms could result in similar properties.

One prominent biological system that achieves great functionality are the cellular microtubules which are regulated by a chemically fueled reaction cycle while depending on non-equilibrium dynamics. Therefore, in chapter three, I focused on energy dissipative self-assembly, and in specific, chemically fueled self-assembly. Establishing a fuel dependence on the self-assembly and material formation process increases the dynamic nature of the system and enables the emergence of life-like properties, e.g., to induce temporal regulation. By coupling the self-assembly process to an energy-transducing step, building blocks are activated, leading to self-assembly. The building blocks' deactivation results in the material's disassembly and decay of its function, providing the fuel's depletion. Hence, the material behaves transiently, i.e., has a tunable lifetime. Numerous man-made examples of chemically fueled systems displayed how the lifetime could be tuned or temporary domains induced by the amount of fuel. I selected a carbodiimide-driven approach as the reaction of choice since it is characterized by its simplicity in application and high liberation of chemical potential by a building block.

Chapter four dealt with the first aim of my thesis, designing transient micellar nanoreactors by demonstrating temporal control on the self-assembly of a diblock-copolymer under fuel consumption. That way, we not only sought temporal control of the assembly but also could give one of the first examples of fuel-driven self-assembly of a block-copolymer activating multiple building blocks within one polymer strain. Excitingly, the transient micelles could up-concentrate reagents and work as nanoreactors for, e.g., a Diels-Alder reaction. In the end, not only the transient nature of the micelles but also the conversion of Diels-Alder reagents were regulated by the fuel concentration.

We extended the concept of temporally controlling assemblies and lifetimes and aimed to design an adaptively behaving material with self-healing ability. I gained insight into early discoveries of presumably inherently self-healing artificial materials in chapter five. Herein, I compared intrinsically and extrinsically self-healing or autonomously versus non-autonomous

healing behavior. I then presented state-of-the-art materials that showed different degrees of ability to self-heal, based on, e.g., micro-encapsulation, dynamic covalent bond formation, and non-covalent interactions. Though it became clear that dynamic structure formation is a key element in self-healing, creating self-healing materials comparable to biological systems remained challenging. Chemically fueled self-assembly intrinsically possesses dynamic behavior caused by the constant activation and deactivation of building blocks and, thus, could be a promising approach to induce self-healing.

Therefore, in chapter six, I aimed for a chemically fueled fibrous hydrogel that self-healed without showing assembly or disassembly dynamics in the undamaged state. We designed the system being supplied by a pseudo-steady state of fuel and activated building blocks and hypothesized the healing effect due to a concept of a chemically fueled molecular glue in combination with an increased nucleation site number. This concept was also generalizable for other peptides, showing a significant relationship between the peptide's critical aggregation concentration and the self-healing efficiency.

In conclusion, this work focused on using chemically fueled self-assembly as a promising tool to create materials with unique features inspired by nature, e.g., temporal control and self-healing. I specifically demonstrated how the lifetime of block-copolymer micelles was fuel-dependently tuned and how they served as nanoreactors for, e.g., Diels-Alder reactions. Furthermore, by adjusting a pseudo-steady state of fuel, a fibrillar system of static nature turned dynamic in case of external damage and was able to self-heal. The approach of coupling self-assembly to a chemical fuel dissipation could give an insight into how the self-healing mechanism proceeds and define hallmarks for other fascinating nature-inspired properties leading to dynamic, learning, or interacting materials.

3 Approaches toward temporally controlled materials

Abstract

As previously stated in chapter one, biological systems hold many unique properties and features with underlying principles and concepts waiting for us to unravel. These life-like properties, such as having temporal control over structure formation or exertion of functionality, display a fundamental key feature for the emergence of even more sophisticated biological behavior. In the following chapter, I closely look at which fundamental circumstances and hierarchical networks drive life-like properties and, specifically, how to induce temporal domains into a self-assembly process. I demonstrate that operating out-of-equilibrium based on a chemically fueled reaction cycle is worth adopting on a synthetic level. Though there are many options to transduce energy, energy liberated from chemical fuels, e.g., GTP as in the self-assembly of microtubules, depicts a promising choice. Herein, the dissipation of chemical fuel is coupled to chemical reaction networks guided by activation and deactivation steps. By dictating the reactions' kinetics, i.e., kinetically controlling the assembly, the material is provided with a specific lifetime and, thus, transient character. I set the presented dissipative approach with respect to other man-made dissipative systems inducing temporal control. Finally, I present a chemical fuel-driven strategy of choice, particularly to temporally control materials based on a carbodiimide-driven self-assembly process.

3.1 Dissipative out-of-equilibrium self-assembly

Most structure and matter formation in biology rely on molecular self-assembly.[36] Molecular self-assembly represents the spontaneous and reversible association of molecules into supramolecular structures and networks driven by non-covalent interactions, e.g., hydrogen bonds, π-π-stacking, hydrophobic interactions, and so forth.[37-39] Classical self-assembly processes proceed in equilibrium, enabling a reversible process resulting in the energetically most minimized and thermodynamically favored structure. Furthermore, self-assembly is a powerful tool to create materials under thermodynamic control, e.g., consisting of a mixture of different building blocks.[40, 41]

However, in- or close-to-equilibrium states do not meet the requirements for the existence of life, i.e., the redistribution of energy sources and, foremost, emerging complex functions.[42, 43] Living organisms, such as cells, adhere, contract, differentiate, divide, or move, and run processes in an adaptable manner and under constant regulation. A plethora of reaction networks in cells functions according to an energy-consuming, so-called dissipative process, sustaining the desired state by operating according to an out-of-equilibrium pathway.[44] This is a clever trait of nature. By coupling their functions to the consumption of energy, i.e., chemical fuel or light, the systems remain dynamic and foremost active and adaptable to changes. In the case of converting chemical fuel to waste, or in other words, converting molecules having a high chemical potential into molecules with a lower one, is the energy-transducing process. This is a significant and crucial distinction from static systems which rely on in-equilibrium dynamics. The dependence on a steady energy consumption gives biological systems control over assembly formation and, thus, their functions by kinetics rather than by thermodynamics. In other words, the properties of an assembly, like its scale, morphology, or function, depend on the kinetics of the energy dissipation. Although the operation in out-of-equilibrium states is thermodynamically unstable and costs energy, it is an essential tool for biology to respond rapidly to an external trigger.

3.1.1 Dissipative self-assembly and self-assembly under dissipative conditions

In general, a self-assembly process can be coupled to an energy-consuming chemical reaction cycle by starting from a simplified self-assembly process as follows: a monomer M can self-assemble into the assembled structure M_n, but this is thermodynamically not preferred, shifting the equilibrium to the dissolved, monomeric state (equation 1).[45]

$$n \cdot M \; \underset{\longleftarrow}{\overset{\rightarrow}{\rule{2cm}{0pt}}} \; M_n \tag{1}$$

The precursor can be activated for assembly by applying a fuel F, resulting in the activated product M*. The fuel F has a high chemical potential (μ_F) and converts into the waste analog W with a low chemical potential (μ_W) (equation 2).

$$n \cdot M + F \longrightarrow n \cdot M^* + W \qquad (2)$$
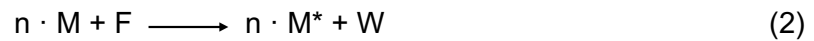
Herein, $\Delta\mu$ is equivalent to the transduced energy needed to push the system out-of-equilibrium and to form the assembly M_n^* (equation 3). In the case of light as an energy source, no waste is produced in contrast to a chemical fuel approach.

$$n \cdot M^* \; \underset{\longleftarrow}{\longrightarrow} \; M_n^* \qquad (3)$$

A deactivation process leads to the conversion of the activated monomer into its monomeric state (equation 4).

$$M_n^* \longrightarrow M_n \qquad (4)$$

Finally, disassembly occurs, resulting in the monomeric state (equation 1).

The self-assembly process can either be dissipative or under dissipative conditions depending on if all energy is dissipated by the monomeric building blocks or by an external component (also referred to as direct vs. indirect dissipative self-assembly).[46-48] The latter case implies a self-assembly process with the building blocks not relying on or participating in energy conversion to mediate the assembly process. In other words, there is no activation of building blocks by the supplied energy in total. Still, energy is consumed by external additives, e.g., enzymes, leading to the assembly formation (or initiating its slow decay). For instance, Liu and co-workers demonstrated a conformational switch of i-motif DNA under light-induced conditions according to a pH-responsive system.[49] Herein, a pH-jump is induced by UV-irradiation of the photobase malachite green (located in solution), resulting in the release of hydroxide ions. Consequently, the cytosine-cytosine base pair formation of the i-motif structure is deprotonated with increased pH, leading to a conformational change and the loss of the tightly packed four-stranded structure. Removing irradiation leads to the reversible reaction of the hydroxide ion with the photosensitizer (photo-switch) and to the return of the DNA's initial conformation. This example stresses two essential points: On the one hand, this system clearly differs from conventional acid/base trigger systems since the change in structure is indirectly coupled to the absorption of light and is sustained as long as energy is supplied. More importantly, it shows that the dissipative manner is implemented in the photo-switch behavior

of the malachite green, working as an active environment rather than an active structural building block.

In the case of dissipative self-assembly, the self-assembly process directly depends on the energy conversion by the building blocks resulting in the monomer's activation. The activated monomers assemble, as this is now a kinetically favored process. Vice versa, a back-reaction converts the activated building blocks to the initial monomeric state. Grzybowski et al. illustrated several examples of light-induced self-assembly based on azobenzene-functionalized gold nanoparticles.[50, 51] UV-irradiation of the nanoparticles leads to isomerization of the azobenzene-units from *trans* to *cis* form. The change in polarity results in the nanoparticles' self-assembly. Hence, light is directly consumed by the photosensitive azobenzene-functionalized particles guiding the self-assembly process as an actively triggered structural component.

3.1.2 Chemically fueled self-assembly

Though light as an energy source brings benefits, e.g., no waste production, non-invasiveness, or high precision, nature mostly operates under the conversion of chemical fuels.[45] For instance, GTP hydrolysis to GDP is used by microtubules, but also ATP, NADH, or acetyl-CoA act as the most prominent and essential chemical fuels in biological systems. Herein, the fuel having a high chemical potential is converted into waste with a low chemical potential by a catalytic reaction cycle. Thus, the gained energy can develop highly sophisticated systems with complex functions, e.g., a spatiotemporal regulated self-assembled system.[46] The diversity of fuels and the possibility to over-fuel (this is impossible with light), make chemical fuels especially attractive to creating high-end functionality.

To design chemically fueled reaction cycles, certain criteria need to be considered.[48, 52] On the one hand, the selected fuel should possess high kinetic stability while being, in turn, thermodynamically unstable. This means, in the absence of the chemical reaction cycle, the fuel is relatively stable and thus hardly converts to waste. For instance, ATP has a high chemical potential and hardly hydrolyzes to ADP without a catalyst, showing a half-life of around 175 hours (pH 8, 25°C).[53] However, an additional enzyme, e.g., ATPase can be applied as catalyst to accelerate the hydrolyzation process. Moreover, the chemically fueled reaction cycle must have at least two reaction steps, activation and deactivation (Figure 1). During the activation process, the not yet assembled building blocks or monomers act as catalysts for fuel-to-waste conversion and are thus activated by fuel. This can happen either non-covalently or covalently bound. The activated catalytic building blocks are reverted to the initial monomers in the deactivation. Several dissipative self-assembled systems worked according to this concept, operating based on phosphorylation and dephosphorylation, transacylation, or

reduction/oxidation of the catalyst.[54-59] The energy liberated by the fuel-to-waste conversion is used for the immediate activation of molecules, bringing them to a higher level of chemical potential.

In conclusion, chemical fuels are the energy source of choice due to their versatility in molecular design and possible fine-tuning of energy liberation, as opposed to light. By coupling self-assembly with dissipative chemical reaction networks, the kinetics of activation and deactivation of the self-assembling building blocks can be controlled and, therefore, the material's transient character. Key elements are to understand and evaluate transferred/transduced chemical energy. That way, synthetic highly functional materials owning life-like features, e.g., temporal regulation, might be feasible.[46]
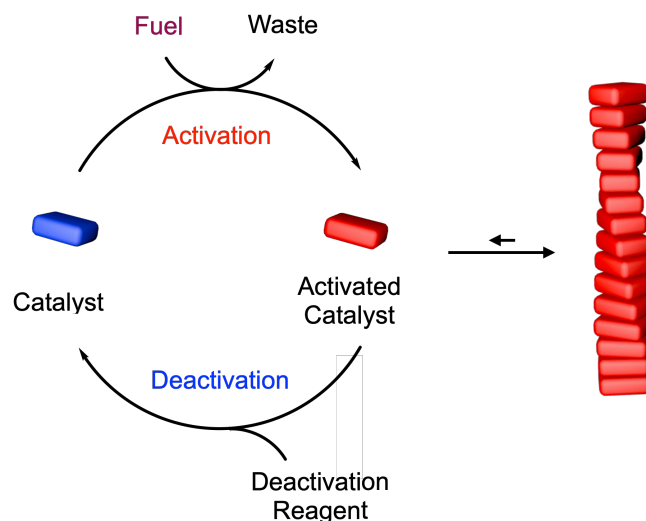
Figure 1: Chemically fueled self-assembly via activation and deactivation of a catalyst. The catalyst serving as a building block is activated under fuel-to-waste conversion. The activated catalyst unit self-assembles due to a change of interactions. A deactivation reagent deactivates the activated species resulting in the disassembly of the structure.

3.1.3   Chemically fueled self-assembly in biology

One of the most prominent biological examples of chemically fueled self-assembling systems demonstrating spatio-temporal control is the cytoskeleton, a highly dynamic and spatially organized fibrillar network residing in the cytoplasm of eukaryotic cells.[60, 61] It comprises regulatory proteins and three main polymeric filaments, e.g., microtubules, actin filament, and intermediate filament structures.[62] The interplay of all three sub-structures enables the regulation of the cell shape and essential mechanical features. For instance, these filaments can withstand deformation while, on the other hand, can re-structure after an external mechanical trigger, thus assisting in the integrity of intracellular segments.[63] Moreover, they

guide structural changes during movement and instruct the transport of intracellular building blocks, e.g., organelles or vesicles.[64] Microtubules, the largest of these filaments, are one of the most prominent biological models performing work and function based on dissipative (or chemically-fueled), out-of-equilibrium self-assembly.[62, 65] Moreover, they own the ability to self-heal (for a detailed discussion, see 5.3.4).[61, 66] The microtubule's network consists of a hollow cylindrical structure based on 9 to 16 laterally combined protofilaments, so-called $\alpha\beta$-tubulins, or hetero-dimeric proteins.[63] The microtubules' highly dynamic behavior and functionality is a consequence of the structure's polymerization and depolymerization process, which is also referred to as dynamic instability. This dynamic instability is based on the structure's stable growth and rapid destruction as a result of energy consumption coupled to the hydrolysis of guanosine 5'-triphosphate (GTP) to guanosine 5'-diphosphate (GDP) (Figure 2).
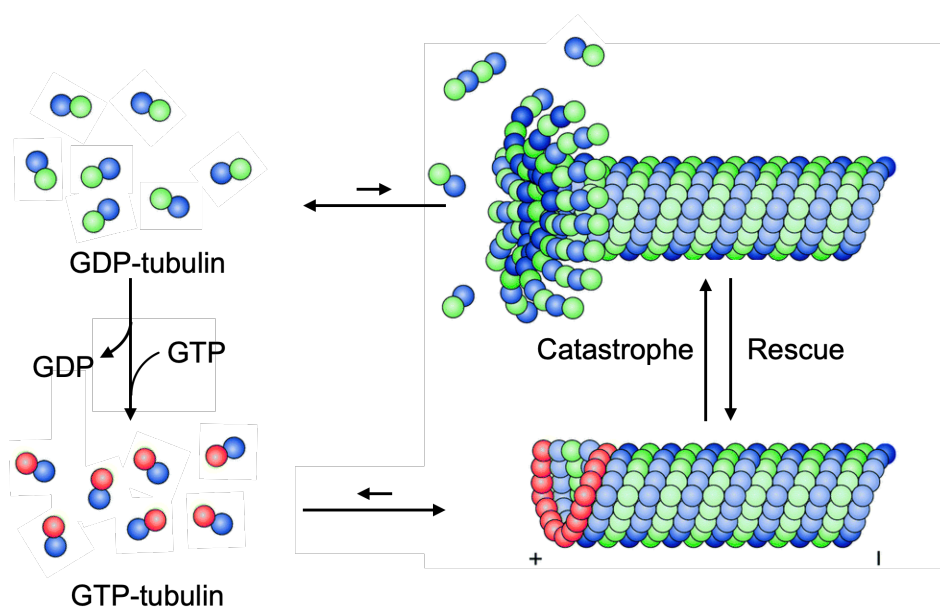
Figure 2: Schematic presentation of a microtubule's self-assembly and disassembly process driven by the conversion of GTP to GDP. Reproduced with permission from ref. 25. Copyright 2017 Royal Society of Chemistry.

This emerging dynamic instability is critical for several cellular processes and enables the microtubules' contribution as, e.g., DNA-segregating motor during mitosis (segregation of chromosomes during cell division).[67, 68]

The assembly and disassembly processes undergo four different kinetic states: growth or elongation (1), catastrophe (2), shortening (3), and rescue (4).[63] Initially, α-β-tubulins are activated through complex formation with GTP and subsequently self-assemble into the microtubular structure (1). This stands in contrast to GDP-bound α-β-tubulins which are not likely to be incorporated into the microtubular formation. The hydrolysis of GTP to GDP is

favored and accelerated in the assembled state (specifically in the inner part of the microtubules), resulting in a microtubular assembly containing mostly GDP-dimers. The activation of GDP monomers and their subsequent self-assembly leads to a highly energized state and, therefore, to a thermodynamically unstable system.[69, 70] Simply, the GTP-rich cap at the end of the microtubule hinders its disassembly. As the hydrolysis reaches the tip of the tube, a catastrophic collapse (2) occurs, resulting in the structure's disassembly and shortening (3).[25] Although the mechanism of the re-growth process (4) is still unknown, recent studies assume that randomly distributed areas of concentrated GTP-tubulins within the microtubules might be plausible.[71]

The discussed biological example of microtubules led to an important conclusion: Relying on dissipative, out-of-equilibrium pathways requires coupling structure formation processes to energy consumption. As long as fuel is available, the process is driven out-of-equilibrium, and the structure will grow. Once the fuel is depleted, the out-of-equilibrium species decay and is reverted to the thermodynamically more stable component. In the case of microtubules, stopping the fuel supply would finally lead to the decay of the assembled structure. From a material science point of view, one learned lesson is that coupling energy transducing reaction steps, such as conveyed by GTP to GDP hydrolysis, to structure formation can be considered a key feature to implement functions, e.g., temporal control, adaptivity, or self-healing into a material. The thus occurring dynamic instabilities and dynamic steady states achieved by coupling energy-transducing reactions to structure formation seem to be a waste of energy at first sight but are an essential element of nature in order to rapidly adapt or operate. Hence, it could be decisive guidance for synthetic approaches to design materials that are, for instance, temporally controlled in their functionality.[5, 56, 72]

3.2   Temporal control over material properties

Temporal control of structure formation or function is more the rule than the exception in biology. For instance, temporally controlling the cytoskeleton's filaments' self-assembly increases the cell's adaptability to external influences, e.g., resulting in the cytoskeleton's motility. Like in biology, the temporal control over synthetic supramolecular materials enables, for example, time-dependent structure transitions and/or transient behavior in functionality. Hence, the material itself, i.e., its lifetime and, specifically, the materials' functionality, gets programmable and predictable. Conceptual requirements, including a minimum of two stimuli acting divergently, must be applied to a system to introduce time control, e.g., a transition in structure and a change in functionality (Figure 3).[56] Initially, a positive trigger is in charge of activating the self-assembly process; a delayed second trigger stimulates the deactivation and,

consequently, the disassembly. The lifetime of the assembly (material) equals the time frame of activation and effectively operating deactivation.
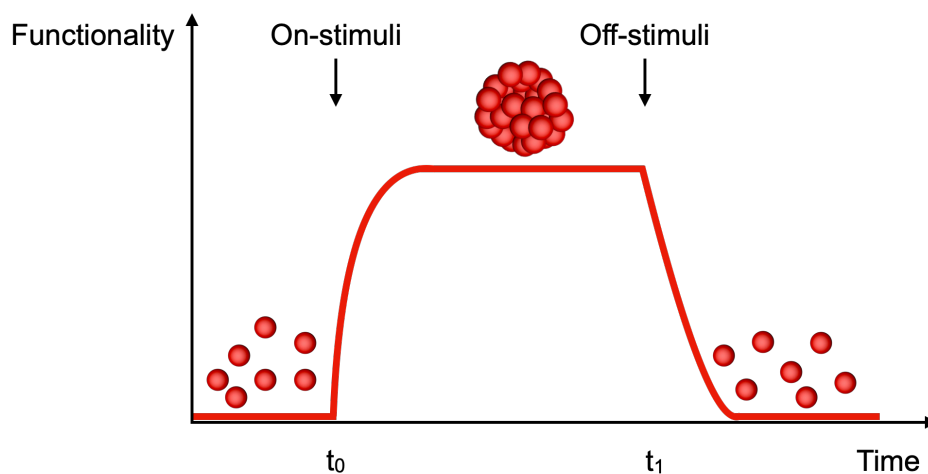

Figure 3: Temporally control over self-assembly based on an on/off-trigger. A trigger stimulates the activation of the building blocks, a second one deactivates the building blocks resulting in disassembly. The material can be endowed with a function over a specific time range. Reproduced with permission from ref. 25. Copyright 2017 Royal Society of Chemistry.

3.2.1   Temporal control via self-assembly under dissipative conditions

For temporal control over material properties under dissipative conditions, biocatalysts, e.g., enzymes, have been proven efficient in modulating assembly and disassembly kinetics.[59] One example of self-assembly under dissipative conditions is shown by Prins and co-workers. Inspired by biological systems, e.g., ATP-driven actin assembly, they used potato apyrase to control the ATP-driven vesicle formation of the surfactant $C_{16}TACN$ Zn^{2+}.[55] ATP, on its own, acts as the chemical fuel regulating the self-assembly of the surfactant $C_{16}TACN$ Zn^{2+} into vesicles. On the other hand, adding ATP under the biocatalytic aid of potato apyrase, i.e., an ATP-catalyzing enzyme, led to the hydrolysis of ATP to adenosine 5'-monophosphate (AMP) and two molecules of orthophosphate (P_i) resulting in the vesicles' disassembly. Therefore, the vesicles were transient and the vesicles' lifetime could be regulated by the kinetics of free ATP hydrolysis (k_{ATP}) in competition with vesicle-bound ATP ($k_{ATP-ves}$). This introduced transience, and dynamism makes them an ideal candidate for the application as, e.g., transient nanoreactors.

Walther and co-workers gave another example of self-assembly under dissipative conditions, coupling responsive assemblies to an active environment based on enzyme-controlled self-assembly.[73] Herein, they catalytically regulated time domains of a pH-responsive peptide hydrogelator (Fmoc-LG-OH) by creating transient pH profiles using a urea/urease switch combined with an acidic buffer. At low pH, the protonated Fmoc-LG-OH self-assembles into a

hydrogel due to the loss of electrostatic repulsion. While the acidic buffer serves as an activator, i.e., initiating self-assembly, the enzymatic conversion of the dormant deactivator urea results in the fresh generation of the base ammonia (acting as the active deactivator), leading to a pH rise and the hydrogel's disassembly. In contrast to the fast activator, the enzymatic activity is lowest at high and low pH (pH <3. 5 or pH >9). This means the system is activated from the low activity state at pH = 9 into the higher activity level after adding the acidic buffer. Hence, the production rate of the active deactivator is directly dependent on the enzyme concentration, enabling fine-tuning of the reaction rates and, thus, the design of hydrogels with a programmable lifetime. Due to the reaction rate tuning and time control, it makes it especially appealing regarding microfluidic guidance or burst release.

3.2.2   Temporal control via dissipative self-assembly

In contrast to self-assembly under dissipative conditions, the activation of the monomeric building blocks is directly coupled to a chemical reaction network for dissipative self-assembly. These chemical reaction networks consist of at least two irreversible chemical reactions that activate and deactivate a monomer.[48] As a consequence, the system exhibits dynamic self-assembly, an interplay of elongation of the assembly due to pushing the system out of equilibrium and occurring disassembly towards equilibrium adjustment.[59] Thus, the resulting system is of transient nature. Van Esch and co-workers reported one early example of synthetic dissipative self-assembly of soft matter.[74] Herein, methyl iodide (MeI) acts as fuel to activate the pH-responsive hydrogelator *N-N'*-dibenzoyl-L-cystine (DBZ) by double alkylation (Figure 4A + B). The decrease in electrostatic repulsions from the diacid to the diester form drives the self-assembly into a fibrillar network. Hydrolysis deactivates the activated building blocks and controls the disassembly of the fibers (Figure 4C). In other words, the chemical environment drives the competing deactivation pathway. Performing at 35 °C, and a constant pH of 7, fibrillar structures were observed after 100 hours and lasted for another 20 hours before the full fuel's depletion and disassembly of the fibers. The ester formation and, thus, activation of the building blocks was faster than the hydrolysis step, resulting in the accumulation of activated building blocks which enabled the assembled structure. This nicely describes important conceptual requirements to create temporally controlled materials: Balancing the kinetics of the competing pathways, i.e., the rates of activation and deactivation, is decisive for successfully operating a system out-of-equilibrium and equipping it with a transient character. Effective tools for fine-tuning the kinetics are the concentration of fuel, feedback mechanisms, pH, and temperature (the latter if hydrolysis drives the deactivation step).
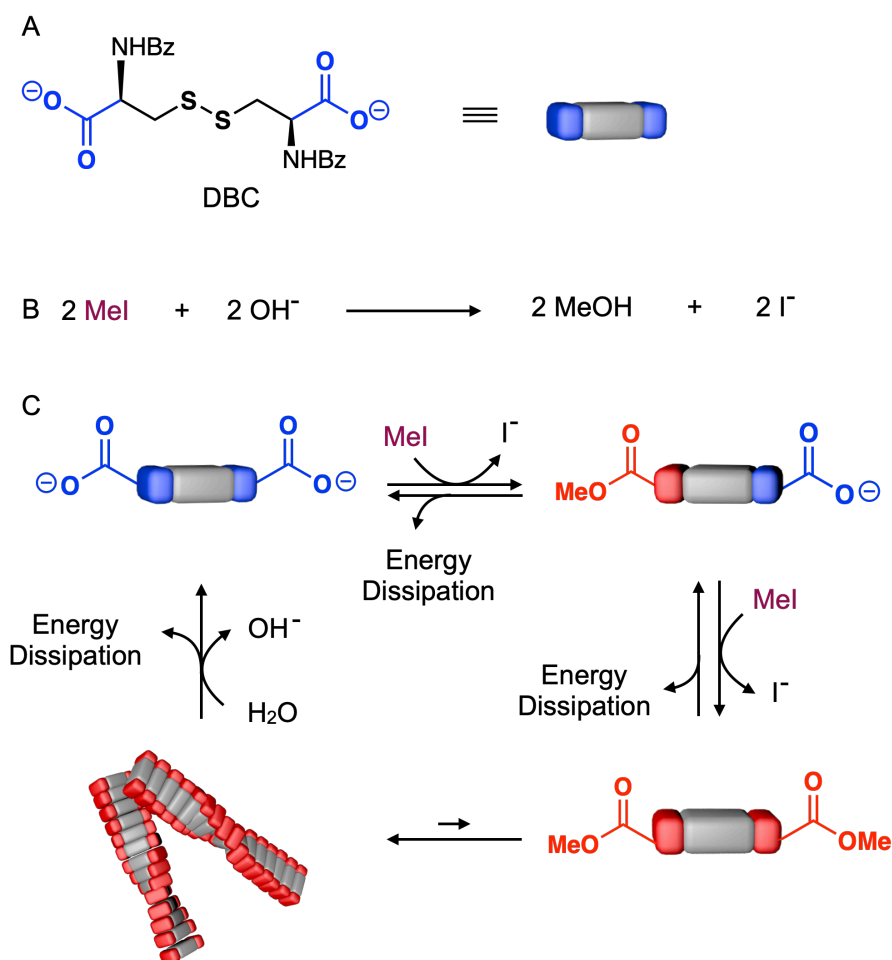
Figure 4: Methyl iodide-driven self-assembly into fibers. **A**) The structure of unreactive building block dibenzoyl-L-cysteine (DBC), (Bz = benzoyl). **B**) Net reaction of fuel MeI with hydroxide ions resulting in methyl hydroxide and iodide. **C**) Reaction cycle of chemically fueled self-assembly. DBC dicarboxylate converts to the methylated analog under the consumption of MeI. The reaction with another MeI leads to the diester DBC-OMe$_2$ structure. The loss in electrostatic interactions and the gain in hydrophobic ones, results in the self-assembly of fibers. Hydrolysis deactivates the methylated building blocks resulting in the carboxylate states. **A**), **B**) and **C**) reproduced with permission from ref. 74. Copyright 2010 John Wiley and Sons.

A similar approach for dissipative, self-assembled materials with a tunable lifetime was conducted by Boekhoven and co-workers based on a reaction cycle driven by the hydration of carbodiimides.[75] The condensing agent, 1-ethyl-3-(3-dimethylaminopropyl)carbodiimide (EDC), was applied as fuel to drive the self-assembly of fluoren-9-ylmethoxycarbonyl aspartic acid (Fmoc-D-OH) (Figure 5). Upon fuel addition, the aspartic acid is activated by the conversion to the respective anhydride. The loss in electrostatic repulsion from the two carboxylates to the anhydride moiety results in self-assembly. In the case of Fmoc-D-OH, it leads to the formation of spherulites, which results in turbidity of the solution.
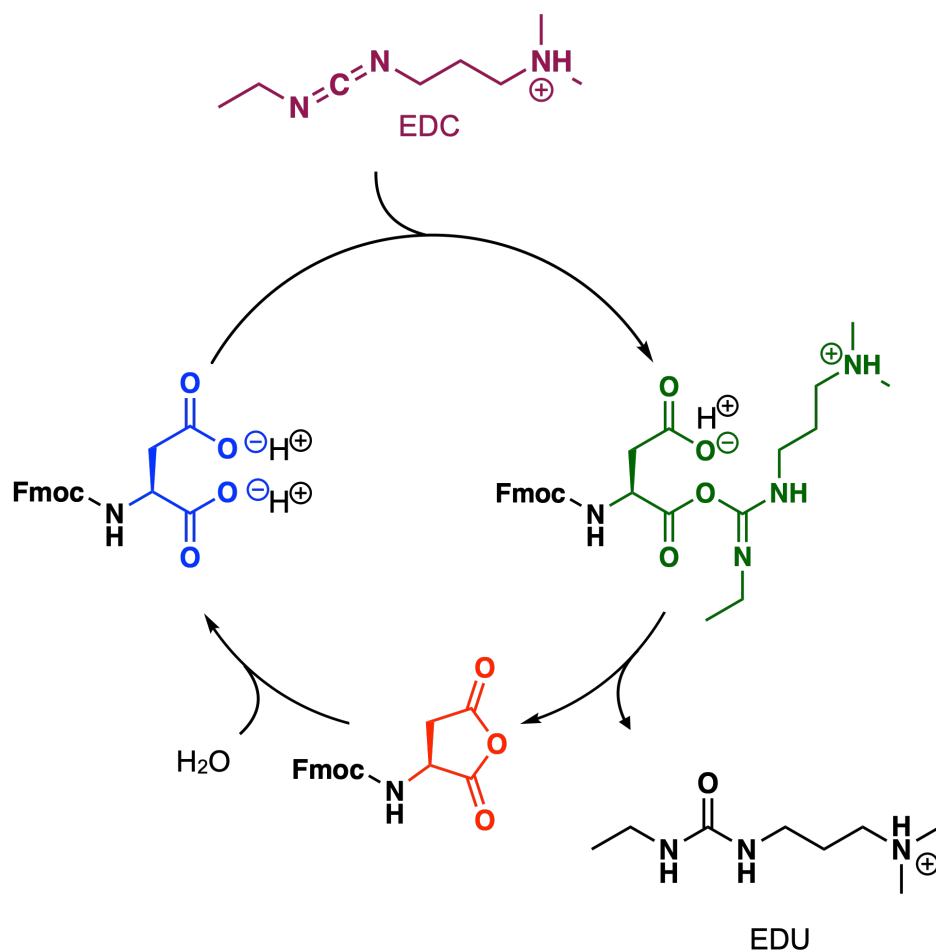
Figure 5: EDC-driven reaction cycle of Fmoc-D-OH. The deprotonated Fmoc-D-OH (blue) gets activated by the fuel EDC (purple), resulting in the respective *O*-acylurea derivative (green). Under the release of the waste EDU (black) the anhydride derivative (red) is formed. Due to the loss of electrostatic repulsion, the anhydride building blocks can self-assemble into spherulites. Water acts as deactivation agent leading to the hydrolysis of the anhydride building blocks. This eventually results in the disassembly of the spherulites.

They designed a self-erasing ink by embedding this dissipative system into a polyacrylamide polymer hydrogel which showed a change in turbidity over a specific lifetime upon fuel supply. The self-assembled components act as transient aggregates exhibiting, e.g., a change in turbidity (displaying the function of an ink) and are therefore appealing in terms of time-sensitive information storage.[45] Due to hydrolysis, the anhydride gets deactivated back to the initial aspartic acid, leading to disassembly and ink erasing. Overall, the aspartic acid catalyzes the hydrolysis reaction of the fuel EDC with high chemical potential to the waste molecule urea with a lower chemical potential and thus drives the chemical reaction network.

Indeed, carbodiimides are suitable candidates for chemical fuels that can drive chemical reaction networks and thus regulate molecular self-assembly. Like ATP, a high chemical potential can be released by the hydration of carbodiimides. In contrast, however, EDC is not

transferred during the energy supply process, i.e., it is no structural component of the self-assembled state. Carbodiimides are available as water-soluble polar ones (EDC), or hydrophobic ones (*N,N'*-diisopropylcarbodiimide (DIC), *N,N'*-dicyclohexylcarbodiimide (DCC)) and can thus be used in aqueous solution or in organic solvents. Furthermore, EDC has a relatively high stability in water with a lifetime of 37 hours (pH 7).[76] In addition, the carbodiimide-driven reaction cycle does not suffer from major side products. The *N*-acyl urea formation is well-known to be suppressible under the addition of catalytic amounts of, e.g., pyridine or 4-dimethylaminopyridine (DMAP).[77]

In a follow-up study based on EDC-driven self-assembly, Boekhoven and co-workers discovered that the material's lifetime can significantly be extended by negative feedback of the assemblies on their deactivation.[75, 78] In other words, the assembly protects itself from deactivation. In this case, the assembly affects the accessibility of activated building blocks for the deactivation reagents, decelerating the deactivation step. For instance, a system containing Fmoc-E-OH molecules is activated upon fuel addition forming the respective anhydride building blocks, which subsequently results in phase separation and self-assembly into colloids. Due to the phase separation, self-assembled molecules are protected from the deactivation agent water. Therefore, only the fraction of anhydride remaining within the water phase is deactivated, which is constant and equals the anhydride's solubility c_{sol}. Herein, hydrolysis of the anhydride occurs according to a 0th-order decay, based on $r = k_{hyd} \cdot c_{sol}$, where r equals the hydrolysis rate and k_{hyd} the hydrolysis rate constant. The assembled anhydride self-protects itself from hydrolysis, i.e., the survival time of the anhydride is elongated and, thus, the material's lifetime. They successfully applied this concept of a linearly decaying emulsion to develop a drug-delivery platform with a controlled release of pharmaceutical drugs.[79] Herein, active oil droplets containing succinic acid derivatives with an unsaturated aliphatic tail are produced upon EDC addition. Afterward, the droplets are loaded with a hydrophobic drug, e.g., Nimesulide (which mostly partitions in the droplets due to the hydrophobicity), and embedded into a hydrogel. As fuel depletes, the oil droplets disassemble according to a linear decay caused by the discussed self-protection mechanism. Consequently, the drugs also follow this linear release. The rate of the drug release, as well as the length of the release period, can be regulated by the initial EDC concentration. This work depicts a simple yet effective example of a constant release profile of pharmaceutical drugs.

The application of the EDC-driven reaction cycle is not restricted to smaller molecules, e.g., peptides, but was also applied on a polymeric level. For instance, Konkolewicz and co-workers reported the formation of a transient fibrillar hydrogel based on cross-linkage of polymers upon EDC addition.[80] Herein, acrylamide (Am) and acrylic acid (AA) copolymers (poly(Am85-*r*-

AA15)) are cross-linked by the EDC-driven carboxylic acid to anhydride conversion. In contrast to most supramolecular materials, which are typically based on non-covalent interactions, in this case, cross-linkage and, thus the self-assembly are promoted by covalent bond formation (anhydride). In other words, adding EDC results in transient covalent bond formation and not in structural modification of the building blocks to result in non-covalent interactions. The number of cross-linkages and, thus, the stiffness and lifetime of the hydrogel can be controlled by the ratio of Am to AA. Moreover, the system can be re-fueled.

3.3   Conclusion and outlook

On our route to creating supramolecular materials with life-like features, we learned that chemical fuel-driven self-assembly is a versatile approach to introduce functionality. Multiple biological systems, including the GTP-driven microtubule formation, operate out-of-equilibrium based on the steady consumption of energy to emerge sophisticated properties, e.g., spatio-temporal regulation. The energy is provided by chemical fuels and coupled to a chemical reaction network that orchestrates the activation and deactivation of assembled building blocks. Thus, the material's lifetime is controlled by the activation and deactivation rates and the amount of fuel. Synthetic materials based on dissipative self-assembly or operating under dissipative conditions have resulted in temporally controlled materials, e.g., self-erasing inks, hydrogels, or vesicles functioning as transient nanoreactors. Though some work demonstrated the self-assembly of larger molecules under dissipative conditions, e.g., block-copolymers into vesicles, apart from the fuel-driven cross-linkage and gel formation of polymers, the dissipative self-assembly of polymers based on multiple activations within one polymer strain has not yet been reported for other types of assemblies, e.g., vesicles and micelles. In the next chapter, I, therefore, present a diblock copolymer containing multiple activation sites that changes its amphiphilicity upon fuel addition resulting in the transient formation of micelles.

4 Chemically fueled block-copolymer self-assembly into transient nanoreactors

Abstract

In this work, we designed a temporally controlled material based on a chemically fueled self-assembly approach. Herein, the fuel-dependent reaction cycle induced the temporary dynamic behavior of the material while fuel was provided. We used a diblock copolymer that changes its amphiphilicity upon fuel addition resulting in the transient formation of micelles. In contrast to other micellar studies, where mostly terminated groups are functionalized, our block copolymer contained 40 diacid groups potentially being converted by fuel. Herein, the amount of added fuel dictated the lifetime of the micelles. We used these fuel-switchable micellar assemblies as nanoreactors to partition and locally up-concentrate hydrophobic reactants and, thus, accelerate chemical reactions. We tested our EDC-driven block copolymer micelles with a Diels-Alder reaction and, to our excitement, determined a significant yield increase with a higher fuel supply.

This work has been published:

This section states the individual work of each author in the publication above. M. A. Würbser and P. S. Schwarz contributed equally. J. Boekhoven, A. Walther, M. A. Würbser, P. S. Schwarz, and J. Heckel designed the experiments. M. A. Würbser, P. S. Schwarz, and J. Heckel carried out the experiments. A. M. Bergmann carried out cryo-TEM imaging. M. A. Würbser and J. Boekhoven wrote the manuscript. All authors have given approval to the final version of the manuscript.

Chemically Fueled Block Copolymer Self-Assembly into Transient Nanoreactors**

Michaela A. Würbser,[a] Patrick S. Schwarz,[a] Jonas Heckel,[b, e, f] Alexander M. Bergmann,[a] Andreas Walther,*[c, g] and Job Boekhoven*[a, d]

In chemically fueled supramolecular materials, molecular self-assembly is coupled to a fuel-driven chemical reaction cycle. The fuel-dependence makes the material dynamic and endows it with exciting properties like adaptivity and autonomy. In contrast to the large work on the self-assembly of small molecules, we herein designed a diblock copolymer, which self-assembles into transient micelles when coupled to a fuel-driven chemical reaction cycle. Moreover, we used these transient block copolymer micelles to locally increase the concentration of hydrophobic reagents and thereby function as a transient nanoreactor.

[a] M. A. Würbser, P. S. Schwarz, A. M. Bergmann, Prof. Dr. J. Boekhoven
Department of Chemistry
Technical University Munich
Lichtenbergstraße 4, 85748 Garching (Germany)
E-mail: job.boekhoven@tum.de

[b] J. Heckel
Institute for Macromolecular Chemistry
University of Freiburg
Stefan-Meier-Str. 31, 79104 Freiburg (Germany)

[c] Prof. Dr. A. Walther
A3BMS Lab
Department of Chemistry
University of Mainz
Duesbergweg 10–14, 55128 Mainz (Germany)
E-mail: andreas.walther@uni-mainz.de

[d] Prof. Dr. J. Boekhoven
Institute for Advanced Studies
Technical University Munich
Lichtenbergstraße 2a, 85748 Garching (Germany)

[e] J. Heckel
Freiburg Materials Research Center (FMF)
University of Freiburg
Stefan-Meier-Str. 21, 79104 Freiburg (Germany)

[f] J. Heckel
Freiburg Center for Interactive Materials and Bioinspired Technologies (FIT)
University of Freiburg
Georges-Köhler-Allee 105, 79110 Freiburg (Germany)

[g] Prof. Dr. A. Walther
Cluster of Excellence livMatS @ FIT – Freiburg Center for Interactive Materials and Bioinspired Technologies
University of Freiburg
Duesbergweg 10–14, 55128 Mainz (Germany)

[**] A previous version of this manuscript has been deposited on a preprint server (DOI: 10.26434/chemrxiv.14138198).

Supporting information for this article is available on the WWW under https://doi.org/10.1002/syst.202100015

In chemically fueled self-assembly, the self-assembly of molecules is regulated by a fuel-driven chemical reaction cycle.[1] The reaction cycle comprises at least two reactions, *i.e.*, a fuel-driven activation reaction that activates building blocks for self-assembly and a deactivation reaction that reverts the building blocks to their initial state. Thus, in response to a chemical fuel, a population of transient products emerges that can assemble into a desired morphology. Successful reaction cycles include the formation of transient methyl esters driven by the hydrolysis of methylating agents,[2] the phosphorylation of peptides driven by the hydrolysis of ATP,[3] ATP-assisted phosphodiester bond formation in DNA systems,[4] and the formation of anhydrides or active esters by the hydration of carbodiimides.[5] The emerging dynamic assemblies range from oil- or coacervated-based droplets,[5f,6] colloids,[7] vesicles,[5g,8] fibers,[2a,b,5a,b,e,9] supra-molecular polymers,[10] hybridized DNA,[4,11] clusters of nano- or microparticles[2c,5c,d] and others. Due to their fuel dependence, the emerging assemblies and their material properties show a limited lifetime which can be tuned by the amount of fuel added.[12] Exciting examples of such materials include self-erasing inks,[5e,13] transient photonics,[14] temporary hydrogels,[5a,11c,15] transient emulsions,[5f,6d] and transient nanoreactors.[8a,16]

Inspired by biological systems, nanoreactors have been developed to increase the efficiency of chemical reactions by up concentrating reactants.[17] There are many biological examples of such nanoreactors, which can differ from simple systems, such as enzymes, to complex self-assembled structures, such as organelles or cells.[18] Most of these structures are maintained in chemically regulated non-equilibrium states in order to control reactions spatially and temporally.[19]

Synthetic nanoreactors have been well studied under equilibrium conditions, and examples include polymer micelles,[20] vesicles,[21] star-shaped polymers,[22] core-shell micelles,[23] and dendrimers.[24] These assemblies locally increase the concentration of substrates or catalysts. In contrast, chemically fueled examples are rather scarce. Inspired by biological systems, the *in-situ* production of nanoreactors in response to a chemical fuel offers additional control parameters over the catalyzed reaction, such as temporal and spatial control as well as control over the reaction yield. Recent work has demonstrated that the yield of a reaction can be tuned by the amount of fuel for the dissipative self-assembly of transient nanoreactors.[16,25] Moreover, similar systems have been used in the context of physical autocatalysis.[6b] In this work, we thus set out to further diversify the types of self-assembly and couple a

chemically fueled reaction cycle to the self-assembly of block copolymer micelles. The formed assemblies are used as transient nanoreactors to catalyze the Diels-Alder reaction of insoluble reagents in aqueous media.

To create transient block copolymer-based assemblies, we designed a diblock copolymer (PEG$_{114}$-b-PSMA$_{40}$, **BCP1**) that comprises a hydrophilic poly(ethylene glycol) (PEG) block and a poly(styrene-alt-maleic acid) (PSMA) block (Figure 1A, the subscripts denote the number-average degree of polymerization). The PEG block was chosen as a permanent hydrophilic block that does not change its function in response to the reaction cycle. In contrast, the PSMA block is hydrophilic by nature but can be activated by the chemical reaction cycle to become hydrophobic.

We envisioned that in the fuel-driven reaction cycle, part of the maleic acid carboxylate groups of the block copolymer **BCP1** react with the condensing agent 1-ethyl-3-(3-dimethylamino-propyl)carbodiimide (EDC), resulting in the formation of the corresponding cyclic anhydride (Figure 1B). We refer to this hydrophobization reaction as the activation reaction, as it activates the precursor for self-assembly. However, in the aqueous environment, these activated building blocks react back to yield the original precursor, which constitutes the deactivation reaction. Taken together, the building block is designed to transiently switch from hydrophilic to hydrophobic at the expense of a chemical fuel (Figure 1C).

We analyzed the evolution of the chemical reaction cycle with **BCP1** as the precursor in response to 2.5, 4.0, and 5.0 mM of EDC by high-pressure liquid chromatography (HPLC). In all experiments, **BCP1** was used at a 5.0 mM concentration when expressed in the concentration of maleic acid monomer units, and the water in which it was dissolved was buffered with 100 mM MES at pH 6.0. At this concentration, no observable shift in the pH over time was measured in response to EDC. A

change in pH would be disadvantageous as it causes a decreased activation reaction rate and an increase in the hydrolysis rate which hampers the process of micellar self-assembly (Supporting Figure S1).

We measured the rapid decay of the EDC concentration, which was fully consumed over a period of 20 minutes and could be fitted with a pseudo-second-order decay using a previously described kinetic model (see Supporting Figure S2). We measured the evolution of the anhydride concentration indirectly *via* a method we recently introduced.[26] Briefly, we added benzylamine to quench the activation and deactivation reaction almost instantaneously. After the quench, we determined the converted benzylamine as a measure of the anhydride concentration (Figure 2A). The rapid decay of the EDC coincided with a rapid increase of the anhydride concentration. From there on, the anhydride decayed slowly with first-order kinetics corresponding to a half-life of roughly 82 min. The rate constants could be combined to update a previously described kinetic model that accurately predicted the evolution of our reaction cycles for several initial concentrations of fuel (Supporting Table S2, Supporting Figure S4).[5e]

Interestingly, we observed a difference in foaminess and interfacial tension of the solution, when we fueled **BCP1** with EDC (Figure 2B). After shaking the solution with polymer but without EDC, we observed some foaminess which lasted around 3 h (Figure 2B, top). In contrast, shaking the same sample with
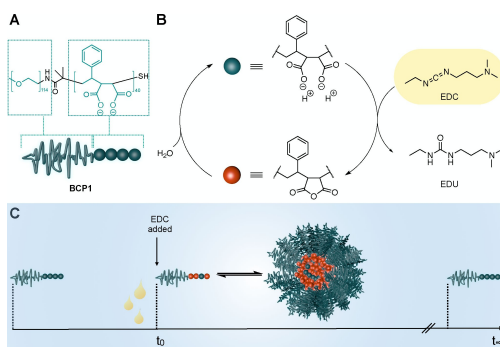
Figure 1. Chemically fueled self-assembly of **BCP1** in block copolymer micelles. A) The chemical structure of diblock copolymer **BCP1**. B) The fuel-driven reaction cycle converts dicarboxylate-based monomers into their corresponding anhydrides. The anhydrides hydrolyze back to their precursor state. C) Schematic overview of the transient anhydride formation resulting in surfactant block copolymer products which are supposed to self-assemble into transient micelles and hydrolyze back to the precursor state after depletion of the fuel.
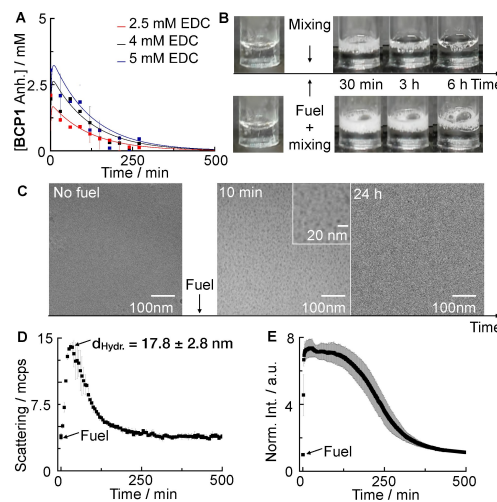
Figure 2. Transient micelle formation at the expense of a chemical fuel. A) Anhydride concentration against time when 5 mM **BCP1** was fueled with 2.5, 4, or 5 mM EDC. Markers represent HPLC data; solid lines represent theoretical data calculated using the kinetic model. B) Time-lapsed photographs of the foamy solutions of 5 mM BCP1 solution (top) and 5 mM **BCP1** solution fueled with 5 mM EDC (bottom). The solution with EDC sustained its foam significantly longer. C) Cryo-TEM micrographs of 5 mM **BCP1** before, 10 min, and 24 h after the addition of 5 mM EDC. D) Scattering rate as a function of time and normalized fluorescence intensity as a function of time (E) of 5 mM **BCP1** fueled with 5 mM EDC in the presence of 2.5 μM Nile Red.

Chemically fueled block-copolymer self-assembly into transient nanoreactors

5 mM EDC induced more foam formation, and it remained for more than 6 h (Figure 2B, bottom). The increased foam stability is likely a result of a slightly decreased interfacial surface tension between the air and water interface. We confirmed this by pendant drop interfacial tensiometry (Supporting Table S3), showing that the surface tension decreased from 56 mNm^{-1} to 52 mNm^{-1} upon fuel addition and restored after several hours. We explain the rather narrow decrease by the already present surface activity of the **BCP1** solution prior to activation (Supporting Table S3). Moreover, the transition into micelles of common surfactants only marginally affects the interfacial surface tension.[27]

Using cryogenic transmission electron microscopy (cryo-TEM), we studied the fuel-induced changes in the solution further. Before the addition of 5 mM EDC, we found no evidence of self-assembly of **BCP1** (Figure 2C). Ten minutes after, the evolution of monodisperse, self-assembled micelles with a diameter of roughly 10 nm can be observed that disappeared after 24 hours. The emergence and decay of small self-assembling species was further confirmed by dynamic light scattering (DLS). We found a rapid increase in the scattering intensity after the addition of the fuel (Figure 2D). A concentration range of 0.25 to 0.5 mM fuel was investigated as minimum concentration resulting in an increased scattering, thus inducing self-assembly (Supporting Figure S6). However, by comparing the maximum anhydride concentration and scattering rate, we noticed a delay. We assumed that the activated block copolymer products require some time to rearrange and overcome the already existing non-covalent interactions. The hydrodynamic diameter at the maximum scattering intensity was roughly 18 nm, further confirming the formation of micelles upon the addition of fuel (Supporting Figure S7). Over the course of the reaction cycle, we found that the scattering decreased. The decay of the scattering coincided with the decay of the anhydride concentration further corroborating the correlation between the emergence and decay of the assembly at the expense of the chemical fuel.

Furthermore, we tested the formation of hydrophobic domains by a Nile Red fluorescence assay. This assay is a convenient method to test whether hydrophobic molecules can be incorporated into assemblies (Figure 2E).[28] Such inclusion of hydrophobic derivatives would be a requirement for the use of our transient assemblies as nanoreactors. When we fueled a solution of 5 mM **BCP1** and 2.5 μM Nile Red with 5 mM EDC, we found that the fluorescence intensity immediately increased, pointing at its uptake by the assemblies. Moreover, the fluorescence intensity decreased over the course of the reaction suggesting that Nile Red is released upon disassembly. Taken together, we successfully designed a diblock copolymer that transiently self-assembles into micelles in response to EDC as chemical fuel and is able to incorporate and release hydrophobic molecules.

Next, we tested the transient micelles' ability to partition and locally up concentrate reactants, thus serving as nanoreactors and accelerating reactions. The Diels-Alder reaction is a prominent example for being catalyzed by the micelles, as this has been demonstrated before with conventional micelles and

the reaction conditions are compatible with our EDC-driven cycle.[29] A downside of using micelles as a nanoreactor can be product inhibition, *i.e.*, the product remains in the micelles, which reduces its activity. The transient character of our micelles could prevent such product inhibition.

We combined our EDC-driven block copolymer micelles with the Diels-Alder reaction of *N*-benzyl maleimide (**1**) and sorbic alcohol or ethyl sorbate (**2a** or **2b**, respectively) which are known as suitable dienophile and dienes for the Diels-Alder reaction (Figure 3A).[29a,e,30] We chose these reagents because of their difference in hydrophilicity.

We first performed the reaction with 0.2 mM of **1** and 5 mM of **2a** in buffered aqueous solution and observed a fast reaction and full turnover to product **3a** (see Supporting Figure S8, S9, and S12). An excess of the diene guaranteed a pseudo-first-order reaction. Upon addition of 5 mM **BCP1**, the reaction remained unaffected (Figure 3B). In the presence of 30 mM EDC, no evidence for micellar catalysis was found (Figure 3B). In fact, the reaction decelerated slightly. These findings can be explained by the relatively high solubility of **2a** (roughly 150 mM, see Supporting Table S6). We conclude that the reaction preferably occurred in the aqueous media. In fact, partitioning of some *N*-benzyl maleimide (**1**) in the micelles may explain the slight deceleration as it separates the reagents from one another.

Next, we performed the reaction in a buffered aqueous solution using 0.2 mM of **1** and an excess of the more hydrophobic diene **2b** (5 mM) to form the Diels-Alder product **3b**. The reaction reached a poor yield of roughly 8% after 800 minutes, likely due to the low solubility of **2b** (see Supporting Figure S10, S11 and S13). In the presence of 5 mM of **BCP1**, the reaction yield remained unchanged (Figure 3C). In contrast, the yield of **3b** increased substantially upon fuel addition. We extended our kinetic model such that it also
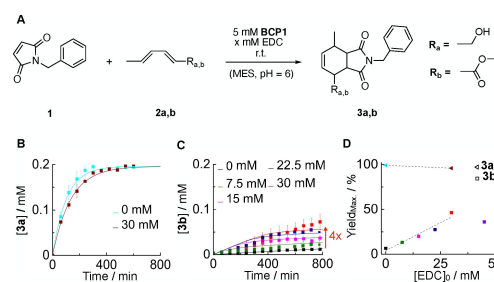

Figure 3. BCP1 micelles as dissipative nanoreactors for Diels-Alder reaction. A) Reaction scheme of the Diels-Alder reaction of the dienophile **1** with the dienes **2a** and **2b** to form the respective Diels-Alder products **3a** and **3b**. B) Concentration profile of **3a** for 0.2 mM **1** and 5 mM **2a** in 5 mM **BCP1** solution fueled with 0 and 30 mM EDC. The presence of **BCP1** micelles has no effect on the reaction rate and yield of **3a**. C) Concentration profile of **3b** for 0.2 mM **1** and 5 mM **2b** in 5 mM **BCP1** solution fueled with different amounts of EDC. The yield increases with increasing fuel concentration. D) Maximum yield of **3a** and **3b** in dependence on the initial fuel concentration. Markers represent HPLC data; solid lines represent theoretical data calculated using the kinetic model.

Chemically fueled block-copolymer self-assembly into transient nanoreactors

ChemSystemsChem | Communications
doi.org/10.1002/syst.202100015

Chemistry Europe
European Chemical
Societies Publishing

predicted the evolution of the Diels-Alder reactions. We used a pseudo first-order rate equation to calculate the rate every second in the reaction cycle. This reaction rate was divided into two parts, *i.e.*, the reaction that occurred in solution (k_6*[**1**]) and the reaction that occurred in the nanoreactor which we made dependent on the anhydride concentration of **BCP1** (k_{cat}*[**1**]*-[Anh]) (see Supporting Notes).

We found a positive k_{cat} when we performed the reaction of **1** and **2b** in the presence of **BCP1** and fuel (Supporting Table S9). Our kinetic model showed that the catalytic activity of **BCP1** increases roughly 7.5-fold when fully converted to the anhydride (Supporting Figure S15). Larger fuel concentrations resulted in higher reaction yields which we attributed to a longer sustained acceleration rate of **BCP1** (Supporting Figure S15). For example, when using 30 mM EDC, the yield of **3b** was improved by a 4-fold compared without EDC. When we used fuel concentrations higher than 30 mM, we observed that the yield of **3b** did not increase further, *e.g.*, the product evolution of **3b** for 45 mM EDC reached a yield of roughly 40% (see Supporting Figure S14). We explain this limitation by the hydrolysis of **1**, **2b** and **3b** and the accumulation of the waste. Indeed, the behavior of the Diels-Alder reaction in the presence of different amounts of sodium dodecyl sulfate (SDS), a common anionic surfactant, also increased the reaction yield to 38–53% after 1200 minutes depending on the amount added (Supporting Figure S13).

We investigated how the yield is dependent on the initial fuel concentration for both reactions. For the Diels-Alder reaction of **3b**, we found that the yield increases linearly with an initial concentration of the fuel (Figure 3D). However, the increased yield leveled off at fuel concentrations higher than 30 mM. Unlike **2b**, for the Diels-Alder reaction of **2a**, the yield and reaction rate was independent of the initial fuel concentration indicating that the reaction preferably occurs in the aqueous environment.

It is worth mentioning that our kinetic model could also predict the evolution of the Diels-Alder with the well soluble **2a** diene, provided that we used a negative k_{cat} (Supporting Table S7) which resulted in a slower reaction rate and further corroborates that the presence of the micelles separates the reagents causing slight deceleration of the reaction.[31] These combined results clearly demonstrate presence of the micelles can accelerate a Diels-Alder reaction provided that both reactants are sufficiently hydrophobic. We can thus conclude that our micelles are not only as efficient in catalyzing Diels-Alder reactions just as regular surfactants but particularly possess the advantage of tuneability of yield or lifetime by their fuel-driven reaction cycle. Moreover, the disassembly of the micelles after depletion of the fuel prevents potential product inhibition.

In this work, we used a carbodiimide-fueled chemical reaction cycle to regulate the transient assembly of a diblock copolymer with fuel-switchable amphiphilicity. In response to chemical fuel, the block copolymers were transiently activated for assembly into micelles which showed a notably reduced interfacial tension between air and water. We demonstrate that the lifetime of the solution containing these micelles could be

regulated by the amount of fuel added. We used the assemblies as a nanoreactor to transiently increase the concentration of reagents for a Diels-Alder reaction and found that yields vastly improved with increasing amounts of fuel. In future work, we will further couple the nanoreactor catalysis to our fuel-driven reaction cycle, *e.g.*, to alter the molecular structure of the precursor, which might result in fascinating properties, such as autocatalysis.

Conflict of Interest

The authors declare no conflict of interest.

[1] a) S. De, R. Klajn, *Adv. Mater.* **2018**, *30*, 1706750; b) R. Merindol, A. Walther, *Chem. Soc. Rev.* **2017**, *46*, 5588; c) B. Rieß, R. K. Grötsch, J. Boekhoven, *Chem* **2020**, *6*, 552; d) N. Singh, G. J. M. Formon, S. De Piccoli, T. M. Hermans, *Adv. Mater.* **2020**, *32*, 1906834; e) G. Wang, S. Liu, *ChemSystemsChem* **2020**, *2*, e1900046.

[2] a) J. Boekhoven, A. M. Brizard, K. N. K. Kowlgi, G. J. M. Koper, R. Eelkema, J. H. van Esch, *Angew. Chem. Int. Ed.* **2010**, *49*, 4825; b) J. Boekhoven, W. E. Hendriksen, G. J. M. Koper, R. Eelkema, J. H. van Esch, *Science* **2015**, *349*, 1075; c) B. G. P. van Ravensteijn, W. E. Hendriksen, R. Eelkema, J. H. van Esch, W. K. Kegel, *J. Am. Chem. Soc.* **2017**, *139*, 9763.

[3] A. Sorrenti, J. Leira-Iglesias, A. Sato, T. M. Hermans, *Nat. Commun.* **2017**, *8*, 15899.

[4] L. Heinen, A. Walther, *Sci. Adv.* **2019**, *5*, eaaw0590.

[5] a) S. P. Afrose, S. Bal, A. Chatterjee, K. Das, D. Das, *Angew. Chem. Int. Ed.* **2019**, *58*, 15783; b) K. Dai, J. R. Fores, C. Wanzke, B. Winkeljann, A. M. Bergmann, O. Lieleg, J. Boekhoven, *J. Am. Chem. Soc.* **2020**, *142*, 14142; c) R. K. Grötsch, A. Angı, Y. G. Mideksa, C. Wanzke, M. Tena-Solsona, M. J. Feige, B. Rieger, J. Boekhoven, *Angew. Chem. Int. Ed.* **2018**, *57*, 14608; d) R. K. Grötsch, C. Wanzke, M. Speckbacher, A. Angı, B. Rieger, J. Boekhoven, *J. Am. Chem. Soc.* **2019**, *141*, 9872; e) M. Tena-Solsona, B. Rieß, R. K. Grötsch, F. C. Löhrer, C. Wanzke, B. Käsdorf, A. R. Bausch, P. Müller-Buschbaum, O. Lieleg, J. Boekhoven, *Nat. Commun.* **2017**, *8*, 15895; f) M. Tena-Solsona, C. Wanzke, B. Riess, A. R. Bausch, J. Boekhoven, *Nat. Commun.* **2018**, *9*, 2044; g) C. Wanzke, A. Jussupow, F. Kohler, H. Dietz, V. R. Kaila, J. Boekhoven, *ChemSystemsChem* **2020**, *2*, e1900044.

[6] a) C. Donau, F. Späth, M. Sosson, B. A. Kriebisch, F. Schnitter, M. Tena-Solsona, H.-S. Kang, E. Salibi, M. Sattler, H. Mutschler, *Nat. Commun.* **2020**, *11*, 1; b) S. M. Morrow, I. Colomer, S. P. Fletcher, *Nat. Commun.* **2019**, *10*, 1; c) I. Myrgorodska, I. Colomer, S. P. Fletcher, *ChemSystemsChem* **2020**, *2*, e1900059; d) C. Wanzke, M. Tena-Solsona, B. Rieß, L. Tebcharani, J. Boekhoven, *Mater. Horiz.* **2020**, *7*, 1397.

[7] B. Rieß, C. Wanzke, M. Tena-Solsona, R. K. Grötsch, C. Maity, J. Boekhoven, *Soft Matter* **2018**, *14*, 4852.

[8] a) S. Maiti, I. Fortunati, C. Ferrante, P. Scrimin, L. J. Prins, *Nat. Chem.* **2016**, *8*, 725; b) E. A. Post, S. P. Fletcher, *Chem. Sci.* **2020**, *11*, 9434.

[9] a) S. Debnath, S. Roy, R. V. Ulijn, *J. Am. Chem. Soc.* **2013**, *135*, 16789; b) B. A. Kriebisch, A. Jussupow, A. M. Bergmann, F. Kohler, H. Dietz, V. R. Kaila, J. Boekhoven, *J. Am. Chem. Soc.* **2020**, *142*, 20837; c) S. Panja, B. Dietrich, D. J. Adams, *ChemSystemsChem* **2020**, *2*, e1900038; d) E. Te Brinke, J. Groen, A. Herrmann, H. A. Heus, G. Rivas, E. Spruijt, W. T. Huck, *Nat. Nanotechnol.* **2018**, *13*, 849.

[10] a) S. Dhiman, R. Ghosh, S. J. George, *ChemSystemsChem* **2020**, *2*, e1900042; b) J. Leira-Iglesias, A. Tassoni, T. Adachi, M. Stich, T. M. Hermans, *Nat. Nanotechnol.* **2018**, *13*, 1021.

[11] a) E. Del Grosso, L. J. Prins, F. Ricci, *Angew. Chem. Int. Ed.* **2020**, *59*, 13238; b) E. Del Grosso, G. Ragazzon, L. J. Prins, F. Ricci, *Angew. Chem.* **2019**, *131*, 5638; c) L. Heinen, T. Heuser, A. Steinschulte, A. Walther, *Nano Lett.* **2017**, *17*, 4989.

[12] B. Rieß, J. Boekhoven, *ChemNanoMat* **2018**, *4*, 710.

[13] R. Klajn, P. J. Wesson, K. J. Bishop, B. A. Grzybowski, *Angew. Chem. Int. Ed.* **2009**, *48*, 7035.

[14] T. Heuser, R. Merindol, S. Loescher, A. Klaus, A. Walther, *Adv. Mater.* **2017**, *29*, 1606842.

[15] a) S. Panja, B. Dietrich, D. J. Adams, *ChemSystemsChem* **2020**, *2*, e1900038; b) S. Ahmed, A. Chatterjee, K. Das, D. Das, *Chem. Sci.* **2019**, *10*, 7574; c) S. Panja, C. Patterson, D. J. Adams, *Macromol. Rapid Commun.* **2019**, *40*, 1900251; d) T. Heuser, E. Weyandt, A. Walther, *Angew. Chem. Int. Ed.* **2015**, *54*, 13258; e) N. Singh, B. Lainer, G. J. M. Formon, S. De Piccoli, T. M. Hermans, *J. Am. Chem. Soc.* **2020**, *142*, 4083.

[16] a) S. Chandrabhas, S. Maiti, I. Fortunati, C. Ferrante, L. Gabrielli, L. J. Prins, *Angew. Chem.* **2020**, *132*, 22407; b) H. Che, S. Cao, J. C. M. van Hest, *J. Am. Chem. Soc.* **2018**, *140*, 5356.

[17] a) D. M. Vriezema, M. Comellas Aragonès, J. A. A. W. Elemans, J. J. L. M. Cornelissen, A. E. Rowan, R. J. M. Nolte, *Chem. Rev.* **2005**, *105*, 1445; b) R. Chandrawati, M. P. van Koeverden, H. Lomas, F. Caruso, *J. Phys. Chem. Lett.* **2011**, *2*, 2639.

[18] K. Renggli, P. Baumann, K. Langowska, O. Onaca, N. Bruns, W. Meier, *Adv. Funct. Mater.* **2011**, *21*, 1241.

[19] a) R. Pascal, A. Pross, *Origins Life Evol. Biospheres* **2016**, *46*, 507; b) C. H. Lineweaver, C. A. Egan, *Physics of Life Reviews* **2008**, *5*, 225.

[20] M. J. Monteiro, *Macromolecules* **2010**, *43*, 1159.

[21] P. Tanner, P. Baumann, R. Enea, O. Onaca, C. Palivan, W. Meier, *Acc. Chem. Res.* **2011**, *44*, 1039.

[22] H. Gao, *Macromol. Rapid Commun.* **2012**, *33*, 722.

[23] R. J. R. W. Peters, I. Louzao, J. C. M. van Hest, *Chem. Sci.* **2012**, *3*, 335.

[24] B. Rasmussen, J. B. Christensen, *Org. Biomol. Chem.* **2012**, *10*, 4821.

[25] S. Maiti, I. Fortunati, C. Ferrante, P. Scrimin, L. J. Prins, *Nat. Chem.* **2016**, *8*, 725.

[26] F. Schnitter, J. Boekhoven, *ChemSystemsChem* **2021**, *3*, e2000037.

[27] H. Ma, M. Luo, L. L. Dai, *Phys. Chem. Chem. Phys.* **2008**, *10*, 2207.

[28] J. Heckel, S. Loescher, R. T. Mathers, A. Walther, *Angew. Chem.* **2020**.

[29] a) T. Rispens, J. B. F. N. Engberts, *J. Org. Chem.* **2003**, *68*, 8520; b) T. Rispens, J. B. F. N. Engberts, *J. Org. Chem.* **2002**, *67*, 7369; c) S. Otto, J. B. Engberts, J. C. Kwak, *J. Am. Chem. Soc.* **1998**, *120*, 9517; d) P. A. Grieco, P. Garner, Z.-m. He, *Tetrahedron Lett.* **1983**, *24*, 1897; e) K. Bica, P. Gärtner, P. J. Gritsch, A. K. Ressmann, C. Schröder, R. Zirbs, *Chem. Commun.* **2012**, *48*, 5013.

[30] G. D. Khandelwal, B. L. Wedzicha, *Food Chem.* **1997**, *60*, 237.

[31] S. Otto, J. Engberts, *Pure Appl. Chem.* **2000**, *72*, 1365.

- 27 -

- 28 -

ChemSystemsChem

Supporting Information

Chemically Fueled Block Copolymer Self-Assembly into Transient Nanoreactors**

Michaela A. Würbser, Patrick S. Schwarz, Jonas Heckel, Alexander M. Bergmann, Andreas Walther,* and Job Boekhoven*
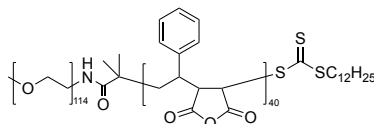
Experimental Section

Materials

We purchased α-amino,ω-methoxy-poly(ethylene glycol) (mPEG$_{114}$-NH, M_n = 5000 gmol^{-1}), 2-(dodecylthiocarbonothioylthio)-2-methylpropionic acid (DDMAT, 98%), maleic anhydride (>99%), 2,2 azobis(2-methylpropionitril) (AIBN, 98%), 2-(N-morpholino)ethane sulfonic acid (MES buffer), styrene (>99%), 1-ethyl-3-(3-dimethylaminopropyl)carbodiimide hydrochloride (EDC, >98%), Nile Red, (E/E)-2,4-hexadiene acid ethyl ester (**2b**, >98%), (E/E)-2,4-Hexadien-1-ol (**2a**, >97%), N-benzyl maleimide (**1**, 99%), benzylamine (BA, 99%), dichloromethane (DCM, >99%) and deuterated chloroform-d$_1$ (99.8 atom % D) from *Sigma-Aldrich*. Oxalyl chloride (98%) was purchased from *ABCR*. We purchased triethylamine (NEt$_3$, >99.5%) from *Carl Roth*. High performance liquid chromatography (HPLC) grade acetonitrile (ACN) was purchased from *VWR*. We removed the contained inhibitors of styrene by passing over basic alumina. All other chemicals were used without any further purification unless otherwise indicated.

Synthesis

Preparation of pegylated RAFT-agent (PEG$_{114}$-DDMAT).
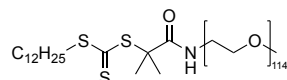
To a solution of DDMAT (2-(dodecylthiocarbonothioylthio)-2-methylpropionic acid, 1.53 g, 4.20 mmol) in DCM (20 mL), oxalyl chloride (1.07 g, 8.43 mmol, 2.0 eq.) was added dropwise at 0 °C, followed by the addition of catalytic amount of DMF (20.0 µL, 18.9 mg, 0.26 mmol, 0.06 eq.). The reaction mixture was stirred at 0 °C for 2 h, after which the solvent and residual oxalyl chloride were removed under reduced pressure. The residue was dissolved in DCM (20 mL), and cooled to 0°C. To this, a solution of mPEG$_{114}$-NH (α-amino,ω-methoxy poly(ethylene glycol), M_n = 5000 gmol^{-1}, 2.10 g, 0.42 mmol, 0.1 eq.) and NEt$_3$ (0.58 mL, 425 mg, 4.20 mmol, 1.0 eq) in DCM (20 mL) was added dropwise and the reaction mixture was stirred at 0 °C for 30 min, followed by stirring at r.t. for 16 h. The reaction mixture was concentrated under reduced pressure to a total volume of approximately 20 mL and the polymer was purified by precipitation from cold ^{i}PrOH (-30 °C, 3 x 200 mL) and pentane (200 mL) with redissolution in DCM (20 mL). After drying at HV, PEG$_{114}$-DDMAT was obtained as a yellow solid. Dispersity was determined via SEC in DMAc (see Supporting Figure S18). Yield: 0.95 g (43% with respect to mPEG, $Đ_{SEC}$ = 1.10, degree of functionalization d_f ≈ 100 %, see Supporting Figure S16).

Preparation of poly(ethylene glycol)-block-poly(styrene-alt-maleic anhydride) block copolymer (BCP1)[1]

A 50 mL round-bottom flask equipped with a stir bar was charged with mPEG$_{114}$-DDMAT (0.95 g, 177.0 µmol), maleic anhydride (3.48 g, 3.55 mmol, 200 eq.), styrene (3.70 g, 3.55 mmol, 200 eq.), AIBN (5.8 mg, 35 µmol, 0.2 eq., from 2 mg/mL stock solution in dioxane), dioxane (26 mL) and trioxane (80 mg as an internal standard for ^{1}H-NMR). The flask was sealed with a rubber septum and the reaction mixture was purged with N$_2$ for 30 min. Polymerization was initiated by immerging the flask in an oil-bath thermostated at 70 °C. The polymerization was monitored via ^{1}H-NMR spectroscopy (CD$_3$CN) of aliquots taken at regular intervals to determine monomer conversion from the decrease of the maleic anhydride (7.16 ppm) and styrene vinyl (5.29, 5.84, 6.80 ppm) signals relative to the trioxane signal (5.15 ppm), which showed equal conversion for the two monomers. The reaction mixture was removed after 180 min and polymerization was stopped by exposure to air and immediate precipitation of the polymer from a tenfold excess of diethyl ether. The polymer was purified by dissolution in dioxane (10 wt% polymer) and precipitation from a tenfold excess of diethyl ether/dioxane (9/1, v/v). After drying at HV, the polymer **BCP1** was obtained as a yellow solid. A degree of polymerization of 40 for the PSMA block was determined via ^{1}H-NMR spectroscopy (CD$_3$CN) from the ratio of the aromatic styrene signal to the PEG CH_2 signal, assuming a degree of polymerization of 114 for the PEG block (see Supporting Figure S17). The same values were also used to calculate number-average molecular weights. Dispersities Đ were determined from SEC in DMAc (see Supporting Figure S18).

BCP1: Đ$_{SEC}$ = 1.18, $M_{n,NMR}$ = 13450 gmol^{-1}.
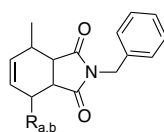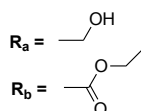
Preparation of Diels-Alder product 3.

3a,b

R$_a$ =

R$_b$ =

To a solution of *N*-benzyl maleimide (**1**, 0.598 g, 3.19 mmol, 1.0 eq.) in DCM (5 mL), (*E/E*)-2,4-hexadiene acid ethyl ester (**2b**) or (*E/E*)-2,4-Hexadien-1-ol (**2a**), (15.97 mmol, 5.0 eq.) was added and stirred at room temperature for 18 h. After evaporation of the solvent, the raw product was purified using reversed-phase chromatography (linear gradient of acetonitrile, 40 to 98%, and water with 0.1% TFA). The combined fractions were lyophilized *in vacuo*. The purified product was used for its calibration on the HPLC as reference for the Diels-Alder kinetics (see Supporting Figure S6-9 and Supporting Figure S19-24).

2-Benzyl-4-(hydroxymethyl)-7-methyl-3a,4,7,7a-tetrahydro-1*H*-isoindole-1,3(2*H*)-dione **3a**: Transparent viscous oil   (yield = 486.0 mg, 53%); ^{1}H NMR (300 MHz, CDCl$_3$): δ (ppm) = 7.32-7.24 (m, 5H, Ar-H), 5.76 (dt, $^3J_{H-H}$ = 9.2, 3.3 Hz, 1H, CH=C), 5.76 (dt, $^3J_{H-H}$ = 9.2, 3.2 Hz, 1H; CH=C), 4.60 (s, 2H; CH$_2$), 4.02 (dd, $^3J_{H-H}$ = 7.0, $^2J_{H-H}$ = 3.3 Hz, 1H; CH$_2$), 3.92 (dd, $^3J_{H-H}$ = 7.0, ^2J = 3.3 Hz, 1H; CH$_2$), 3.86 (s, 1H; OH); 2.59 (qdd, $^3J_{H-H}$ = 8.6, 3.3, 2.0 Hz, 1H; CH), 3.36 (dd, $^3J_{H-H}$ = 8.6, 7.1 Hz, 1H; CH), 3.08 (, $^3J_{H-H}$ = 8.6, 6.5 Hz, 1H; CH) 2.45 (qdd, $^3J_{H-H}$ = 8.6, 3.3, 2.0 Hz, 1H; CH), 1.48 (d, $^3J_{H-H}$ = 7.4 Hz, 1H; CH$_3$); *Endo/exo*-ratio: 86/14. ^{13}C NMR (101 MHz, CDCl3): δ (ppm) = 178.9, 177.2, 135.6, 135.4, 128.6, 128.4, 128.3, 127.8, 62.8, 45.1,43.0, 42. 3, 38.1, 31.3, 16.7; HRMS (ESI): *m/z* calcd for C$_{17}$H$_{19}$NO$_3$: 285.14; found: 286.12 [M+H]$^+$; HPLC: R$_t$ = 2.40 min.

Ethyl 2-benzyl-7-methyl-1,3-dioxo-2,3,3a,4,7,7a-hexahydro-1H-isoindole-4-carboxylate **3b**: Transparent solid (yield = 470.2 mg, 41%); ^{1}H NMR (300 MHz, CDCl$_3$) :δ (ppm) = 7.27 – 7.22 (m, 5 H; Ar-H), 6.34 (dt, $^3J_{\text{H-H}}$ = 9.3, 3.3 Hz, 1H; CH=C), 5.68 (dt, $^3J_{\text{H-H}}$ = 9.3, 3.4 Hz, 1H; CH=C), 4.54 (dd, $^3J_{\text{H-H}}$ = 7.1,1.0 Hz, 2H; CH$_2$), 4.31 (qd, $^3J_{\text{H-H}}$ = 7.1,1.0 Hz 3.4 Hz, 2H; CH), 3.71 (dd, $^3J_{\text{H-H}}$ = 8.8, 5.7 Hz, 1H; CH), 3.09 (dd, $^3J_{\text{H-H}}$ = 8.8, 5.7 Hz, 2H; CH), 2.40 (qdd, $^3J_{\text{H-H}}$ = 11.0, 5.5, 2.7 Hz, 1H; CH), 1.39 (d, $^3J_{\text{H-H}}$ = 7.4 Hz, 3H; CH$_3$), 1.33 (t, $^3J_{\text{H-H}}$ = 7.1 Hz, 3H; CH$_3$); ^{13}C NMR (101 MHz, CDCl$_3$): δ (ppm) = 176.7, 176.6, 170.8, 135.8, 134.6, 128.6, 128.5, 127.9, 126.5, 61.4, 44.0, 43.9, 42.4, 40.6, 31.6, 16.7, 14.3; HRMS (ESI): m/z calcd for C$_{19}$H$_{21}$NO$_4$: 327.15; found: 328.09 [M+H]$^+$; HPLC: R$_t$ = 4.78 min.

Experimental Methods.

Sample preparation. We suspended 6.72 mg of **BCP1** anhydride (1 mM monomeric maleic anhydride units) in 20 mL of a 10 mM MES solution at pH 9. The reaction mixture was shaken for 3 days for the complete hydrolysis of the maleic anhydride moieties. The reaction mixture was freeze-dried. Next, we added 20 mL of a 10 mM MES solution at pH 6.0 to adjust the overall pH to pH 6.0 and distributed the solution in 5 mL aliquots. The aliquots were again freeze-dried and stored at -20 °C until further usage. We added 1 mL MQ water to each aliquot before an experiment. The addition of 1 mL MQ water results in 5 mM **BCP1** concentration (with respect to the monomeric maleic acid units) in 100 mM MES at pH 6.0.

Determination of solubilities of dienes. A saturated solution of diene **2** was prepared (diene/100 mM MES buffer, 1/4). After mixing and ultrasonication for 10 minutes, the solution was equilibrated. This was followed by centrifugation (13500 rounds per minute, 5 min). The upper phase was removed, and the buffer phase analyzed by HPLC. In case of diene **2b**, phase separation in aqueous buffer solution was noticed even after 3 days. Therefore, the solubility was determined in respect to the equilibrated value of **2b** after 3 days under consideration of its hydrolyzed fraction.

Quantification of the anhydride concentration. We prepared 200 µL of 5 mM **BCP1** stock solution into a screw cap HPLC vial with micro insert and added the appropriate amount of fuel by the addition of a highly concentrated EDC stock in MQ water. Next, 20 µL samples were taken at the respective timepoints and quenched with 20 µL of a 40 mM BA stock solution in MQ water following a previously reported protocol.[2] The BA reacts irreversibly with the anhydride groups and inhibits the reaction with remaining EDC. We quantified the BA concentration at different time points in the reaction cycle and calculated the anhydride concentration from the consumption of BA using the relation *c(Anhydride) = c$_0$(BA) - c(BA)*.

Diels-Alder reaction. We prepared 200 µL of a 5 mM stock solution of **BCP1** in a screw cap HPLC with micro inset. Next, the reaction cycle was started by the addition of a highly concentrated EDC stock solution as described above. The experiment was equilibrated for 10 min to form **BCP1** micelles. Afterwards, the Diels-Alder reaction was started by adding 0.4 µL of a 100 mM stock solution of **1** and 2 µL of a 500 mM stock solution of **2**. We investigated the reaction kinetics via HPLC. Control experiments in 100 mM MES and 10 mM SDS were prepared as described above but without **BCP1**.

High Performance Liquid Chromatography (HPLC). We monitored the kinetics of the reaction cycle and Diels-Alder reaction by analytical HPLC (*ThermoFisher* Vanquish Duo UHPLC) with a Hypersil Gold 100 x 2.1 mm C18 column (3 µm pore size). We prepared 200 µL of the reaction mixture into a screw cap HPLC vial with micro inset following the sample preparation protocol described above. All samples were directly injected without any further dilution from the HPLC vial. We injected 1 µL for the detection of BA, 0.1 µL for the detection of EDC and 3 µL for the detection of **1**, **2a** and **2b** and the respective Diels-Alder products **3a** and **3b**. We used a UV/Vis detector at 254 nm for the quantification of BA, **2a** and **3a** and 220 nm for the quantification of all other reagents. Calibration curves for the EDC (in MQ water), benzylamine (in MQ water), **1** (in MES buffer), **2a** (in ACN), **2b** (in ACN) and Diels-Alder products **3a** and **3b** (in ACN) were performed with the corresponding methods in triplicate. Retention times and calibration values are given in Supporting Table S1, S4 and S5. We used the following methods for the separation of the compounds:

HPLC method 1: H$_2$O: ACN from 95:5 to 75:25 in 3 min, from 75:25 to 2:98 in 0.5 min, 2:98 from 3.5 min to 6 min, from 2:98 to 95:5 in 0.5 min, 95:5 from 6.5 min to 10 min.

HPLC method 2: H$_2$O: ACN from 95:5 to 2:98 in 5 min, 2:98 from 5 min to 6.5 min, from 2:98 to 95:5 in 0.5 min, 95:5 from 7 min to 10 min.

HPLC method 3: H$_2$O: ACN from 60:40 to 2:98 in 5 min, 2:98 from 5 min to 6.5 min, from 2:98 to 60:40 in 0.5 min, 60:40 from 7 min to 10 min.

Reversed-phase High Performance Liquid Chromatography (HPLC). The Diels-Alder raw products **3a** and **3b** were purified on reversed-phase HPLC (*Thermofisher*, Hypersil Gold 250 x 20mm, 5 µm pore size, C18 column) with a linear gradient of acetonitrile (ACN, 40 to 98%) and water with 0.1% trifluoroacetic acid.

Size-Exclusion Chromatography (SEC). SEC was performed using an *Agilent* 1200 system equipped with a 1260 series isocratic pump and a refractive index detector. The stationary phase consisted of a pre-column and three GRAM gel columns (8 x 300 mm, *Polymer Standard Services*) with pore sizes of 30, 1000, and 1000 Å, respectively. Chromatography was performed at 50°C at a flowrate of 1 mLmin^{-1} DMAc + 0.5 wt% LiBr. Narrowly distributed poly(methyl methacrylate) standards were used for calibration (*Polymer Standard Services*). Samples were prepared at polymer concentrations of 1.0 gL^{-1}.

Kinetic Model. We used a *Matlab* kinetic model for the calculation of the concentrations of reactants. See Supporting Figure S4 and Supporting notes for detailed discussion.

Cryogenic-Transmission Electron Microscopy (cryo-TEM). Samples for TEM measurement were prepared as stated above. The grids (Quantifoil R2/2 on Cu-grid 400 mesh) were freshly glow-discharged for 30 s before use. Preparation of the grids was performed in an *FEI/Thermo Fisher* Vitrobot at 25 °C with the relative humidity set to 100%. **BCP1** (5 µL) was incubated for 30 s, blotted twice for 3.5 s with a blotting force set to -5. This was followed by plunging of the sample into liquid ethane (pre-cooled by liquid nitrogen). For the measurement and unless not stored in liquid nitrogen, the cryo-TEM grids were transferred into a *Gatan* cryo-transfer specimen holder to insert into the microscope. A temperature of -170 °C of the holder was ensured during the measurement. Cryo-TEM pictures were obtained using a *Jeol JEM-1400 plus* operating at 120 kV and were recorded in a low-dose mode using a CCD camera.

Interfacial Surface Tension (IFT). The interfacial surface tension between the aqueous **BCP1** system and air was determined using the video-based optical contact angle measuring system *OCA 25* (*Dataphysics*), using the software *SCA-22* pendant drop right. 1 mL *Braun* disposable syringes and a regular needle of 0.8 mm radii were used. The measurements occurred at the stated time points and were repeated 10 times.

Fluorescence spectroscopy. Nile Red assay studies were performed on a Jasco FP-8300 fluorescence spectrophotometer with an external temperature control (*Jasco MCB-100*). The samples were directly prepared in a 10 mm quartz cuvette from *Precision Cells Inc.* by mixing 5 mM **BCP1** solution with 5 mM EDC and 2.5 µM Nile Red. The fluorescence intensities were measured over time, each minute, at 635 nm with an excitation at 550 nm. The normalized values were obtained by division through the blank prebleached fluorescence intensity values.

Dynamic Light Scattering (DLS). The scattering behavior of the micellar assemblies was detected on a *Malvern Zetasizer Nano ZS* using a laser wavelength of 633 nm in disposable cuvettes (PS). The measurement for 5 mM **BCP1** solution with and without 5 mM EDC were performed using 5 acquisition times of 20 s.

Electrospray Ionization Mass Spectrometry (ESI-MS). The ESI-MS spectrum was recorded on a *Thermo Scientific LGC Fleet* spectrometer by *Thermo Fischer Scientific*. The analysis of mass was carried out with the *time-of-flight* method.

Nuclear Resonance Spectroscopy (NMR). NMR spectra were recorded on a *Bruker AVIII-300*, *Bruker ARX 300* and *AVIII-500-cryo* spectrometer by *Bruker Analytik* at 25 °C and a frequency of 300/300/500 MHz, respectively. Chemical shifts δ are reported in ppm and are referred to the residual solvent peak of the used deuterated solvent (in case of chloroform-d$_1$ 7.26 ppm (^{1}H) and 77.2 ppm (^{13}C), acetonitrile-d$_3$ 1.94 ppm (^{1}H)). The abbreviation of the signal multiplets are as followed: s-singulet, d-dublet, t-triplet, m-multiplet. The coupling constant J is stated as average value in Hz and refers to coupling between two protons. The degree of polymerization refers to the amount of monomer units found comparing the ratio of the styrene (Aryl-H) and PEG (CH$_2$) signal in the ^{1}H-NMR spectrum. *Endo/exo* diastereomer distinguishment as well as *endo/exo*-ratio was determined referring to the *J*-coupling and the integration of the CH-group at 2.56 ppm.

Time-lapse photography. In a 2 mL HPLC vial, 500 µL of the polymer precursor solution fueled with or without EDC were imaged with a high-definition camera. Time-lapse software was programed to image the sample in a 5 min interval. The investigation of the **BCP1**'s foaminess was performed by vortexing the solution for 1 min prior to the time-lapse video.

Supporting Tables

Supporting Table S1. Characterization of reagents and products.

Substance	Structure	Retention time [min]	Calibration value [mAUmM^{-1}]
EDC		1.38 (method 1)	1.75 (220 nm)
BA		2.38 (method 1)	0.37 (254 nm)

Supporting Table S2: Summary of rate constants for the reaction cycle of **BCP1** fueled with different batches of fuel.

k_0 [s^{-1}]	k_1 [M^{-1}s^{-1}]	k_2 [s^{-1}]	k_3 [s^{-1}]	k_4 [s^{-1}]
1.35E-5	1.3	1*k_1	0.4*k_1	1.4E-4
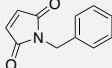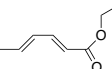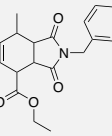
Supporting Table S3: Interfacial Tension (IFT) of 5 mM **BCP1** solution with and without the addition of 5 mM EDC after 10 min, 6 h and 12 h. The error shows the standard deviation from the average (n = 10).

Conditions	Interfacial Tension [mNm^{-1}]
100 mM MES	68,17 ± 0,23
5 mM BCP1	55,60 ± 0,21
5 mM BCP1 & 5 mM EDC after 10 min	52,13 ± 1,44
5 mM BCP1 & 5 mM EDC after 6 h	56,79 ± 0,32
5 mM BCP1 & 5 mM EDC after 12 h	56,81 ± 0,18
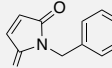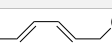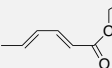
Supporting Table S4. Characterization of Diels-Alder reaction of **1** and **2a** resulting in **3a**.

Substance	Structure	Mass calc. [gmol^{-1}]	Mass obs. [gmol^{-1}]	Retention time [min]	Calibration value [mAUmM^{-1}]
1		187.06 $C_{11}H_9NO_2$	188.10 [Mw+H]$^+$	2.85 (method 3)	2.12 (254 nm)
2a		98.07 $C_6H_{10}O_2$	140.87 [Mw+H]$^+$	1.60 (method 3)	1.54 (254 nm)
3a		285.14 $C_{17}H_{19}NO_3$	286.10 [Mw+H]$^+$	2.40 (method 3)	1.44 (254 nm)

Supporting Table S5. Characterization of Diels-Alder reaction of **1** and **2b** resulting in **3b**.

Substance	Structure	Mass calculated [gmol⁻¹]	Mass observed [gmol⁻¹]	Retention time [min]	Calibration value [mAUmM⁻¹]
1		$Mw = 187.06$ $C_{11}H_9NO_2$	188.10 [Mw+H]⁺	2.85 (method 3)	86.40 (220 nm)
2b		$Mw = 140.08$ $C_8H_{12}O_2$	140.87 [Mw+H]⁺	4.06 (method 3)	17.93 (220 nm)
3b		$Mw = 327.15$ $C_{19}H_{21}NO_4$	328.09 [Mw+H]⁺	4.78 (method 3)	13.02 (220 nm)

Supporting Table S6: Solubility and hydrolysis rate constant of Diels-Alder reagents **1**, **2a** and **2b**. The solubility was measured according to the Experimental Methods. The $\pm$ represents the standard deviation from the average (n = 3).

Substance	Structure	Solubility [mM]	Hydrolysis Rate Constant [s⁻¹]
1		2.51 ± 0.75	2.7E-6
2a		147.02 ± 0.61	0
2b		0.25 ± 0.60	3.9E-7

Supporting Table S7: Rate constants for the reaction cycle and Diels-Alder reaction of **1** and **2a** for 5 mM **BCP1** fueled with different batches of EDC.

Conditions	k_5 [s⁻¹]	k_6 [s⁻¹]	k_{cat} [s⁻¹]
w/o EDC	2.7E-6	1.6E-4	0
w/ EDC	2.7E-6	1.6E-4	-8E-3

Supporting Table S8: Rate constants of the Diels-Alder reaction of **1** and **2a** in control experiments.

Conditions	k_5[s⁻¹]	k_6 [s⁻¹]	k_{cat} [s⁻¹]
100 mM MES	2.7E-6	1.6E-4	0
100 mM MES & 10 mM SDS	2.7E-6	1.6E-4	0

Supporting Table S9: Rate constants for the reaction cycle and Diels-Alder reaction of **1** and **2b** for 5 mM **BCP1** fueled with different batches of EDC.

Conditions	k_5 [s^{-1}]	k_6 [s^{-1}]	k_{cat} [s^{-1}]
w/o EDC	2.7E-6	1.5E-6	0
w/ EDC	2.7E-6	1.5E-6	2E-3

Supporting Table S10: Rate constants of the Diels-Alder reaction of **1** and **2b** in control experiments.

Conditions	k_5 [s^{-1}]	k_6 [s^{-1}]	k_{cat} [s^{-1}]
100 mM MES	2.7E-6	0.2E-6	0
100 mM MES & 10 mM SDS	2.7E-6	0.95E-5	0
100 mM MES & 30 mM EDC	2.7E-6	0.22E-6	0

Supporting Figures
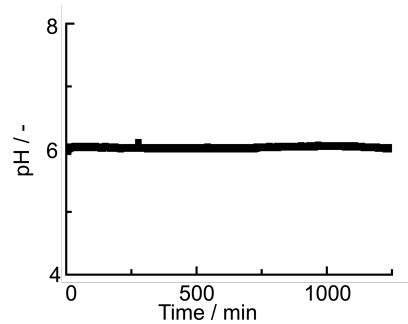
Supporting Figure S1: The pH as a function of time using 5 mM **BCP1** and 30 mM EDC.
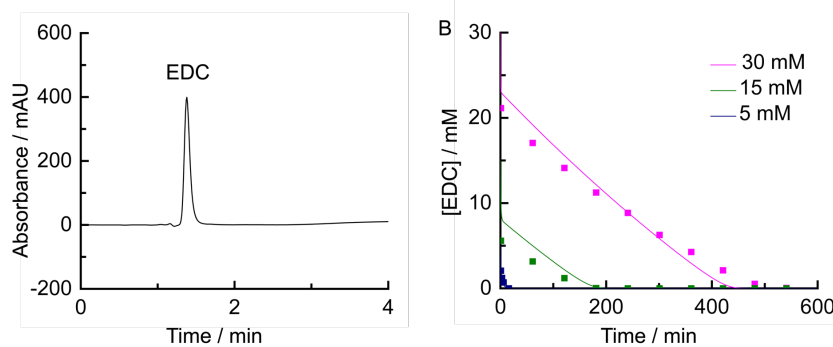
Supporting Figure S2: **A**) HPLC chromatogram at 220 nm of 5 mM **BCP1** fueled with 30 mM EDC. **B**) EDC concentration profile of **BCP1** fueled with different batches of EDC. Markers represents HPLC data, the line represents predicted values from our kinetic model.
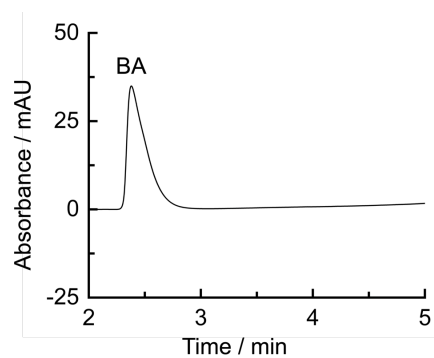
Supporting Figure S3: HPLC chromatogram at 254 nm of 5 mM **BCP1** fueled with 5 mM EDC, diluted 1/1 and quenched with 20 µL of a 40 mM BA stock solution.
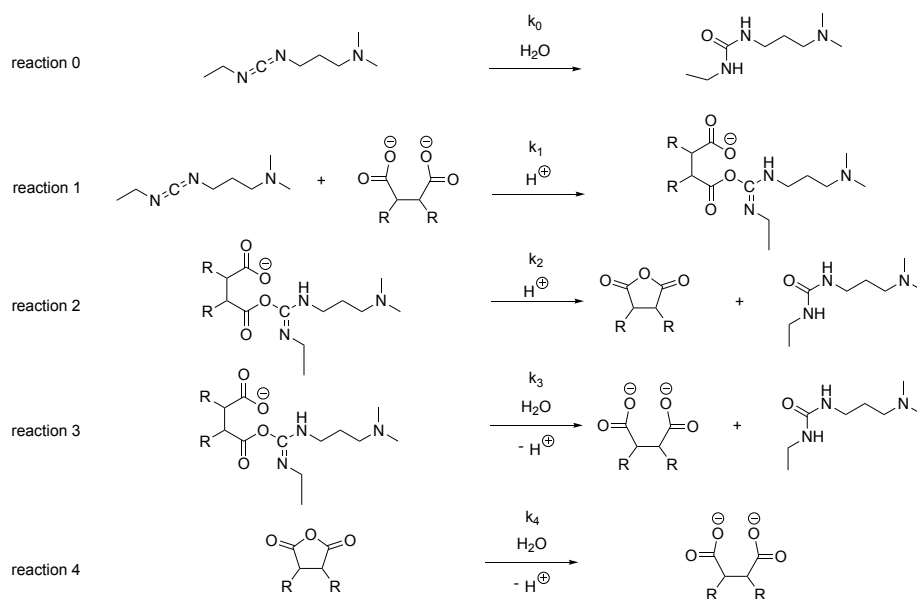
Supporting Figure S4: Schematic representation of the chemical reactions of the kinetic model in the EDC-driven reaction cycle of **BCP1**. (reaction 0) pseudo-first order hydrolysis reaction of EDC. (reaction 1) Second order reaction of the maleic acid precursor with EDC to form the intermediate product *O*-acylisourea. (reaction 2) First-order reaction of the intermediate product *O*-acylisourea to the anhydride product and urea waste product. (reaction 3) Pseudo first-order hydrolysis reaction of the intermediate product *O*-acylisourea to form the initial maleic acid precursor and urea waste product. (reaction 4) pseudo-first order hydrolysis reaction of the maleic anhydride product to form the initial maleic acid precursor. See Supporting Notes for a detailed discussion on the rates and rate constants.
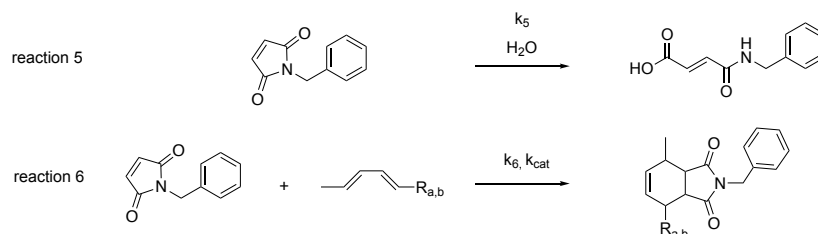
Supporting Figure S5: Schematic representation of the chemical reactions of the kinetic model in the Diels-Alder reaction. (reaction 5) Pseudo-first order hydrolysis reaction of **1**. (reaction 6) Pseudo first-order Diels-Alder reaction of **1** with **2a** or **2b** to form the Diels-Alder product **3a** or **3b**. We considered a pseudo first-order reaction as the dienes **2a** and **2b** were used in excess. See Supporting Notes for a detailed discussion on the rates and rate constants.
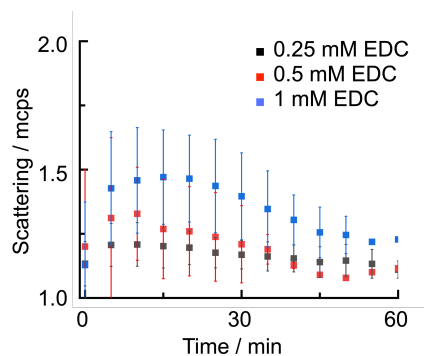
Supporting Figure S6: Scattering rate as a function of time of 5 mM **BCP1** fueled with 0.25, 0.5 and 1 mM EDC. Markers represent DLS data. The error bars show the standard deviation from the average (n = 3).
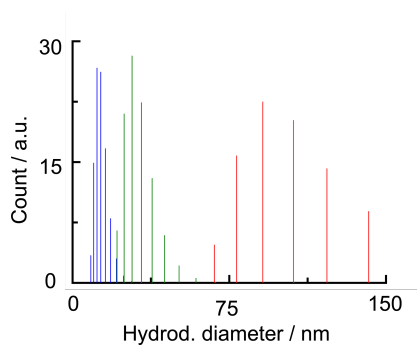

Supporting Figure S7: Size distribution of the hydrodynamic diameter of 5 mM **BCP1** in 100 mM MES before (green), at the scattering maximum at 25 min (blue) and after 24 h (red) after the addition of 5 mM EDC. The size distribution at the maximum scattering is the narrowest.
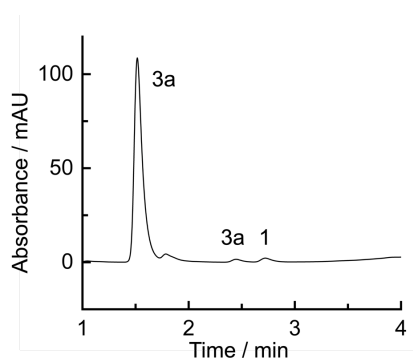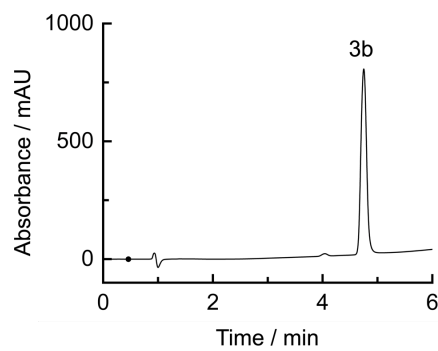

Supporting Figure S8: HPLC chromatogram of the Diels-Alder reaction of **1** and **2a** at 254 nm to form the respective Diels-Alder product **3a**.
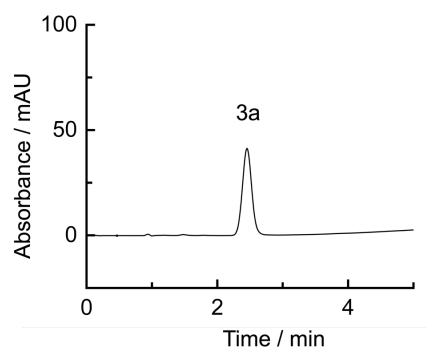
Supporting Figure S9: HPLC chromatogram of the synthesized and purified Diels-Alder product **3a**.
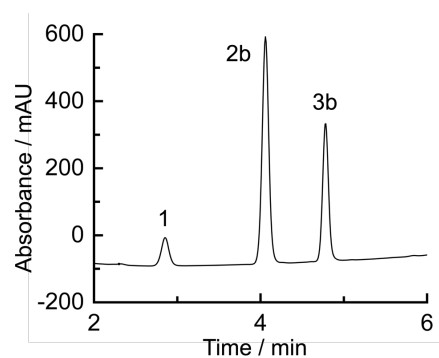
Supporting Figure S10: HPLC chromatogram of the Diels-Alder reaction of **1** and **2b** at 220 nm to form the respective Diels-Alder product **3b**.
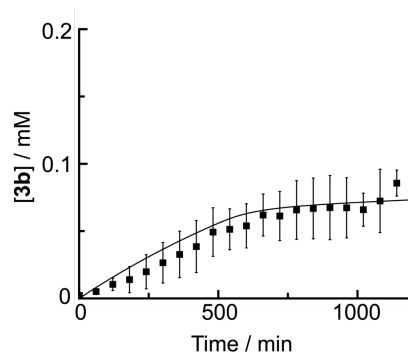

Supporting Figure S11: HPLC chromatogram of the synthesized and purified Diels-Alder product **3b**.
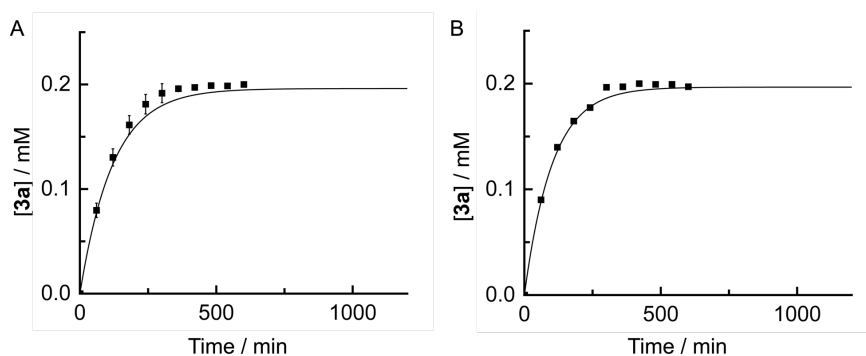
Supporting Figure S12: Diels-Alder product concentration profile of 0.2 mM **1** and 5 mM **2a**. **A**) in 100 mM MES, **B**) 10 mM SDS. Markers represent HPLC data, the line represents predicted values from our kinetic model. The error bars show the standard deviation from the average (n = 3).
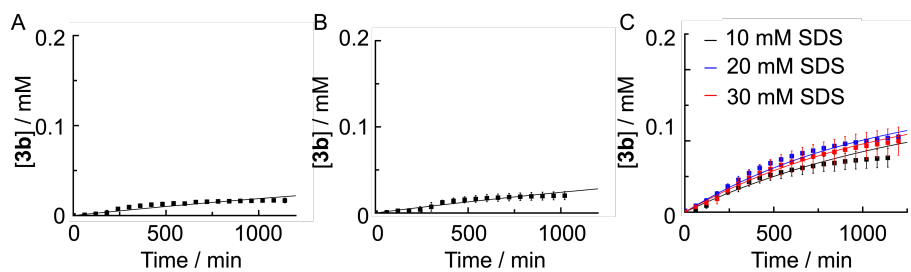

Supporting Figure S13: Diels-Alder product concentration profile of 0.2 mM **1** and 5 mM **2b A**) in 100 mM MES, **B**) in 100 mM MES and 30 mM EDC and **C**) 10, 20 and 30 mM SDS in100 mM MES. Markers represent HPLC data, the line represents predicted values from our kinetic model. The error bars show the standard deviation from the average (n = 3).


Supporting Figure S14: Diels-Alder product concentration profile of 0.2 mM **1** and 5 mM **2b** in 5 mM **BCP1** and fueled with 45 mM EDC. Markers represent HPLC data, the line represents predicted values from our kinetic model. The error bars show the standard deviation from the average (n = 3).
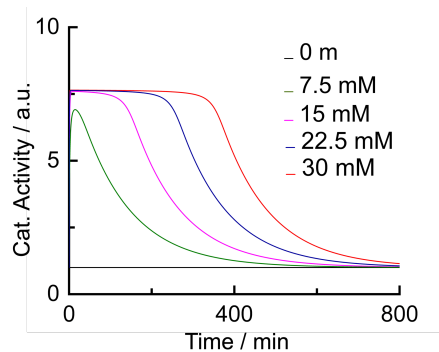
Supporting Figure S15: Quantification of catalytic activity due to **BCP1** fueled with different batches of EDC predicted by our kinetic model. See Supporting Notes for the definition and discussion on the catalytic activity.
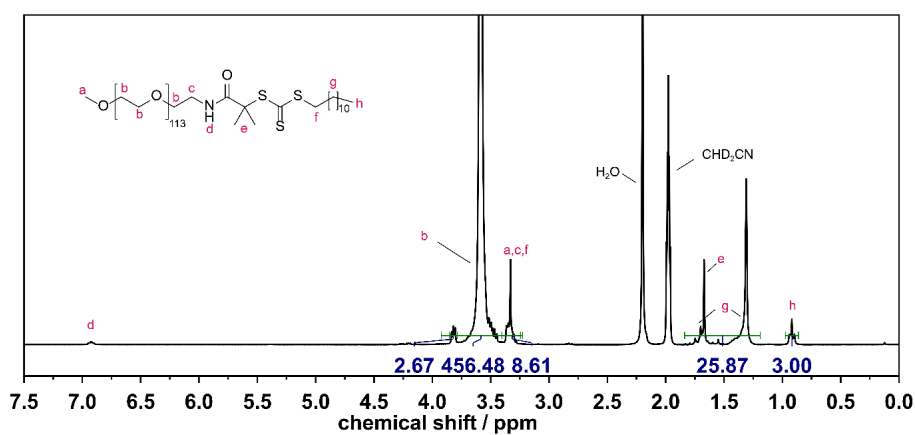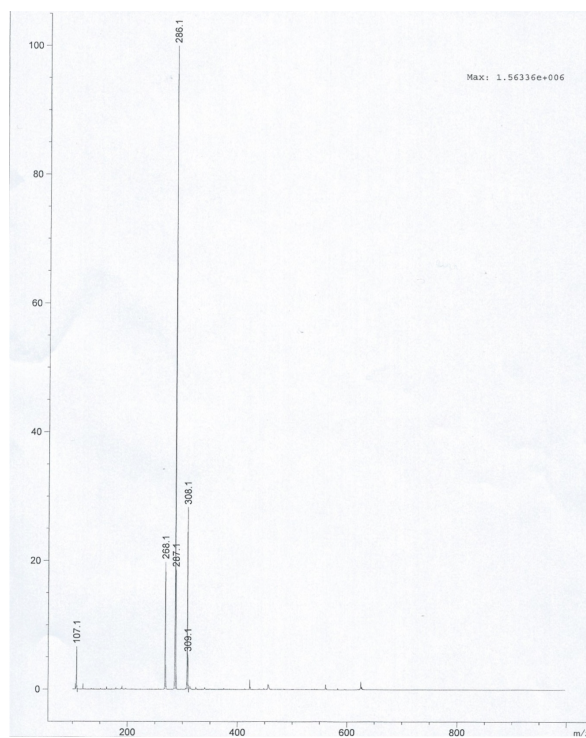

Supporting Figure S16: ^{1}H-NMR spectrum of mPEG$_{114}$-DDMAT (300 MHz, CD$_3$CN). Functionalization is quantitative as determined from the ratio of the methyl signal (h, 3 protons) to the PEG-signal (b, 113 x 4 + 2 = 454 protons). The ^{13}C-satellite signal of signal b is integrated to estimate the integral of the overlapping signals for a,f,c that overlap with the other satellite.
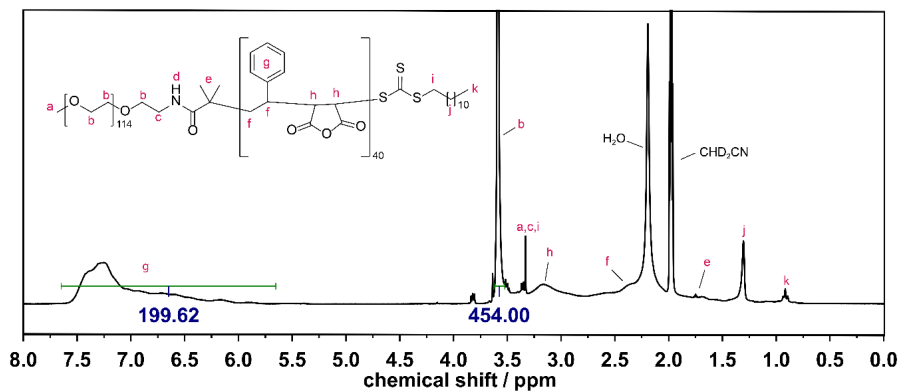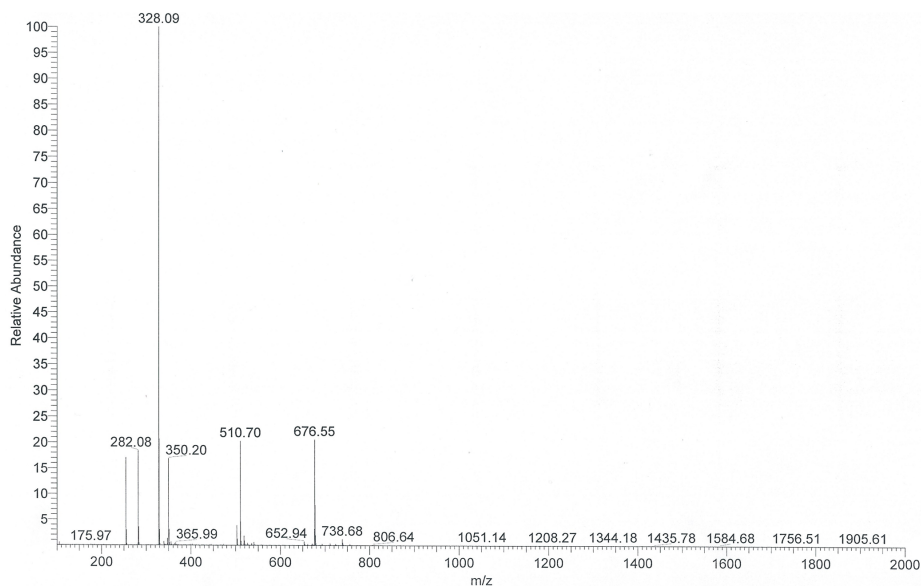
Supporting Figure S17: ^{1}H-NMR spectrum of **BCP1** (300 MHz, 25 °C, CD$_3$CN). The degree of polymerization for the PSMA block was determined from the ratio of the PEG-signal (113 x 4 + 2 = 454 protons) to the aromatic styrene signal (g, 40 x 5 = 200 protons).
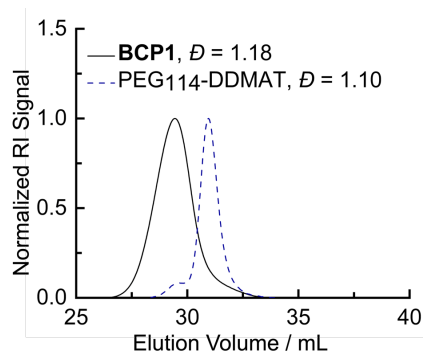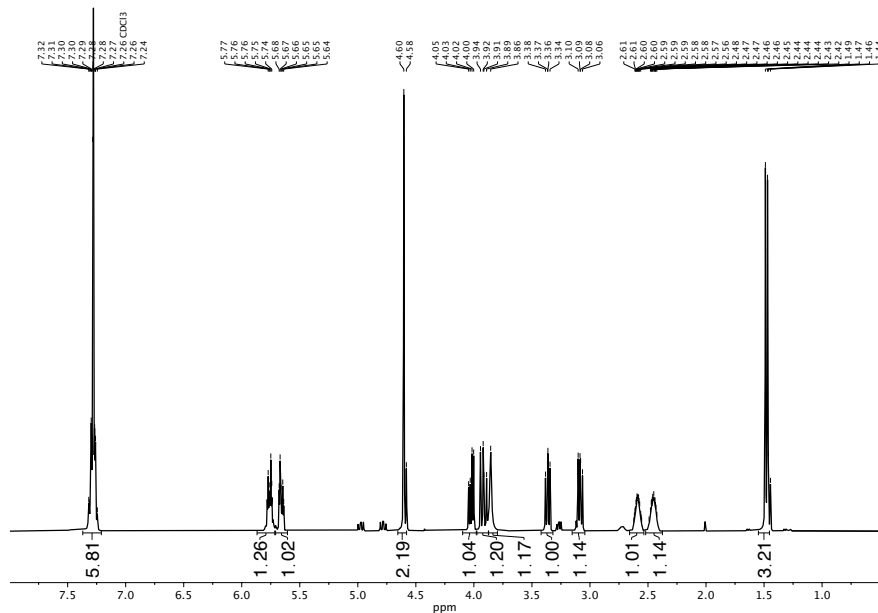

Supporting Figure S18: SEC traces of the PEG$_{114}$-DDMAT and the **BCP1** in DMAc.

Supporting Figure S19: ESI-MS characterization of the Diels-Alder product **3a**.

Supporting Figure S20: ESI-MS characterization of the Diels-Alder product **3b**.

Supporting Figure S21: ^{1}H-NMR (CDCl$_3$, 300 MHz) spectrum of product **3a**. The not integrated signals are assigned to the *exo*-diastereomer of **3a**.
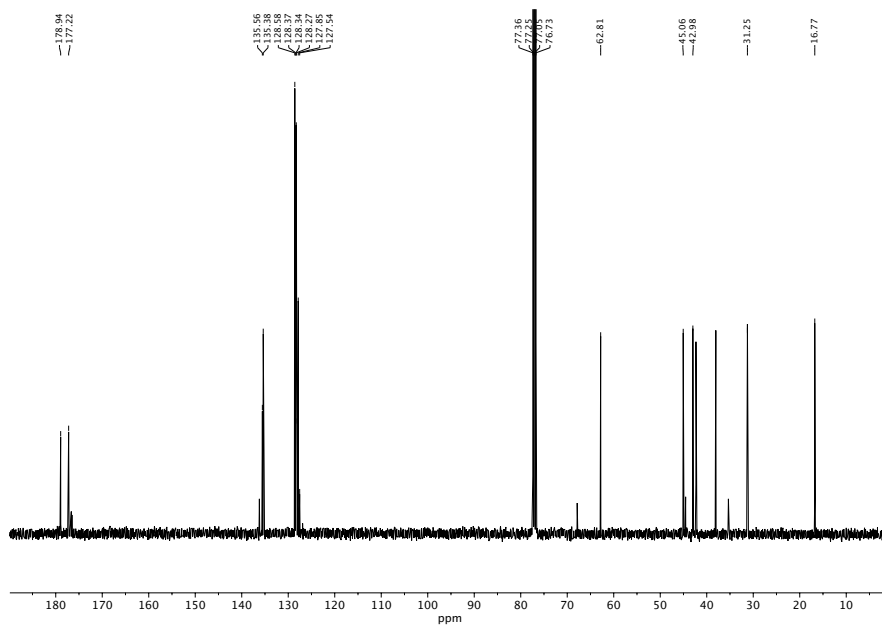
Supporting Figure S22: ^{13}C-NMR (CDCl$_3$, 101 MHz) spectrum of product **3a**. The signals of low intensity are assigned to the *exo*-diastereomer of **3a**.
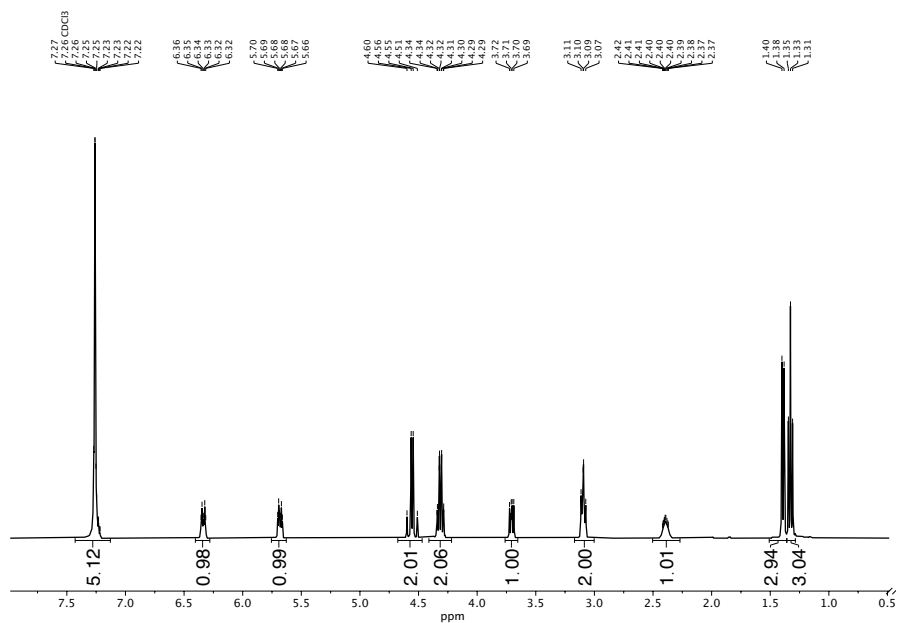
Supporting Figure S23: ^{1}H-NMR (CDCl$_3$, 300 MHz) spectrum of product **3b**.
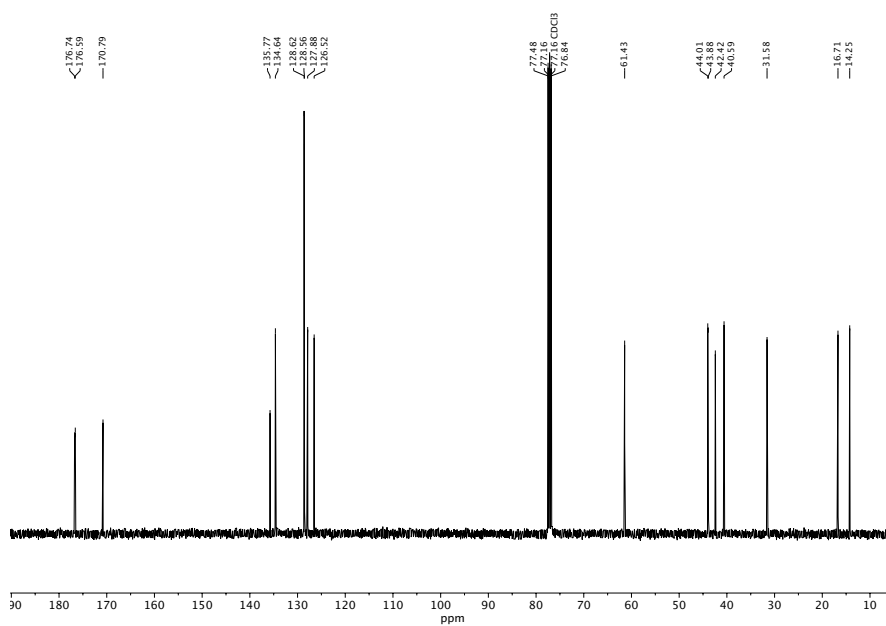
Supporting Figure S24: ^{13}C-NMR (CDCl$_3$, 101 MHz) spectrum of product **3b**.

Supporting Notes

Description of the kinetic model. We used a *Matlab* code as kinetic model to calculate the concentrations of each reactant for every second i in the reaction cycle (maleic acid precursor, fuel, intermediate product, maleic anhydride product). The model is based on five differential equations which represent the five underlying chemical reactions: (1) the pseudo first-order hydrolysis reaction of EDC r_0, (2) the second-order reaction of the maleic acid precursor with the fuel to form the intermediate product, (3) the first-order maleic anhydride formation reaction r_2, (4) the pseudo first-order hydrolysis reaction of the intermediate product r_3, (5) the pseudo-first order hydrolysis reaction of the maleic anhydride product r_4. The rate constants k_0 and k_1 were determined from the experimental HPLC data by monitoring the EDC concentration over time. The rate constants k_2, k_3 and k_4 were determined by fitting.

$$r_0(i) = k_0 \cdot EDC(i) \tag{1}$$

$$r_1(i) = k_1 \cdot EDC(i) \cdot COOH(i) \tag{2}$$

$$r_2(i) = k_2 \cdot COOEDC(i) \tag{3}$$

$$r_3(i) = k_3 \cdot COOEDC(i) \tag{4}$$

$$r_4(i) = k_4 \cdot COOOC(i), \tag{5}$$

The kinetic model also calculated the concentration of the Diels-Alder products **3a** and **3b** for every second in the reaction cycle. We used the dienes **2a** and **2b** in excess to have pseudo-first order reactions which are solely dependent on the concentration of the dienophile **1**. The following three differential equations were used as a basis for the calculation: (6) the pseudo-first order hydrolysis reaction of the dienophile **1**, (7) the pseudo-first order reaction of **1** to form the Diels-Alder products **3a** and **3b**. The rate is based on the rate constant k_6 of the reaction in the absence of fuel to which a k_{cat} in dependence on the respective anhydride concentration is added. (8) the variable *cat(i)* was used to quantify the catalytic activity due to **BCP1** after addition of fuel in relation to the reaction without fuel (see Supporting Figure S15). The hydrolysis rate constant of **1** was determined experimentally by HPLC and can be seen in Supporting Table S7-S10. The rate constants k_6 and k_{cat} of the Diels-Alder reaction were determined by fitting the evolution of the product concentration **3a** and **3b** derived by HPLC.

$$r_5(i) = k_5 \cdot \mathbf{1}(i) \tag{6}$$

$$r_6(i) = \left(k_6 + k_{cat} \cdot COOOC(i)\right) \cdot \mathbf{1}(i) \tag{7}$$

$$cat(i) = \left(k_6 + k_{cat} \cdot COOOC(i)\right)/k_6 \tag{8}$$

References

[1]   S. Harrisson, K. L. Wooley, *Chem. Commun.* **2005**, 3259.
[2]   F. Schnitter, J. Boekhoven, *ChemSystemsChem* **2021**, *3*, e2000037.

5 Approaches toward designing self-healing materials

Abstract

In the previous chapters, we learned that chemically fueled self-assembly can be used to control materials over time. Another interesting feature is that chemically fueled supra-molecular materials can self-heal, which I explore in a later chapter. But first, in the following chapter, I introduce the state-of-the-art of self-healing materials. During the last decades, material scientists showed increased interest in designing self-restoring materials. Besides the urge to create materials similar to nature's complexity, i.e., life-like, autonomously behaving materials, a self-healing feature improves the material's longevity, thus, establishes decreased maintenance and costs and improves safety and resource conservation. Self-healing has been observed in various synthetic materials, such as glass, metals, or polymers since the last century. However, the healing driving force or mechanism often remained unclear and challenging to design. In principle, self-healing can occur autonomously or not, being intrinsically or extrinsically driven. I present examples of materials that self-heal based on, e.g., healing agent microencapsulation strategy, dynamic reversible covalent bond exchange reactions (dynamers or vitrimers), or reversible network formation (supramolecular materials). Though the latter examples showed an increased dynamic behavior, they were still far away from operating autonomously like biological systems. Such systems like the cytoskeleton's microtubule show that chemically fueled self-assembly can lead to autonomous self-healing. Despite one rare synthetic example of self-healing chemically fueled fibers, we still lack a fundamental understanding of its mechanism. By understanding how self-healing is conducted in nature, and unraveling dictating mechanisms, we may create materials able to self-heal comparable to living systems.

5.1 Non-biological self-healing materials

During the last decades, the urge to create materials that can self-restore their functionality (or structure) became especially appealing, particularly in interdisciplinary fields of regenerative medicine, building construction, architecture, aerospace, robotics, and so forth.[81, 82] However, materials that show inherent self-healing behavior are not a completely recent discovery. Early records state that already 2000 years ago, during the Roman Empire, self-healing concrete of buildings and constructions was observed.[83-85] Damages or cracks in the micrometer range within the concrete repaired themselves by the intrinsic hydration of unhydrated cement particles.[86] A similar process was discovered by Lord Rayleigh in 1937, demonstrating self-healing glass after external rupture.[87] Decades later, Wiederhorn and Townsend explained that this process of self-healing glass originates in highly active dangling bonds in contrast to the strained silicon-oxygen bond.[88]

In 1956, Broom and co-workers observed self-healing metallic alloys.[89, 90] It was soon studied that this healing effect was caused by temporally local (and directional) mobility of atoms towards the defect or crack zone, consequently filling this defect site.[91]

In the field of polymer chemistry, self-healing was also frequently observed. Voyutskii and Vakula studied the self-adhesion of polymer-polymer solid phases according to diffusion processes and set this in relation to their glass transition temperature (T_g) and degree of cross-linkage in the 1950s.[92] Early assumptions indicated that self-healing of any polymer matrix could generally be possible if taken place above the glass transition temperature, where molecular mobility is higher.[82] For instance, Gerry and co-workers observed crack healing of a cast epoxy resin at elevated temperatures (Figure 6A).[93] In the 1970s, Wool and co-workers demonstrated that viscoelastic polymers such as hard polypropylene (HPP) overcame interlamellar microvoids induced by stretches. Similar healing effect was observed in cracks in polystyrene or microvoids in poly(styrene-butadiene-styrene) (SBS) block copolymers.[82] Later studies considered that a healing effect originated in the energy balance between work and strain energy, viscous dissipation, and damage. Herein, the stretches presumably caused a redistribution of energies and a conversion of surface energy and mechanical work resulting in the healing of the damage.[94, 95] One bold yet captivating self-healing study was performed by Fall and Kalista and co-workers, demonstrating the self-healing of poly(ethylene-*co*-methacrylic acid) copolymers (EMMA) plates (thickness = 1 mm) after a projectile puncture.[96-98] The hole caused by the bullet merged within seconds, faster than could be tracked by eyes (Figure 6B). The most important lesson of this study was that the heat generated by the mechanical rupture of the bullet led to the melting of the polymer located adjacent to the entry point, initiating the healing process. Or in other words, the damage to the polymer plates triggered the healing. Especially the latter polymeric examples demonstrated that

understanding the interplay of molecular mobility and inter-diffusional operation combined with phase-phase interchange processes could help to design self-healing materials. Though these phenomena or observations were mostly restricted to small damages and dependent on, e.g., the presence of water, it perfectly illustrates how inherent self-healing mechanisms lead to self-repairing materials. In principle, a diversity of material classes can self-heal. However, it also hints that the material's morphology, i.e., soft or hard matter, is a decisive factor in accomplishing the self-healing process. Moreover, the type and manner of healing can vary drastically, for instance, if the healing mechanism proceeds intrinsically or extrinsically, or entirely autonomously.
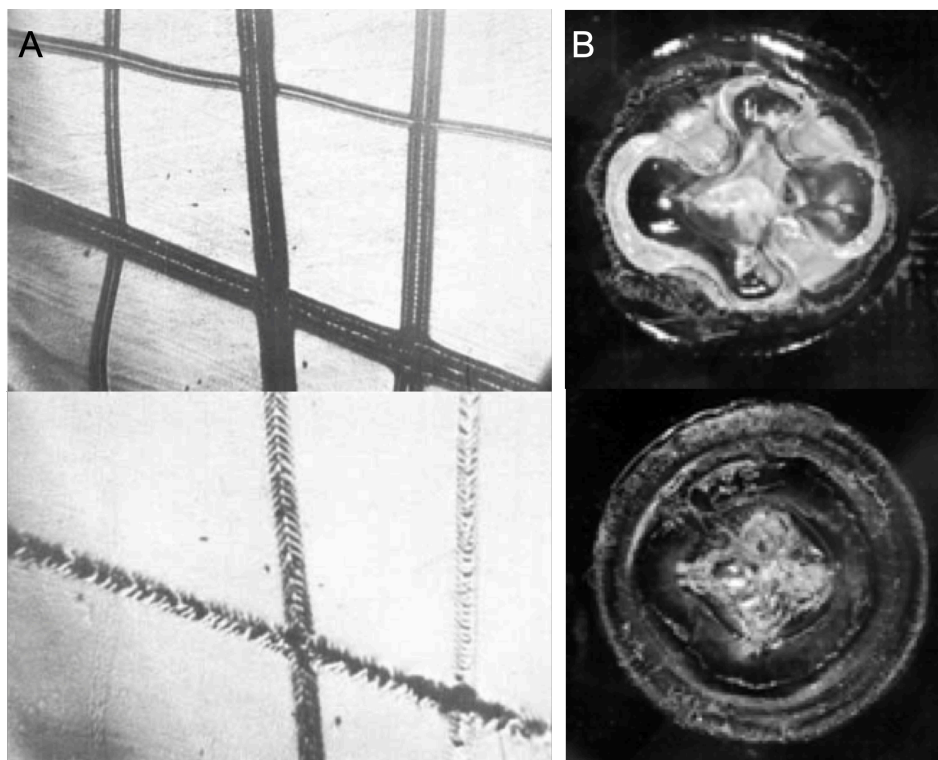

Figure 6: Observations of self-healing polymeric materials. **A**) Top: Damaged cast epoxy resin surface after scratches. Bottom: The same damaged epoxy surface after heating (200 °C) for 12 hours. The scratched surface was partially restored. Reproduced with permission from ref. 93. Copyright 1969 Taylor and Francis. **B**) Top: Damaged and healed site of an EMMA plate after disc penetration at 20 °C. Bottom: Damaged and healed site of an EMMA material after disc penetration at 130 °C. An increased elastic recovery response was observed at higher temperatures. Reproduced with permission from ref. 97. Copyright 2013 Royal Society of Chemistry.

5.2   Classification of self-healing materials

Self-healing materials can be characterized by the ability to regenerate their initial functionality after applied mechanical, thermal, or ballistic damage.[82] The goal is to restore the material's

original properties rather than recover the initial morphology.[81] During the last decades, a plethora of self-healing materials have been described, covering various material classes, including metals, ceramics, and their composites, polymers, and supramolecular materials.[81, 82, 99, 100]

Most of them combine a similar basic healing process: 1) The production of a mobile phase that serves as a healing agent, which is generated by either the damage itself or triggered by an external stimulus. 2) The mass transport to the ruptured site is followed, initiating the repair reaction or process, either by physical interactions or chemical reactions.[81]

We differentiate between two types of self-healing materials depending on the trigger and the nature of the healing process: the healing can proceed autonomously or not. While non-autonomous systems require an external trigger or environmental change, e.g., pH, light, temperature, or a mechanical one, autonomously healing materials heal without intervention or external stimuli.[83] The damage itself triggers the healing process.[81] One of the most prominent examples of autonomous healing is human tissue.

Furthermore, we refer to two further sub-categories: intrinsic versus extrinsic self-healing. The latter needs to apply external healing agents, e.g., micro- or nanocapsules embedded into the matrix. If damaged, the breakage of the capsules releases the filling (the mobile phase). In contrast, intrinsic healing materials are designed without external healing agents located in the matrix and heal by, e.g., reversible bond formation (see 5.3.2).[81, 83, 101]

In recent years, specific interest has grown in smart materials that can be used in autonomous or biomimetic robotics and actuators. In these systems, self-healing of soft as well as hard matter is of particular interest, though self-healing hard matter shows its challenges due to, e.g., restricted diffusion processes.

In the following section, I have a deeper look at state-of-the-art materials demonstrating landmarks in the man-made creation of self-healing materials.

5.3 Landmarks in artificial self-healing materials

5.3.1 Self-healing materials based on encapsulation

One of the first self-healing materials, being (semi)-commercialized, was described by Dry, Sottos and co-workers.[102-105] They presented a universal approach of hollow fiber-filled composites, embedded in either polymer or concrete matrix. Herein, the fibers are filled with a reactive agent that is released in the case of damage. As the location of mechanical trauma is equal to the damaged site of the fibers, the released healing fluid is available on spot. In other words, the 'glue' for repairing the material is already incorporated into the material's network. The following criteria were classified as crucial for successful healing: Fibers containing a

healing agent, a significant trigger to release the agent, a fiber coating with a wall that is damaged by applying the trigger, and the healing agent can initiate the self-repair process. This concept showed a high degree of customizability of its design and components, e.g., fiber design, fiber amount, healing agent, or fiber coating.

A similar autonomous approach to self-healing was realized by White et al., by applying microcapsules filled with healing fluid instead of fibers in an epoxy matrix.[104, 106, 107]

Indeed, the field of stimuli-responsive capsules has drawn much attention in the last decades as they can be applied for, e.g., nutrient preservation, fragrance release, drug delivery, and, most interestingly, self-healing. Besides mechanical rupture, other mechanisms triggering the capsule release were reported based on biological, photo, thermal, electrical, magnetic, or chemical stimuli.[108-112] The self-healing based on microencapsulation adhered to similar principles already presented by Dry et al. — a rupture of the material led to the breaking of the microcapsules located at the fracture and consequently to a release of the healing agent (Figure 7A).[104] Due to capillary forces, the low-viscous fluid flowed to the cracked site and repaired it. The twist laid in incorporating a catalytic trigger into the epoxy matrix. As the fluid, e.g., a monomer, gets in touch with the catalyst after rupture, polymerization occurs and mends the damaged site. This self-healing concept showed great versatility since applying living polymerization catalysts and creating several healing events was possible. This concept was expanded in collaboration with Moore and co-workers to programmable microcapsules containing a self-immolative shell.[113] Herein, the capsule shell wall consisted of self-immolative polymers that depolymerize by a head-to-tail mechanism after removal of a triggering end group such as a carbamate protecting group (Figure 7B). The addition of hydrochloric acid (HCl) or piperidine led to the decomposition of the shell and to the release of the filling. This predictable chemical system could be applied as drug delivery platforms or in Li-ion batteries. Though an attractive concept, fibers as well as microcapsules have drawbacks since both geometries did not result in the greatest healing efficiency.[81] Moreover, the autonomous healing process was restricted to one distinct damage per considered location. Once the microcapsules were ruptured, and the healing agent discharged, multiple healing cycles were hardly achievable. Although the latter was tried to be overcome by applying, e.g., re-mendable cross-linked polymers to increase the number of healing cycles, the external pressure or heat needed for the mending process diminished the autonomous aspect.[114]

In later studies, White, Moore, and co-workers expanded the concept of self-healing microcapsules by adapting to a bio-mimicking approach, inspired by microvascular networks.[115] They approached autonomous self-healing of a ruptured network based on a penetrating three-dimensional microvascular coating-substrate network imitating human skin (Figure 7C). The network is filled with a healing fluid while catalyst particles are embedded into

an epoxy coating. As damage occurs in the coating, a healing fluid, e.g., dicyclopentadiene, (DCPD) is discharged by the microvascular network toward the crack site. The contact with the Grubbs II catalyst incorporated in the coating started the polymerization and repairing process. This way, self-healing at the same location was feasible for up to seven cycles.
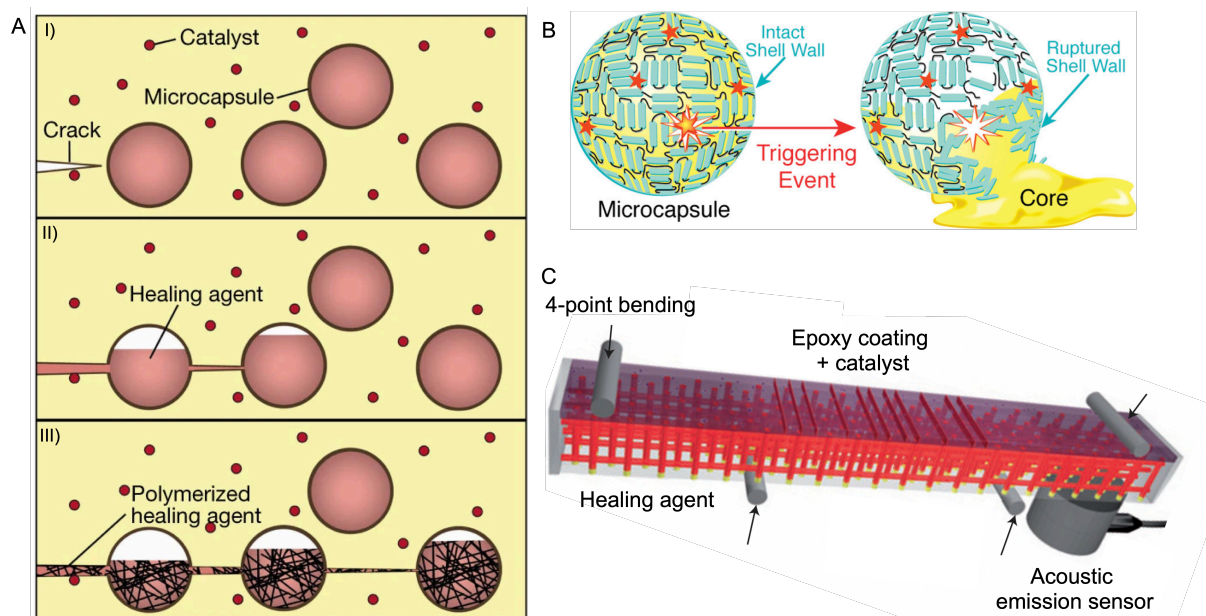

Figure 7: Self-healing according to microcapsules and microvascular networks. **A**) Microencapsulation healing concept based on a catalyst and encapsulated healing agent loaded composite matrix. I) Damage, e.g., a crack within the network occurs. II) If the crack prolongs and encounters a microcapsule, its breakage leads to the release of the healing agent toward the composite matrix due to capillary forces. III) By contacting the embedded catalyst, the liquid healing agent starts polymerizing, resulting in the mending of the damage. Reproduced with permission from ref. 104. Copyright 2001 Nature Publishing Group. **B**) Schematic illustration of a programmable microcapsule based on a self-immolative shell (turquoise) containing a trigger group (star) that gets stimulated by, e.g., a change in pH, resulting in the depolymerization of the shell and the discharge of the filling. Reproduced with permission from ref. 113. Copyright 2010 American Chemical Society. **C**) Schematic illustration of a self-healing network inspired by the capillary network in the dermis layer of skin. It contains a microvascular substrate filled with a healing agent coated with a catalyst-loaded epoxy matrix. A four-point bending method initiates cracks at the coating surface where the tensile stress is highest. The cracks perpetuate to the coating-substrate surface and capillary forces lead to the release of the healing agent and polymerization of the agent. Reproduced with permission from ref. 115. Copyright 2007 Springer Nature.

5.3.2 Self-healing materials based on dynamic covalent bond formation

The previous examples showed that an effective self-repair of damaged materials is feasible by relying on an extrinsically applied healing agent to heal the damage. The damage initiates chemical reactions leading to newly formed irreversible covalent bonds and connectivity, i.e., the material mends and self-repairs. Though offering versatility in terms of the healing agent's

chemical compositions, the initial material (matrix) behaves static at ambient conditions and mostly relies on highly reactive reagents or chemical reactions, just as in the case of most irreversibly formed polymers. In other words, the driving force necessary to re-connect the network is missing. However, if the material itself was of dynamic nature, i.e., based on reversible connectivity and network formation, the material should be capable of self-restoring a defect or damaged site. Therefore, other approaches to designing self-healing materials specifically targeted the driving forces of reversible bond formation and connectivity. Hence, the intrinsically dynamic nature of supramolecular materials served as inspiration. Here, the dynamism is directly linked to the reversibility and, thus, the relative weakness of non-covalent interactions like hydrogen bonds, π-π-stacking, and others. By operating in equilibrium, these systems can be considered static and thermodynamically stable, though potentially offering conceptual requirements, such as reversibility, to design self-healing materials.

Dynamic polymers, so-called dynamers, depict a new class of material chemistry combining dynamic constitutional chemistry with molecular chemistry inspired by the dynamically behaving class of supramolecular chemistry.[116] This results in a steady constitutional amendment based on building block exchange and re-arrangement, likewise realized reversibly by covalent bonds. Though Jean-Marie Lehn stated that dynamers "may be either of molecular or supramolecular nature depending on whether the connections are reversible covalent bonds or non-covalent interactions"[117], I primarily focus on molecular dynamers based on reversible covalent bonds in this section (for supramolecular materials see 5.3.3). The dynamic character of the material is achieved by introducing covalent bonds that reversibly form and cleave, i.e., labile chemical bonds, responding to an external stimulus, e.g., heat, light, or chemical additives.[118] The most prominent reversible reactions include, e.g., imine type or disulfide bonds, reversible 4+2 cyclo-additions, and Diels-Alder (DA) reactions. Specifically, DA-reactions were considered a promising tool in developing a trigger-induced material to exert self-healing behavior.[116] For instance, Wudl and co-workers reported a self-healing macromolecular network formed by thermally DA-cross-linkage of PA-MI (polyamide maleimide) and PA-F (polyamide furan).[114] As a robust polymeric material at ambient temperature, it can mend under elevated temperatures (120 °C). After mechanical trauma, heat initiates the DA-reaction, resulting in the healing of the fractured part for even multiple times. Around 30% of cross-linkage is disconnected at elevated temperatures and re-connects upon cooling. Though this system showed beneficial traits, e.g., not relying on catalysts or externally added monomers, elevated temperatures are needed to trigger the DA-reaction.

In contrast, Lehn and co-workers set an example for a self-repairing polymer based on reversible DA reaction under ambient conditions. Bis(fulvene) and bis(dicyanofumarate) terminated polydispersed polyethylene underwent a reversible DA-reaction resulting in a

stretchable polymer film at 25 °C.[119] After cutting the film and overlapping the pieces under slight pressure, the re-adjusted polymer film was stretchable, assuming self-healing at the polymer's interfaces.

During the 2010s, Leibler and co-workers significantly impacted the development of dynamic polymers, also called vitrimers. Though conceptually showing no difference to dynamers, the Leibler group specifically studied dynamic covalent bond formation based on associative dynamic bond-exchange processes, i.e., transesterification, transamination, transcarb-amoylation, or olefin metathesis.[120] They subordinately belong to the family of Covalent Adaptable Networks (CANs), previously introduced by Bowman and others, and specifically distinguish themselves by greatly cross-linked polymer networks with silica-like fluidity.[121-124] Dynamic covalent bonds are introduced into a cross-linked network and, thus, enable a dynamic and reversible re-arrangement of connectivity in response to external stimuli (Figure 8).[125] Therefore, vitrimers combine the best traits of thermoplastics and thermosets, i.e., recyclability and robustness.[126] Though the complete network is re-organized, the number of cross-links is kept constant.[121] Vitrimers own great mobility and flow above T_v (freezing transition temperature) while showing robust, thermoset-like features underneath this specific temperature. Therefore, they feature strong mechanical robustness while simultaneously showing dynamic behavior (autonomously or stimulus-induced), which gives them significant qualities, e.g., weldability, recyclability, and on a more sophisticated level, the ability to self-heal.[127]

One early example of such a self-healing polymer was presented by the Leibler group which designed an epoxy thermoset based on a thermally-responsive metal-catalyzed transesterification exchange reaction.[128] The polymeric system consisted of an epoxy-acid network formed by diglycidyl ether of bisphenoal A (DGEBA) and a mixture of di- and tricarboxylic fatty acids catalyzed by zinc acetate ($Zn[ac]_2$). A key feature is that the transesterification kinetics are fast at high temperatures (over T_v). In other words, elevated temperatures lead to fast exchange reaction rates and malleability of the material in contrast to a secured connection and elastomer-like features at ambient temperatures. Herein, the exchange reaction rates are tuned by the type and amount of used catalyst.[121] Therefore, damage within the network was overcome by heating the material, leading to the formation of multiple transesterification products that, again, formed a dense cross-linked network upon cooling.
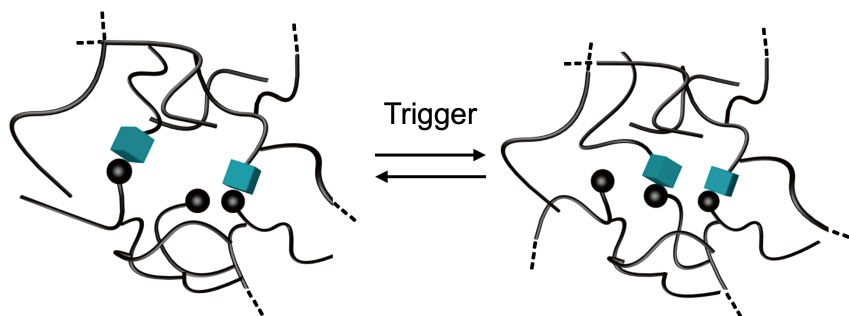
Figure 8: Dynamic covalent bond formation to induce self-healing. Schematic illustration of general molecular network re-arrangement in vitrimers. The topology is changed upon an externally induced trigger, e.g., heat. Reproduced with permission from ref. 125. Copyright 2019 Royal Society of Chemistry.

5.3.3   Self-healing supramolecular materials

In contrast to the studies on dynamic covalent bond formation yielding in self-repairing behavior, supramolecular chemistry's dynamic and reversible character offers great conditions to induce self-healing features. Structure formation and healing mechanisms in biological systems often rely on non-covalent interactions like hydrogen bonds, host-guest interactions, metal-ligand coordination, or hydrophobic effects. That way, the formation of labile yet strong bonds is feasible, leading to a dense but reversible network.

Multitopic molecules, i.e., molecules exerting directional non-covalent bonds due to, e.g., functional hydrogen bond acceptors or donors, are a promising tool to create supramolecular networks containing long-lived, cross-linked chains while owning polymer-like properties.[127, 129] For instance, a mixture of ditopic and multitopic molecules can interact/associate in more than one axis based on acceptor-donor concepts and thus form a strongly cross-linked network.[130] In most polymeric cases, the obtained material resembles thermoplastics rather than elastomers and is prone to crystallization. Therefore, precise control and fine-tuning of the hydrogen-bonding functional units are important for balancing strong directionality and cross-linkage while preventing phase separation and crystallization. Following this concept, Leibler and co-workers reported a self-healing thermo-reversible rubber based on supramolecular self-assemby.[127, 131, 132] The thermoplastic elastomer consists of a mixture of oligomers containing self-complementary and complementary hydrogen bonding groups, e.g., amidoethyl imidazolidone, di(amidoethyl) urea and diamido tetraethyl triurea. After damage, mostly hydrogen bonds are broken but can be re-installed due to the reversible nature of the non-covalent interactions (Figure 9A).[127] The system self-heals through self-adhesion, providing the damaged sites are slightly pressed together (Figure 9B). This concept was also used (and commercialized) for producing self-healing automotive repair coatings, resulting in a surface polish in the case of cracks.[81]
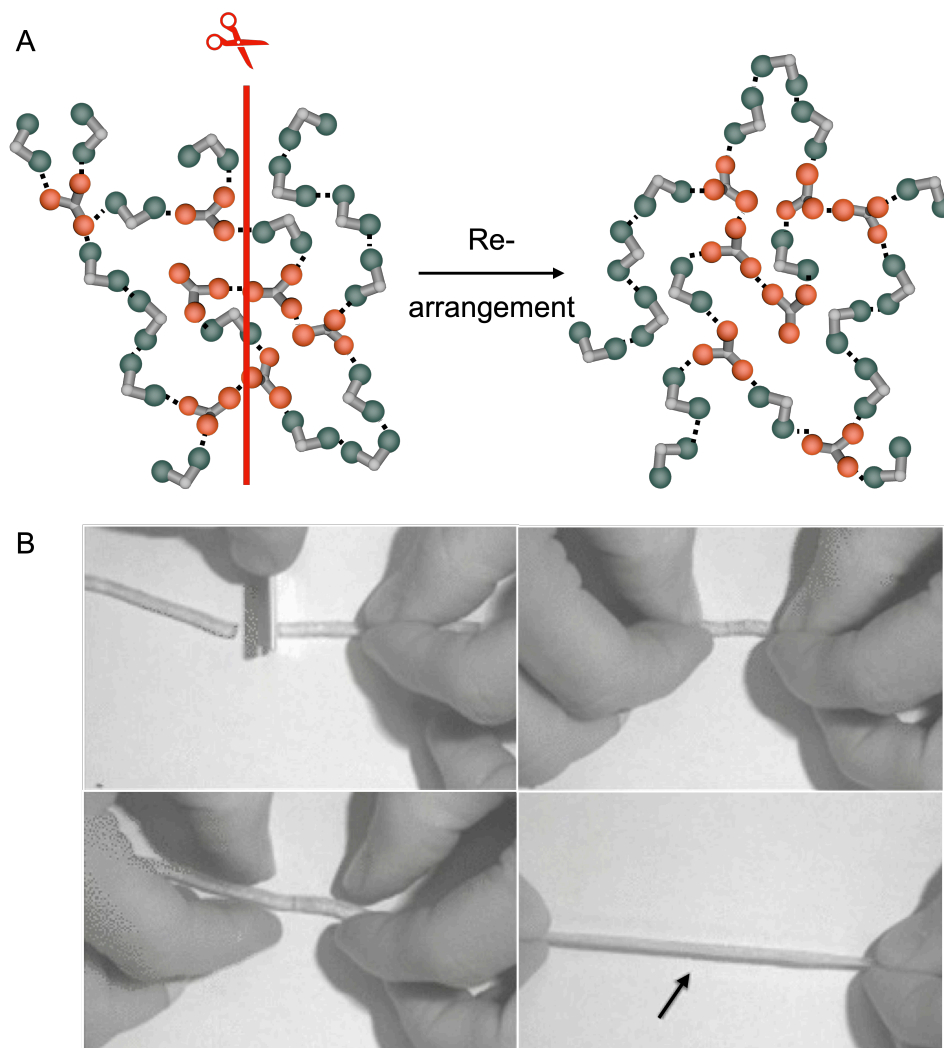
Figure 9: Self-healing based on non-covalent interactions. **A**) Schematic view of a reversible network based on non-covalent interactions (dotted lines) of ditopic (petrol blue) and tritopic (orange) molecules. **B**) Self-healing process of an oligomeric, thermoplastic elastomer. In case of damage, the cut surfaces need to get in contact to start self-adhesion. The new arrangement of hydrogen bonds leads to the healing of the cut polymer. **A**) and **B**) reproduced with permission from ref. 127. Copyright 2008 Nature Publishing Group.

Moreover, ureidopyrimidinone (Upy) moities, i.e., quadruple hydrogen bonding motifs, have been developed as injectable hydrogels for biomedical applications like tissue engineering, drug delivery, or 3D bioprinting, and shown shear-thinning and self-healing abilities.[133] Most conventional hydrogels are formed in situ by chemical cross-linkage and suffer from drawbacks, such as clogging. Therefore, hydrogels with a viscous flow under shear stress and recovering behavior have been studied.[134] For instance, Meijer and co-workers demonstrated an injectable hydrogel protein delivery system for cardiac recovery after injury.[135] The system operates in terms of terminally functionalized UPy poly(ethylene glycol) (PEG), showing a sol-

to-gel transition at pH < 8.5. The catheter-injected hydrogelator solution, loaded with an antifibrotic growth factor, was delivered to the injured site. The immediate contact with heart tissue led to gelation caused by the change in pH. The gel worked as a local drug release reservoir and self-repaired the injection site. Bai and co-workers demonstrated another study on self-healing and self-injectable hydrogels.[136] Here, the authors did not entirely rely on hydrogen interactions but rather on the interplay of hydrophobic (π-π-stacking, hydrophobic effect) and hydrophilic (hydrogen bonds) domains within a peptide sequence. Assembly caused by hydrophobic effects or pi-pi stacking is also a key driving force in living systems to trigger shape change or folding processes as well as the formation of micelles or membranes.[99] The entropic gain drives the collapse of hydrophobic segments away from the aqueous medium leading to an assembled structure. The authors investigated a series of Fmoc-dipeptides with differing strengths of the hydrophobic domains (Fmoc-tyrosine-leucine (Fmoc-YL-OH), vs. Fmoc-tyrosine-alanine (Fmoc-YA-OH), vs. Fmoc-leucine-leucine (Fmoc-LL-OH) vs. Fmoc-phenylalanine-leucine (Fmoc-FL-OH) and concluded that the higher the hydrophobic forces, the stronger the gel's mechanical stiffness, whereas increased hydrogen bond interactions led to a greater self-healing ability. *In vivo* studies showed that the tyrosine-leucine dipeptide Fmoc-YL-OH, displayed the highest shear-thinning and self-healing features. Molecular dynamics (MD) simulation confirmed that this may be caused by the additional hydrogen bond interactions of the phenolic hydroxyl group since more hydrogen bonds were counted. It also forms longer fibers than the other dipeptides in a 100 ns time window, indicating faster assembly kinetics. In terms of design considerations, this study stresses that a self-healing material, and a high recovery rate can be achieved by fast assembly rates and additional hydrogen bond interactions. However, hydrophobic and hydrophilic interactions must be designed in a balanced manner. The directionality of selected and designed hydrogen bonds could lead to an orientation interaction enhancing the formation of the fiber network in the case of damage.

Non-covalent host-guest interaction based on the macrocycles cyclodextrins (CDs), curcubit[n]urils, crown ethers or catenanes were reported to result in self-healing hydrogels.[137] In the case of oligosaccharide CDs, the hydrogel network can be accomplished either by physical cross-linkage through host-guest interactions of CD-grafted polymers and hydrophobic polymers, or by complex inclusion between the host CD and polymer structures. The latter was demonstrated with a redox-responsive self-healing host guest polymer by the Harada group (Figure 10).[138] Herein, 6βCD grafted pAA serves as the host-polymer, while ferrocene (Fc) modified pAA presents the guest-polymer. Upon mixture of both, immediate gelation occurred. Due to the redox responsiveness of the Fc-group, the hydrogel's sol-gel

transition could be switched, and the repair of two cut polymer blocks was initiated after applying a reducing agent on the cut surface.

Huang and co-workers studied a similar concept of self-healing supramolecular gel formation by crown ether host-guest interactions.[100] A dibenzo[24]crown-8 (DB24C8) grafted poly(methyl methacrylate) (PMMA) was cross-linked by bisammonium salts leading to a supramolecular gel. Interestingly, the gel displayed an excellent macroscopic gel recovery as rheological analysis concluded a recovery of 100% under a high strain in less than 10 seconds, feasible for several cycle times. Due to the pH-dependable sol-gel transition, the gel can be degraded. One unique example of an optically healable supramolecular polymer driven by metal-ligand coordination was given by Rowan and colleagues.[139] The polymer is based on a supramolecular polymerization by telechelic, low-molecular mass poly(ethylene-*co*-butylene) terminated with 2,6-bis(1'-methylbenzimidazolyl)pyridine (Mebip) ligands able to complex with Zn^{2+} ions. The metal-ligand interactions are prone to heat and can be reversibly disconnected. If a damaged area was exposed to UV-light, healing occurs due to a light-to-heat conversion. Upon light absorption, the electronic excitation of the metal-ligand moieties results in a heat conversion of the absorbed energy. Consequently, the metal-ligand bond is temporarily disentangled, and the viscosity decreased, enabling rapid and efficient healing.
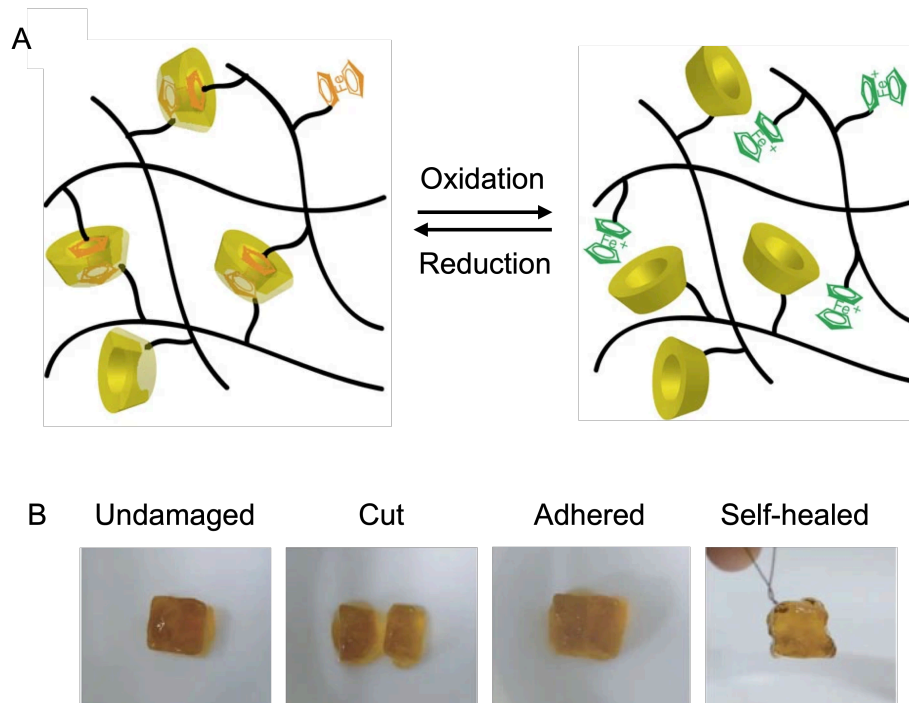

Figure 10: Self-healing based on redox-responsive sol-gel transition. **A**) Schematic illustration of sol-gel redox-switch. Under oxidative conditions, e.g., the addition of NaClO, the Fc-group (orange) gets oxidized (Fc$^+$, green). Due to the electrostatic repulsion, the guest leaves the CD-host (yellow) leading to the sol-state. Adding a reducing agent results in the gelation of the solution, the Fc-guest enters the host again. **B**) Self-healing of hydrogel pieces. The pAA-6βCD/pAA-Fc hydrogel was cut into two pieces. By rejoining the damaged sites, the gel self-

healed within 24 hours. **A**) and **B**) reproduced with permission from ref. 138. Copyright 2011 Macmillan Publisher Limited.

5.3.4 Chemically fueled self-assembly to create self-healing materials

The above-presented synthetic materials proved to show diversity and versatility in designing self-healing materials based on microencapsulation, dynamic covalent bond formation, or non-covalent interactions. However, most examples showed non-autonomous healing and were constrained to externally added healing agents or stimuli while not showing high cycle times. Inspiration from biological systems like microtubules might give the right motivation for another strategy to induce self-healing as nature does. In chapter three, I mentioned the rich diversity biology offers to exert unique properties like mechanical stability and, specifically, the ability to self-heal. Microtubules have a high stiffness, showing a great ability to bend under intracellular forces.[140] Several studies stated that this property comes from preliminary existing defects and holes in the microtubular network, which leads to the microtubules' unique mechanical features.[141-143] Théry and colleagues studied the microtubules' self-regeneration potential in response to mechanical stress, like bending, using a microfluidic device under fluorescence imaging.[61] Initially, they confirmed that the microtubules' stiffness steadily decreases with growing bending cycle number, i.e., the microtubules soften under mechanical stress. This is assumed to be promoted by the already existing lattice defects. Moreover, by giving long recovery periods in between the bending cycles, no structure softening was observed, hinting at the microtubules' ability to heal. They hypothesized that a local disassembly spreading from the pre-existing defects and long-distance disorganization of the microtubular structure might be key factors leading to the self-repair ability. Furthermore, this study indicates that self-healing can also occur by incorporating "fresh" tubulin dimers from the solution.[66] This assumption is inherently grounded in the dynamic character of chemically-fueled self-assemblies and shows that the structure's growth and collapse are orchestrated by fuel-activated building blocks.

Van Esch and colleagues reported one rare synthetic example of a chemically-fueled self-assembled material demonstrating self-healing behavior.[144] The system comprised the gelation and fiber formation of bis and tris-carboxylate reagents using the methylating agent dimethyl sulfate as chemical fuel. By tuning the fuel amount, they controlled the hydrogel's lifetime as well as mechanical properties. But more importantly, the material exerted a chemically fuel-driven self-healing ability after external mechanical damage. After all, this is not a too surprising observation since chemically fueled materials offer self-regeneration due to their dynamic nature. As long as fuel is provided to the system, building blocks will be dynamically activated and deactivated, and the structure assembles and disassembles.

Consequently, this implies that once damaged, newly activated building blocks can be incorporated into the network, and the initial function be re-stored (provided the presence of fuel). This opens the doors to design materials that can intrinsically and autonomously self-heal.

5.4 Conclusion and outlook

Nature beautifully demonstrates how living systems adapt, maintain their existence, and can self-heal autonomously in the case of damage. During the last decades, material scientists approached multiple strategies to mimic this trait. On the one hand, they achieved creating self-healing behavior extrinsically by coupling an external trigger using, for example, healing agents-filled microcapsules. Moreover, it was soon discovered that by directly targeting the bond formation process and the network's connectivity, the system could be endowed with reversible features and, thus, enhance self-repair mechanisms. This dynamism was conducted by, for instance, dynamers or vitrimers, forming dynamic reversible covalent bonds based on reversible bond exchange reactions.

On the other hand, supramolecular materials showed another strategy to induce self-healing. However, in most cases, either an external trigger like an increase in temperature to initiate the exchange reaction, or an entirely static network due to the formation of the thermodynamic most stable structure diminished the dynamic character. In contrast, biological systems, such as the cytoskeleton's microtubule network, impeccably present self-healing features based on chemically fueled assembly and disassembly processes. Indeed, it can self-restore its features by operating completely autonomously, i.e., without any extern or intrinsic stimulus triggering the healing effect. Though one rare synthetic example already demonstrated chemically fueled fibers that can self-heal, the underlying mechanism remains unclear. Indeed, we lack a fundamental understanding of the self-healing mechanisms of synthetic chemically fueled supramolecular materials.

6 A chemically fueled supramolecular glue for self-healing gels

Abstract

In this work, we investigated a chemically fueled supramolecular material that can self-heal. We used a similar approach as the synthetic chemically fueled fiber example in chapter five, relying on a small peptide that assembles into a fiber network upon the consumption of fuel. Interestingly, the rapid activation and deactivation kinetics of the reaction cycle were not reflected in the assembly and disassembly kinetics. In other words, building blocks in the solution and the fibrillar network get activated and deactivated, but the fibrillar assemblies hardly disassemble, displaying a static-like character. To our excitement, the network became dynamic if externally ruptured and consequently self-healed. We explain this behavior by the concept of a chemically fueled molecular glue. By a pseudo-continuous supply of fuel to the system, most peptide molecules get activated to self-assemble into fibers. Some peptide molecules remain in solution and undergo constant activation and deactivation, but without resulting in assembled structures due to the low concentration and lack of nucleation sites. Breakage of the fibers leads to a significant increase in nucleation sites that the molecular glue could attach to. The broken fiber ends self-assemble again, and the network is restored. We found that the higher the peptide's critical aggregation concentration (CAC), the greater the healing efficiency. This concept was applied to other peptides as well, demonstrating an important relation between the system's CAC and its healing efficiency.

This work has been published:

This section states the individual work of each author in the publication above. J. B. and M. A. W. wrote the manuscript, J. R.-F., M. A. W., B. R., A. M. B., M. K. performed the experiments, J. R.-F. and M. A. W. equally contributed to the work. J. B. and O. L. supervised the research. All authors have given approval to the final version of the manuscript.

EDGE ARTICLE

Check for updates

A chemically fueled supramolecular glue for self-healing gels†

Jennifer Rodon-Fores, ‡[a] Michaela A. Würbser, ‡[a] Martin Kretschmer, [bc] Benedikt Rieß, [a] Alexander M. Bergmann, [a] Oliver Lieleg [ID] [bc] and Job Boekhoven [ID] *[a]

Chemically fueled supramolecular materials offer unique properties that include spatial and temporal control and even the ability to self-heal. Indeed, a few studies have demonstrated the ability to self-heal, however, the underlying mechanisms remain unclear. Here, we designed a peptide that forms a fibrillar network upon chemical fueling. We were surprised that the hydrogel could self-heal despite the lack of dynamics in the fiber assembly and disassembly. We explain this behavior by a mechanism that involves the chemically fueled peptide molecules that cannot self-assemble due to the lack of nucleation sites. When the fibers are perturbed, new nucleation sites form that help the assembly resulting in the healing of the damaged network. Furthermore, we generalized the behavior for other peptides. We refer to this non-assembling, chemically-fueled peptide as a molecular glue. In future work, we aim to explore whether this self-healing mechanism applies to more complex structures, narrowing the gap between biological and synthetic self-assemblies.

Introduction

Supramolecular materials are materials in which the building blocks are held together by non-covalent interactions.[1–6] Recently, the focus has been on dynamic supramolecular materials that adapt to changes in their environment.[7–12] A class of these dynamic materials is the chemically fueled supramolecular materials in which chemical reactions regulate self-assembly.[13–19] In the chemical cycle, a precursor molecule reacts with a chemical fuel and becomes activated for self-assembly (*i.e.*, the activation reaction, Fig. 1A). That activated state is transient and spontaneously reverts to the precursor. Thus, the building blocks for the assembly have a finite lifetime set by the activation and deactivation rates. Therefore, the properties of the supramolecular material are dictated by the kinetics of activation and deactivation and the rates of assembly and disassembly. The dynamic nature of these chemically fueled supramolecular materials offers exciting properties. For example, due to their fuel-dependent nature, these materials can be controlled over space and time.[16,20] Specifically, if a finite amount of fuel is applied, a material emerges as long as fuel is

available. This lifetime control has been explored in the context of self-abolishing hydrogels, transient emulsions, temporary nanoreactors, and others.[21–32] When fuel is applied locally, the assemblies follow the gradients of fuel used in, *e.g.*, self-erasing inks.[33,34] Finally, due to the constant activation and deactivation of self-assembling building blocks, the emerging supramolecular materials have been proposed to be self-healing.[35] Indeed, biological chemically fueled assemblies, like the GTP-fueled microtubules, have been demonstrated to self-heal,[36,37] and the underlying mechanisms are relatively well understood. In contrast, up to now, only one study indicates that chemically fueled synthetic fibers can self-heal.[38] However, we still lack a fundamental understanding of the underlying self-healing mechanisms. Moreover, we do not know whether these principles are generalizable among chemically fueled assemblies.

In this work, we study how chemically fueled hydrogels can self-heal. We describe a small peptide that assembles into a fibrillar network at the expense of chemical fuel. Despite the fast dynamics of the reaction cycle, the fiber network is not dynamic in its assembly and disassembly. That means that building blocks are deactivated and reactivated in the fiber network without disassembling. Excitingly, after external damage, the network becomes dynamic, heals, and reinstates its static nature. Thus, chemical fuel is constantly burnt without any dynamic assembly. However, the mechanism of constantly burning fuel allows for healing in the case of damage.

Results and discussion

The peptide we used in this study is based on the peptide Fmoc-AAD-OH in which Fmoc means fluorenylmethoxycarbonyl, A

[a]Department of Chemistry, Technical University of Munich, Lichtenbergstraße 4, 85748 Garching, Germany. E-mail: job.boekhoven@tum.de

[b]TUM School of Engineering and Design, Department for Materials Engineering, Technical University of Munich, Boltzmannstr. 15, 85748, Garching, Germany

[c]Center for Protein Assemblies (CPA) & Munich Institute of Biomedical Engineering (MIBE), Technical University of Munich, Ernst-Otto-Fischer-Str. 8, 85748 Garching, Germany

† Electronic supplementary information (ESI) available. See https://doi.org/10.1039/d2sc03691f

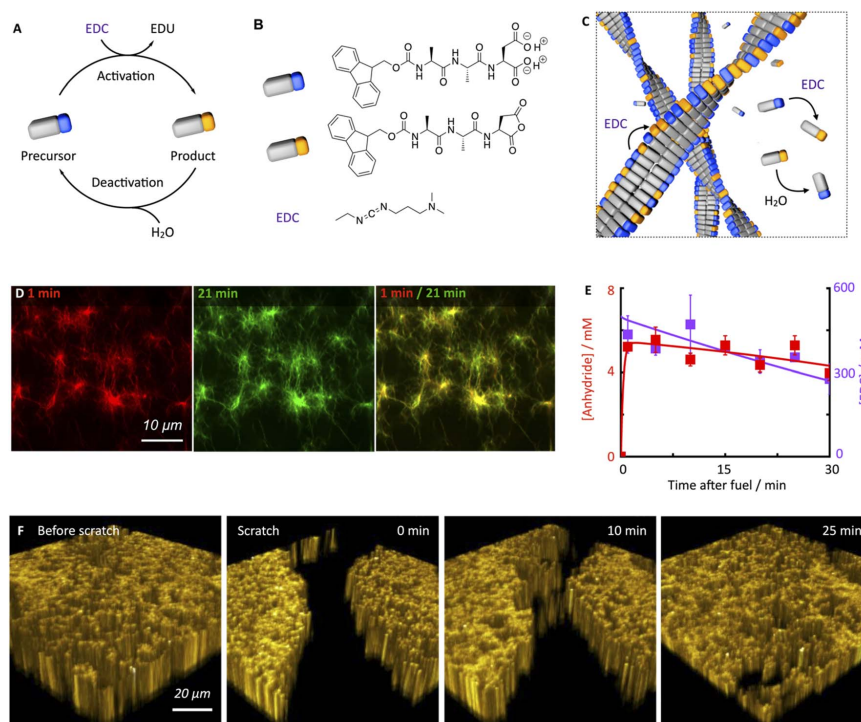‡ J. R.-F. and M. A. W. contributed equally.

Fig. 1 Chemically fueled self-assembly of Fmoc-AAD-OH into fibrillar assemblies in a pseudo-steady-state. (A and B) The chemical reaction cycle and peptide design. (C) Scheme of the fibers in pseudo-steady-state. Activation and deactivation occur at roughly equal rates both on the fibers and in the solution. Hardly any precursor disassembly takes place. (D) Confocal images of 10 mM Fmoc-AAD-OH fueled with 500 mM EDC, 1 minute and 21 minutes after application of fuel. The composite shows the lack of dynamic behavior. (E) Anhydride (red) and EDC (violet) concentration against time when 10 mM Fmoc-AAD-OH was fueled with 500 mM EDC. Markers represent HPLC data performed in triplicate; solid lines represent theoretical data, calculated using the kinetic model. (F) Confocal fluorescence microscopy in $x/y/z$ dimension of 10 mM Fmoc-AAD-OH fueled with 500 mM EDC before performing a scratch and after the scratch performed 13 minutes after fuel addition, showing self-healing of the network over the course of 25 minutes.

means Alanine, and D means aspartic acid (Fig. 1B). The peptide serves as a precursor in our chemical reaction cycle. In the cycle, we used *N*-(3-dimethylaminopropyl)-*N'*-ethyl-carbodiimide (EDC) as fuel as previously published (Fig. 1B).[39,40] In the activation reaction, the precursor reacts with EDC and is converted into its corresponding cyclic anhydride, *i.e.*, the product (Fig. 1B). In the aqueous environment, the precursor rapidly hydrolyzes back to the precursor state, *i.e.*, the deactivation reaction. Taken together, upon application of fuel, a transient product emerges that is sustained until all fuel is depleted. Due to the loss of the two anionic carboxylates upon activation, the product can self-assemble into fibers driven by the Fmoc-group induced π-stacking and hydrogen-bond formation (Fig. 1C). Indeed, the peptide precursor was dissolved at a 10 mM concentration in an aqueous 200 mM MES buffer at pH 6, and no evidence of self-assembly was observed (see ESI, Fig. 1†). After applying 500 mM EDC, confocal

microscopy revealed that a dense fibrillar network had formed (Fig. 1D and ESI, Fig. 2†).

We applied a significant excess of chemical fuel to ensure that the fibrillar network remained in a pseudo-steady-state, *i.e.*, that the activation and deactivation reaction rates were roughly equal (Fig. 1E). A pseudo-steady-state ensures that the network is not growing or collapsing during the analysis, which would not allow for an analysis of the self-healing behavior. By high-performance liquid chromatography (HPLC), we measured whether the 500 mM fuel was sufficient to keep the precursor and product in a pseudo-steady-state (Fig. 1E). Thus, at selected time intervals, we quenched a sample using a previously published method.[41] We found that the product concentration was roughly 5.8 mM and remained relatively constant for the first 30 minutes. In this time frame, we also observed a high EDC consumption. Thus, the product remained in a pseudo-steady state due to the sufficiently high excess of fuel. We used

a kinetic model that we previously wrote to predict the pseudo-steady-state kinetics and the consumption of fuel (Fig. 1E, ESI† supporting notes for a description of the model). The kinetic model predicts the concentrations of all species involved in the reaction cycle for each second by using five differential equations. From the kinetic model, we could calculate a half-life of the product of 46 seconds.

Despite the short half-life of the product, we were surprised to find that the fiber network is not dynamic in the sense that it does not assemble or disassemble (Fig. 1D). We can visualize the lack of dynamics by overlaying two micrographs of a 20 minute interval. When the two micrographs are overlaid, it is apparent that hardly any fibers have been newly formed or old ones disassembled. In other words, even though the product only has a half-life of 46 seconds, fiber disassembly hardly occurs.

We hypothesize that either the product assembles and does not deactivate after assembly resulting in a static network, or, the product is deactivated in the fiber, which also results in a static fiber network. In line with previous work on similar peptides,[40,42] a ^{1}H-NMR-study showed that most of the peptides, be it in the precursor or product state, reside in the assembled state (*vide infra*). Thus, the precursor remains kinetically trapped within the fibers after deactivation and is reactivated before it can disassemble (Fig. 1C). Taken together, our hydrogel can persist for roughly an hour in a pseudo-steady state but, surprisingly, does not display any dynamics of assembly or disassembly.

Next, we investigated the ability of this fiber network to self-heal by confocal fluorescence microscopy. Inspired by a cell wound healing assay which is based on manually drawing a scratch with a pipette tip through a line of epidermal cells,[43,44] we developed a micromanipulator that can draw a scratch through our hydrogel with the tip of a needle (see Methods and ESI, Fig. 3†). In the assay, a hydrogel is made in an incubator chamber with a microscopy glass bottom window such that the hydrogel can be imaged by confocal microscopy. The micromanipulator drags a needle over the microscopy glass, such that it draws a trench through the gel in which the gel is damaged. Importantly, the hydrogel and the trench of damaged hydrogel remain hydrated such that no drying effects play a role in the healing process. The micromanipulator combined with an Arduino microcomputer allowed for automation and more reproducible scratching than manual perturbation. Specifically, we guaranteed an average scratch size of 54.9 μm (±12.4 μm). We used our micromanipulator on a fiber network in pseudo-steady-state (10 mM Fmoc-AAD-OH with 500 mM EDC) and drew a scratch 13 minutes after the fuel was added. Immediately after the scratch, we imaged the fiber network in three dimensions as a function of time (Fig. 1F). We were excited to observe that the scratch was, in fact, healing and that there was no evidence of the damage after roughly 30 minutes.

To quantify the healing, we repeated these experiments (Fig. 2A) and determined the width of the scratch (W, see Methods) in Fiji as a function of time after the scratch (Fig. 2B and see Methods). We found that W decreased gradually over 25

minutes until it reached zero, *i.e.*, until the scratch was no longer visible (Fig. 2B). From this data, we concluded that the scratch heals to 100% over 25 minutes when a scratch is drawn 5 minutes after fuel addition. On another sample, we drew a scratch 30 minutes after adding fuel and found that the healing was much slower and incomplete. To compare the datasets, we calculated the degree of healing by measuring the amount healed ($W_{t=0} - W$) and normalized it towards the size of the initial width ($W_{t=0}$) following eqn (1) (see Methods). Normalizing the size of the initial width allowed us to average multiple scratches (Fig. 2C). It should be noted that the fluorescence intensity in the micrographs decreased somewhat over the process of the healing (*e.g.*, Fig. 2A), which could be related to a morphological transition of the network after damaging it.

To confirm that the self-healing was an active behavior, we performed similar experiments with Fmoc-AAD-OH, which was acidified, *i.e.*, a fiber network that was not maintained by a chemical reaction cycle but instead close to equilibrium. After the scratch, these fiber networks remained static without evidence of self-healing (see ESI, Fig. 4†). This data shows that chemically fueled fiber networks can heal and that the time of damage in the cycle plays a significant role in the ability of the network to heal.

To further understand the lack of healing, we also measured the average healing rate over 25 minutes after the scratch, *i.e.*, the migration rate of the fiber front (Fig. 2D, see Methods eqn (2)). Again, we found that the healing was fast early in the cycle, but samples that were perturbed later in the cycle suffered from a slow healing process. The lack of healing later in the cycle is surprising, given that the reaction cycle is in a pseudo-steady state, *i.e.*, the concentration of product and fuel did not drastically decrease in this time window. We hypothesized that the accumulation of the EDU waste caused the slowing of the healing.[45] Thus, we measured the migration rate 13 minutes after adding fuel to the fibrillar networks with additional EDU (Fig. 2E). We found a peculiar relation between the migration rate and the EDU amount present in the system by adding different EDU concentrations before the fuel addition (Fig. 2E). With a concentration of 80 mM EDU or greater, no healing was observed. From these observations, we concluded that the active fiber networks are self-healing but accumulated waste severely hinders it.

Furthermore, we confirmed the ability of the fiber networks to self-heal on a macroscopic level. A vial inversion method visualized the ability of the hydrogel to recover and become self-supporting after damaging it on a vortex mixer for 20 seconds (Fig. 2F). Plate–plate rheology showed that after fueling with 500 mM of EDC, a hydrogel with a 1.4 kPa strength is formed that slowly loses stiffness as a function of time (Fig. 2G). After the vortex mixing, the damaged (liquified) gel converted back into a self-supporting hydrogel over the course of five minutes. In line with the previous data, we found that the gel could not recover when the damage was inflicted late, *i.e.*, after 30 minutes after adding fuel (ESI, Fig. 5†).

To quantify the recovery of the storage modulus, we performed the same vortexing experiment but analyzed the damaged gel with the rheometer. In line with the vial inversion
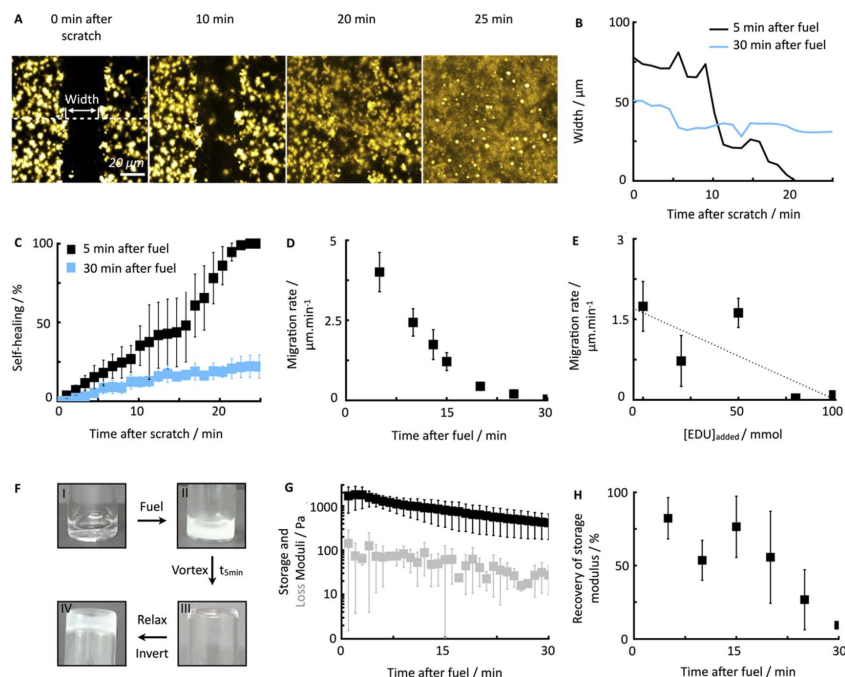
Chemical Science

Fig. 2 Self-healing behavior of chemically fueled Fmoc-AAD-OH in a pseudo-steady-state. (A) Confocal micrographs of damaged Fmoc-AAD-OH fibers at 5 minutes with collapsing width over the time of 25 minutes. For each scratch, a triplicate of widths was analyzed over the whole scratch size (each width being in a distance of roughly 40 μm from each other). (B) The width of a scratch as a function of time after damaging at 5 minutes (black) and 30 minutes (light blue). (C) Normalized self-healing behavior as a function of time after damaging at 5 minutes (black) and 30 minutes (light blue). Error bars represent 3 widths per scratch for an average of 3 scratches. (D) Migration rate of fiber assemblies over time of damage after fuel addition. Error bars represent 3 widths per scratch for an average of 3 scratches. (E) Migration rate over added EDU concentration, damaging at 13 minutes after fuel addition. Error bars represent 3 widths per scratch for an average of 3 scratches. (F) Vial inversion pictures of 10 mM Fmoc-AAD-OH without fuel (I), after the addition of 500 mM fuel (II), after vortex mixing 5 minutes after fuel addition (III), relaxing for 5 minutes and inverting (IV). (G) Storage and loss modulus over time of 10 mM Fmoc-AAD-OH fueled with 500 mM EDC. Error bars represent the average of 3 experiments. (H) Recovery of storage modulus of Fmoc-AAD-OH over different damage time after fuel addition. Error bars represent the average of 3 experiments.

tests, we found that recovery depended on the cycle time (Fig. 2H). Specifically, after 5 minutes in the reaction cycle, the gel without perturbation had a storage modulus of 1.4 kPa. A gel damaged on the vortex mixer after 5 minutes in the cycle had a strength of 0.7 kPa and recovered to 1.2 kPa over the course of 5 minutes (ESI, Fig. 6†). Thus, the gel was able to recover 82% of the original storage modulus. In line with the microscopy data, a gel damaged after 30 minutes in the cycle could only recover 9.4% of its initial storage modulus. So indeed, our chemically fueled Fmoc-AAD-OH assemblies show self-healing characteristics on a microscopic and macroscopic level, despite being limited due to the eventually accumulating EDU concentration.

We hypothesize that this self-healing behavior of the network, despite the lack of self-assembly and disassembly dynamics in the networks, originates from two effects (Fig. 3A). On the one hand, peptides are kinetically trapped in the fibers and activation, deactivation and reactivation take place on the

fibers without disassembly. That would explain the lack of dynamics. On the other hand, part of the peptides is activated and deactivated in solution but cannot assemble because of a lack of endcaps of fiber to adhere to. After damaging the gel, the number of endcaps increases, and the healing process starts.

To confirm this hypothesis, we tested how much of the peptide is trapped in the fibers and how much of the peptide remains in the solution. We also tested how many endcaps become available during the damaging process. By ^{1}H-NMR, we quantified that roughly 0.7 mM of the peptide remained in the solution in the first minutes. We assume that non-assembled peptides are NMR-active and visible whereas the assembled ones are not (ESI, Fig. 7A†). In other words, most peptide is assembled in the fibers. Combined with the HPLC data, which showed that there was roughly 5 mM precursor available under these conditions, this implies that most of the precursor is in
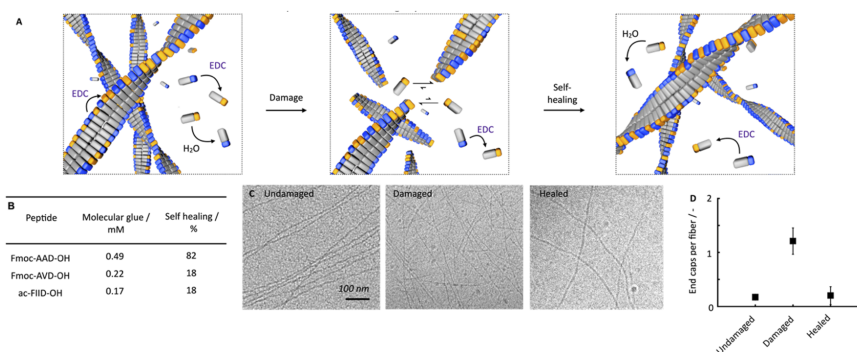
Edge Article

Chemical Science

Fig. 3 Self-healing mechanism of chemically fueled Fmoc-AAD-OH in a pseudo-steady-state. (A) Schematic depiction of the proposed self-healing mechanism. (B) Critical aggregation concentration of molecular glue and self-healing (rheological) at $t = 5$ minutes of Fmoc-AAD-OH, Fmoc-AVD-OH, and ac-FIID-OH. (C) Cryo-TEM micrographs of 10 mM Fmoc-AAD-OH fueled with 10 mM EDC without ultrasonication at $t = 1$ minute after fuel addition (undamaged), ultrasonication at $t = 1$ minute after fuel addition (damaged), 25 min after ultrasonication at 1 minute after fuel addition (healed). (D) Ratio of the number of end caps over the number of fibers per 1 μm^2 at $t = 1$ minute after fuel addition without damaging (undamaged), damaging at $t = 1$ minute after fuel addition (damaged), 25 min after damaging at $t = 1$ min after fuel addition (healed). All experiments were performed in triplicate.

the fibers. Thereby, we confirmed that the fibers consist of a co-assembly of anhydride product and precursor. Thus, there is a population of peptides that remains kinetically trapped in the fibers (roughly 9.3 mM), and there is a population of peptides in the solution that is continuously activated and deactivated (roughly 0.7 mM). We assume that the anhydride in the solution cannot assemble with the fibers because, on the one hand, its concentration is too low to nucleate into new fibers. On the other hand, the density of the endcaps is too low to add on existing fibers. In other words, the reaction cycle continuously converts chemical energy, but no new molecules assemble or disassemble. When a lower amount of fuel was added (100 mM, ESI, Fig. 7B†), similar kinetic trapping of the precursor in the fibers was observed. Even after all 100 mM fuel was depleted, disassembly had not completely taken place.

We established that peptides remain kinetically trapped. Next, we wondered how much of the peptide remains in solution. Thus, we determined the critical aggregation concentration of Fmoc-AAD-OH with 500 mM EDC. We added increasing amounts of Fmoc-AAD-OH to a solution of 500 mM EDC and measured the scattering rate by DLS (ESI, Fig. 8†). The amount of Fmoc-AAD-OH needed to find the first evidence of assemblies was 0.7 mM. We then used the kinetic model to calculate the amount of anhydride in that experiment to be around 0.5 mM. Thus, we conclude that the anhydride's critical aggregation concentration (CAC) of Fmoc-AAD-OH is ∼0.5 mM (Fig. 3B). From this surprisingly high number, we assume that, in our gels, most anhydride resides in the fibers. In contrast, roughly 0.5 mM anhydride is in the solution phase but cannot assemble due to its low concentration and the low number of endcaps. We refer to the anhydride in solution as the "molecular glue". The scenario changes when the gel is destroyed (Fig. 3A, center). We expect that the number of endcaps drastically increases due to

the damage. These endcaps are now available for the molecular glue to grow new fibers and aid healing.

We further supported the molecular glue hypothesis by cryo-TEM and counted the endcaps per fiber in 1 μm^2 (Fig. 3C). The high gel stiffness made obtaining images challenging by cryo-TEM, so we changed the conditions to 10 mM Fmoc-AAD-OH fueled with 10 mM EDC. We normalized the number of end caps by the total number of fibers and found that the number of endcaps increased roughly 6-fold after ultrasonication. Moreover, after 25 minutes, the endcaps had drastically decreased again, further corroborating the self-healing through growing on endcaps (Fig. 3D). The observation that mild ruptures increase the chain termini and affect the seeded fiber growth has been demonstrated by others too.[46,47]

To further confirm the molecular glue hypothesis, we prepared a similar peptide that is fluorescently labeled with an NBD label on an additional cysteine (Fmoc-AAC(NBD)D-OH). We added the NBD label because of its sensitivity to its surrounding environment, thus allowing us to measure whether it is co-assembled or in solution. We prepared a gel of 10 mM Fmoc-AAD-OH fueled with 500 mM EDC and added a mixture of Fmoc-AAD-OH and Fmoc-AAC(NBD)D-OH on top in a ratio of 10 : 1 (ESI, Fig. 9†). We found that the fluorescence signal did not increase compared to a blank experiment of Fmoc-AAC(NBD)D-OH with fuel which points to no dye incorporation into the network. In contrast, when the dye was present from the beginning of the cycle, the fluorescence was very high, demonstrating that our NBD peptide indeed was incorporated. Finally, when adding the Fmoc-AAC(NBD)D-OH just after damage by vortexing or ultrasonication, the fluorescence signal increased drastically.

We received similar results on a microscopic level. By confocal fluorescence microscopy with the fluorescently tagged

peptide and Nile Red, we imaged three samples, *i.e.*, an undamaged sample subjected to the fluorescently tagged peptide, a sample to which we added the fluorescently tagged peptide and then sonicated it, and a sample damaged with a needle loaded with fluorescently tagged peptide. Without damage, there was no evidence of any fluorescence intensity of the NBD-labeled peptide, demonstrating no incorporation (ESI, Fig. 10A†). In contrast, we observed homogeneous incorporation of the labeled peptide if the Fmoc-AAC(NBD)D-OH mixture was added on top of a gel and damaged by ultrasonication (ESI, Fig. 10B†). Lastly, we performed a scratch on a Fmoc-AAD-OH gel 13 minutes after fuel addition, applying a needle loaded with 1 μL of a Fmoc-AAD-OH/Fmoc-AAC(NBD)D-OH solution (ESI, Fig. 10C†). By this, we envisioned to provide the labeled peptide directly at the damaged front to track the spatial re-organization of the fibers. Over the migration time of 25 minutes, we observed a substantial increase in the intensity of the labeled peptide, specifically at the scratched site. These experiments further support our hypothesis that new building blocks are incorporated into the network only after damage as molecular glue aids the healing process.

To understand better the mechanism of self-healing, we tested two more chemically fueled, fiber-forming peptides, *i.e.*, Fmoc-AVD-OH and ac-FIID-OH.[40,48] We chose Fmoc-AVD-OH due to its chemically structural similarity. Due to the more hydrophobic valine amino acid compared to alanine, it has a lower critical aggregation concentration, and we calculated the concentration of molecular glue to be also lower at 0.22 mM (Fig. 3B and ESI, Fig. 11†). On the other hand, ac-FIID-OH is structurally more different than Fmoc-AAD-OH. Yet, it also forms a hydrogel in response to chemical fuel and has a similar critical aggregation concentration. Its concentration of molecular glue is low at 0.17 mM (ESI, Fig. 11†). Cryo-TEM of these peptides demonstrated that they indeed form fibers (ESI, Fig. 12†).

By quantifying the recovery of storage modulus on the rheometer, we found that the self-healing ability of the other two fiber formers was lower than Fmoc-AAD-OH (ESI, Fig. 13†). Specifically, Fmoc-AVD-OH and ac-FIID-OH only showed a recovery of storage modulus of roughly 18%, 5 minutes after the application of fuel. These findings further highlight the importance of molecular glue for the healing of the hydrogels, *i.e.*, if the product has poor solubility, not much molecular glue is available, and healing is poor.

Conclusions

We found that chemically fueled fibers can self-heal even though they are not dynamic. We explain this surprising finding by the concept of a chemically fueled molecular glue. Briefly, most peptides are assembled and will not disassemble upon deactivation, which explains the lack of dynamics. Some peptide remains in solution and is continuously activated and deactivated but cannot assemble into fibers due to their low concentration and the lack of nucleation sites to adhere to. The damaging of the network creates numerous new nucleation sites on which this molecular glue can self-assemble. The

peptide's critical aggregation concentration is related to the concentration of molecular glue. Thus, the higher the critical aggregation concentration, the greater the ability to self-heal. It should be noted that the term molecular glue refers to a glue that can only heal its fibrillar network. Furthermore, we found that the behavior was generalizable for other peptides and confirmed that the system's CAC indeed notably influenced the self-healing nature. In future work, we aim to expand our understanding further and adapt the mechanism to more complex peptide structures.

Materials and methods

Materials

We purchased benzylamine (BA, 99%), deuterated dimethyl oxide (DMSO-D_6, 100%, 99.96 atom % D), deuterium oxide (D$_2$O, 99.96 atom % D), 1-ethyl-3(3-dimethylaminopropyl) carbodiimide hydrochloride (EDC·HCl, 99%), *N,N*′-diisopropyl-carbodiimide (DIC, 99%), 37 wt%. hydrochloric acid (HCl, MQ 200), 2-(*N*-morpho-lino)ethane sulfonic acid (MES, 99.5%), Nile Red (MQ 100), piperidine (99%), Fmoc-D(O*t*Bu)-wang resin (100–200 Mesh size, loading 0.67 mmol g^{-1}), protected amino acids (Fmoc-A-OH (95%), Fmoc-V-OH (>98%), Ac-F-OH (98%), Fmoc-I-OH (98%)), sodium hydroxide (NaOH, >98%), *N,N*-dimethylformamide (DMF, 99.8%), diethyl ether (Et$_2$O, >99%) trifluoroacetic acid (TFA, 99%), triisopropylsilane (TIPS, 99%), *N*-ethyldiisopropylamine (99%, DIEA), 4-chloro-7-nitrobenzo-furazan (NBD-Cl, 98%), β-mercaptoethanol (>99%) and 4-methyl-morpholine (NMM, 99%) from Sigma-Aldrich. Hydroquinone (99%) was purchased from Thermo Fisher Scientific and oxyma (97%) from Novabiochem. High-performance liquid chromatography (HPLC) grade acetonitrile (ACN) was purchased from VWR. All chemicals were used without any further purification unless stated differently.

Synthesis of peptide precursor acids

Peptide precursor acids were prepared on a 0.250 mmol scale using a CEM Liberty microwave-assisted peptide-synthesizer and the Liberty Blue Application Software (Copyright CEM Corporation 2015, Version: 1.45.5794.20265). We used the pre-loaded wang resin with Fmoc-D(O*t*Bu)-OH as the first coupling step. The resin is pre-swollen outside the synthesizer for 15 min. Ahead of the amino acid coupling, the *N*-terminal Fmoc-protecting group was removed by adding a 20% v/v solution of piperidine (2 × 20 mL) in DMF. After heating in the microwave (1 minute, 90 °C), the mixture was washed with DMF (2 × 10 mL). Next, the coupling step was performed using 4.0 eq. of Fmoc-A-OH, Fmoc-V-OH, Fmoc-F-OH or Fmoc-I-OH in DMF (200 mM, 10 mL), 4 eq. of DIC (500 mM, 4 mL) and 4 eq. of oxyma (1000 mM, 2 mL). The mixture was subsequently heated in the microwave (2 minutes, 90 °C). The Fmoc-deprotection, washing, and the washing cycle was performed for each amino acid coupling. The peptide was cleaved from the resin by adding a mixture of 95% TFA (9.5 mL), 2.5% deionized water (0.25 mL) and 2.5% TIPS (0.25 mL). Afterwards, the solvent was removed under reduced pressure. The peptides were then

precipitated out using diethyl ether. The crude product was isolated by centrifugation. The resulting peptides were dissolved in ±50% MeCN in H_2O and purified by high-reversed-liquid-chromatography (RP-HPLC) (40% to 98% gradient, 0.1% TFA in H_2O and MeCN). The collected fractions were freeze-dried and stored at −20 °C.

Fluorescent labelled peptide synthesis (Fmoc-AAC(NBD)D-OH): The anchoring of the first amino acid Fmoc-D(OtBu) to the hydroxylic group of a wang resin was performed by the activated symmetric anhydride route. A solution (0.2 M) was prepared by dissolution of Fmoc-D(OtBu)-OH (12.0 mmol) and DIC (6.0 mmol) in DMF at room temperature. The DIU side product was precipitated by cooling down the reaction mixture at −20 °C for 60 min and filtered out before being brought to contact with the resin. All subsequent couplings steps were performed with the microwave-assisted peptide synthesizer. As a first step, the symmetric anhydride solution was added to the pre-swollen wang resin (0.5 mmol) together with DMAP in catalytic amounts to drive the acetylation reaction. Afterwards, the N-terminal Fmoc protecting group was cleaved with piperidine solution at 20% v/v in DMF (2 × 20 mL) and Fmoc-C(Mmt)-OH and Fmoc-A-OH were added in the same way as described before.

The orthogonal deprotection of Mmt protecting group was performed by using a low percentage of TFA (2%) with TIPS in DCM (7 × 10 mL) stirred for 10 min. The deprotection progress could be followed by the yellow trityl cations formation. At the last wash step, the solution is then colourless. To prevent the formation of disulphide bond, β-mercaptoethanol with NMM were added to the solution as oxidizing agent. Then, the NBD-Cl was coupled to the cysteine. NBD-Cl (2.0 eq., 1.0 mmol) was added and followed by DIEA (1.0 eq. 0.5 mmol). The reaction is stirred at room temperature for 2 h in aluminium foil to prevent photobleaching of the dye. The cleavage of the peptide from the resin and its purification followed the same protocol as described earlier.

Sample preparation

We dissolved the peptide precursor acids in 200 mM MES buffer resulting in a 13.3 mM stock solution, and adjusted the pH to pH 6.0. A 2000 mM EDC stock solution was always freshly prepared in MQ water, and the reaction cycle was started by adding EDC to the peptide precursor acid solution. A 1000 mM benzylamine stock solution in acetonitrile was prepared freshly ahead of the quenching experiment. All experiments were performed at 25 (±0.5) °C and stored at 8 and −20 °C.

Quantification of the anhydride concentration

We prepared 75 µL of a 13.3 mM stock solution of the precursor acid into a screw cap HPLC vial with a micro insert and added the appropriate amount of fuel by adding 25 µL of a 2000 mM EDC stock in MQ water. The reaction cycle is then quenched at the respective time points with 100 µL of a 1000 mM BA stock solution in acetonitrile following a previously reported protocol.[41] The BA reacts irreversibly with the anhydride groups and inhibits the reaction with the remaining EDC. The formed

BA-peptide derivative was trackable by HPLC (220 nm) (ESI, Fig. 14–17†). This derivative concentration is equal to the formed anhydride concentration.

Quantification of migration rate

We quantified the migration rate using a classical method for wound healing scratch assays.[43,44] Herein, we damaged our fiber network using a 200 µm thin needle that was attached to a manipulator set-up (ESI, Fig. 3†). The scratch was performed on a 10 µL volumed hydrogel (10 mM Fmoc-AAD-OH fueled with 500 mM EDC, stained with 2.5 µM Nile Red), preformed in an incubation chamber (ibidi) suitable for imaging by confocal fluorescence spectroscopy without drying effects. The scratch was performed at the respective time by inserting the needle in 45° to the hydrogel layer and subsequently instructing the manipulator to perform the scratch. The healing process was immediately monitored in x/y/z dimension (184 µm × 184 µm with a z-stack of around 20 µm) over the migration time of 25 min. The analysis of the migration rate took place around 15 µm above the glass slide surface. Each scratch was performed in triplicate. We analyzed the scratch width collapse based on the manual distance measured by the software ImageJ. Herein, we took a width of the fibers front orthogonal to the scratch and compared the initial width at $t = 0$ minute to the one at $t = 25$ minutes. For each scratch, a triplicate of widths was analyzed over the whole scratch size (each width being in a distance of roughly 40 µm from each other). The healing in % was determined as follows:

$$\text{Healing }(\%) = \left(1 - \frac{W_t}{W_{t=0}} \right) \times 100 \qquad (1)$$

The migration rate was determined by applying eqn (2):

$$r_{\text{m}} = \frac{W_{t=0} - W_{t=25}}{t_{\text{migrat.}}} \qquad (2)$$

where r_{m} is the migration rate, W the width at different times t and t_{migrat} the time over which the network migration was studied (25 minutes).

Quantification of peptide precursor in solution and co-assembly ratio

The amount of peptide precursor in solution and the co-assembly ratio of peptide precursor to anhydride product was investigated over time using ^{1}H-Nuclear Resonance Spectroscopy (NMR) and analytical High-Performance Liquid Chromatography (HPLC). ^{1}H-NMR spectroscopy was used to determine the free peptide precursor concentration in solution and the ratio of co-assembly of peptide precursor and product. We used an inner tube filled with an internal hydroquinone standard (50 mM dissolved in D_2O) and recorded the spectra according to water suppression. Herein, we compared the integral of the Fmoc-protons at 7.20–7.50 ppm to the integral of the hydroquinone standard at 6.70 ppm to determine the free peptide precursor concentration in the solution. We confirmed the co-assembly ratio by assuming that self-assembled molecules do

- 69 -

A chemically fueled supramolecular glue for self-healing gels

not show NMR-activity and remain silent, in contrast to non-assembled ones that are visible.[40]

In combination with the anhydride concentration that we obtained by HPLC, the peptide concentration in solution and the peptide precursor concentration was received as follows:

$$[\text{peptide}]_{\text{sol.}} = [\text{peptide precursor}]_{t=0.} - [\text{peptide}]_{\text{ass.}} \quad (3)$$

The amount of peptide precursor co-assembling in the fiber network was obtained according to:

$$[\text{peptide precursor}]_{\text{ass.}} = [\text{peptide}]_{\text{ass.}} - [\text{product}] \quad (4)$$

where $[\text{peptide}]_{\text{sol.}}$ represents the concentration of peptide in solution, $[\text{peptide precursor}]_{t=0}$ the initial peptide precursor concentration, $[\text{peptide}]_{\text{ass.}}$ the concentration of peptide in the fiber assemblies, $[\text{peptide precursor}]_{\text{ass.}}$ the peptide precursor concentration in the fiber assemblies and $[\text{product}]$ the concentration of anhydride product analyzed by HPLC. Using the so obtained peptide concentration in solution and our kinetic model, we could define the amount of anhydride product in solution that we define as molecular glue concentration.

Spatial organization of Fmoc-AAC(NBD)D-OH

By confocal microscopy, we analyzed the spatial incorporation of the NBD-labeled peptide at the damaged network front. As a negative control (undamaged), we prepared 10 mM Fmoc-AAD-OH with 500 mM EDC (stained with 0.1 µM Nile Red) in the incubation chamber topped with 1 µL of a mixture (10 : 1 ratio) of Fmoc-AAD-OH and Fmoc-AAC(NBD)D-OH. We used an excitation at 488 nm for the NBD-labeled peptide and 552 nm for the Nile Red stained one. The gel was screened in x/y/z-dimension for 40 minutes.

Next, the damaged experiment was approached by preparing another Fmoc-AAD-OH gel in a vial topped with 1 µL of a mixture (10 : 1 ratio) of Fmoc-AAD-OH and Fmoc-AAC(NBD)D-OH. After 13 minutes the gel was ultrasonicated for 2 minutes, immediately transferred to the incubation chamber and screened as stated above.

Finally, the Fmoc-AAD-OH gel was prepared in the incubation chamber and scratched 13 minutes after fuel addition. The applied needle was topped with 1 µL of a mixture (10 : 1 ratio) of Fmoc-AAD-OH and Fmoc-AAC(NBD)D-OH, creating the direct contact of fiber damage sites and the NBD tagged peptide. All experiments were performed in triplicate.

Quantification of amounts of end caps per fiber

The change in the number of end caps per fiber upon damage of the fiber network was determined using cryo-Transmission Electron Microscopy (cryo-TEM). Due to the gel's strength, we decreased the fuel concentration to 10 mM by adding 25 µL of a 40 mM EDC stock solution to a 75 µL peptide precursor acid stock solution of 13.3 mM in a 2 mL vial. The damaged sample was destroyed by ultrasonication of the sample for 20 seconds at $t = 1$ minute and immediately pipetted onto the prepared grid in the Vitrobot. The same sample was then pipetted on a second

grid after 25 minutes to compare for the recovery of destroyed fibers. As a control, an undamaged sample with the same conditions was prepared for the same timepoints without ultrasonicating it. Per condition, six micrographs were used to determine the average end cap per fiber ratio. All experiments were performed in triplicate.

High-performance liquid chromatography (HPLC)

We monitored the kinetics of the reaction cycle by analytical HPLC (Thermo Fisher Vanquish Duo UHPLC) with a Hypersil Gold 100 × 2.1 mm C18 column (3 µm pore size). We prepared 200 µL of the reaction mixture into a screw cap HPLC vial with micro inset following the sample preparation protocol described above. All samples were directly injected without any further dilution from the HPLC vial. We injected 2 µL for the detection of EDC, BA and for the detection of the peptide precursor acids. We used a UV/Vis detector at 220 nm and 254 nm for the quantification of all reagents. Calibration curves for the EDC (in MQ water), BA (in acetonitrile), peptide precursor acids (in MES buffer) were performed with the corresponding method in triplicate. Retention times and calibration values are given in ESI, Table 1.† We used the following method for the separation of the compounds:

HPLC method: H_2O : ACN from 98 : 2 to 2 : 98 in 12 minutes, 2 : 98 for 1 minute, 2 : 98 to 98 : 2 in 1 minute and 98 : 2 for 1 minute resulting in a 15 minute long method.

HPLC: R_t (Fmoc-AAD-OH) = 9.7 min (see ESI, Fig. 15†).
HPLC: R_t (Fmoc-AVD-OH) = 11.1 min (see ESI, Fig. 16†).
HPLC: R_t (ac-FIID-OH) = 8.9 min (see ESI, Fig. 17†).
HPLC: R_t (Fmoc-AAC(NBD)D-OH) = 11.7 min (see ESI, Fig. 18†).

Reversed-phase high-performance liquid chromatography (RP-HPLC)

The peptide precursor acids were purified on reversed-phase HPLC (Thermo Fisher, Hypersil Gold 250 × 20 mm, 5 µm pore size, C18 column) with a linear gradient of acetonitrile (ACN, 40 to 98%) and water with 0.1% trifluoroacetic acid. UV-Vis detection was conducted using 220 and 254 nm.

Kinetic model

We used a Matlab kinetic model for the calculation of the concentrations of reactants. See ESI† supporting notes for a detailed discussion.

Time-lapse photography and vial inversion

The vial inversion experiment was performed in a 2 mL HPLC vial and imaged with a high-definition camera. Time-lapse software was programmed to image the sample in a 30 second interval. We started the hydrogel formation by adding 125 µL of a 2000 mM EDC stock solution to 375 µL of 13.3 mM peptide precursor acid solution (pH 6, 200 mM MES). At the respective time, the hydrogel was destroyed using a vortex mixer for 20 seconds resulting in the liquification of the gel. After giving the gel time to relax for 5 minutes, the vial was inverted and imaged

to demonstrate the gel's ability to self-heal. All experiments were performed in triplicate.

Self-healing measure by rheology

We obtained the initial gelation morphology by adding 50 μL of a 2000 mM EDC stock solution to a 150 μL of a 13.3 mM peptide precursor acid in the rheometer. To ensure linear material response during the gelation process of the samples, the measurements were performed in torque-controlled mode (by applying small torques of 0.5 μNm and a constant oscillation frequency of 1 Hz). The storage and loss moduli were determined for 5 minutes, and one measurement point was recorded every 7.5 seconds. To determine the self-healing behavior of the peptides, the samples were prepared in a vial using the conditions stated above. At the respective time intervals, the gel was destroyed by a vortex mixer (20 seconds) and immediately transferred to the rheometer plate. The rheological measurement was conducted as described above to test for the mechanical recovery abilities of the sample over time.

Confocal fluorescence microscopy

We imaged the behavior of the fiber assemblies on a microscopic level using a Leica DMi8 microscope, including a 63× water immersion objective. We prepared the hydrogels of a total reaction volume of 10 μL directly in incubation chambers (ibidi chamber). The assemblies were stained with 2.5 μM Nile Red. Samples were excited at 552 nm (488 nm in the case of Fmoc-AAC(NBD)-OH) and imaged at 577–650 nm.

Fluorescence spectroscopy

Nile Red assay studies were performed on a Jasco FP-8300 fluorescence spectrophotometer with external temperature control (Jasco MCB-100). The fluorescence intensities were measured over time, each minute, at 635 nm with an excitation at 488 nm. The Fmoc-AAC(NBD)D-OH incorporation experiment was performed by preparing a hydrogel (135 μL of a 13.3 mM Fmoc-AAD-OH solution fueled with 45 μL of a 2000 mM EDC solution) in a vial. After 13 minutes, the gel was damaged (vortex mixed or ultrasonicated for 20 seconds) and pipetted to a 10 mm quartz cuvette from Precision Cells Inc. On top of the damaged gel, 20 μL of a 10 : 1 mixture of Fmoc-AAD-OH to Fmoc-AAC(NBD)D-OH was added. The increase in fluorescence intensity was observed over time. All experiments were performed in triplicate.

Nuclear resonance spectroscopy (NMR)

NMR spectra were recorded on a Bruker AVIII-300, Bruker ARX 300 and AVIII-500-cryo spectrometer by Bruker Analytik at 25 °C and a frequency of 300/300/500 MHz, respectively. Chemical shifts δ are reported in ppm and are referred to the residual solvent peak of the used deuterated solvent (D$_2$O (4.79 (^{1}H))) and dmso-D_6 (2.50 (^{1}H) and 39.5 ppm (^{13}C)). The abbreviation of the signal multiplets are stated as followed: s-singlet, d-doublet, t-triplet, q-quartet, m-multiplet. The coupling constant J referred to the average value in Hz and the coupling between

two protons. The analysis of all received spectra was performed using MestReNova© software (Version 11.0.0.-17609).

^{1}H-NMR ((Fmoc-AAD-OH) 300 MHz, dmso-D_6): δ (ppm) = 12.61 (s, 2H, COOH), 8.10 (d, 1H, ^3J = 8.0 Hz, CONH), 7.99 (d, 1H, ^3J = 7.6 Hz, CONH), 7.89 (d, 2H, ^3J = 7.5 Hz, CH_{aryl}), 7.73 (dd, 2H, ^3J = 6.3 Hz, CH_{aryl}), 7.52 (d, 1H, ^3J = 7.7 Hz, CONH), 7.37 (dt, 4H, ^3J = 7.4 Hz, ^4J = 1.2 Hz, CH_{aryl}), 4.52 (dt, 1H, ^3J = 7.9, 6.1 Hz, CH), 4.31–4.20 (m, 4H,CH CH_2), 4.06 (t, 1H, ^3J = 7.2 Hz, CH), 2.67 (dd, 1H, ^2J = 16.7 Hz, ^3J = 5.8 Hz, CH_2COOH), 2.59 (dd, 1H, ^2J = 16.7 Hz, ^3J = 6.6 Hz, CH_2COOH), 1.23 (dd, 6H, ^3J = 7.1 Hz, CH_3) (see ESI, Fig. 19†).

^{13}C-NMR ((Fmoc-AAD-OH) 250 MHz, dmso-D_6): δ (ppm) = 172.2, 171.9, 155.9, 144.1, 140.9, 127.9, 127.3, 125.6, 120.35, 65.8, 50.1, 48.7, 48.0, 46.8, 36.1, 18.5 (see ESI, Fig. 20†).

^{1}H-NMR ((Fmoc-AVD-OH) 300 MHz, dmso-D_6): δ (ppm) = 12.7 (s, 1H, COOH), 12.45 (s, 1H, COOH), 8.26 (d, 1H, ^3J = 7.8 Hz, CONH), 7.90 (d, 2H, ^3J = 7.6 Hz, CH_{aryl}), 7.83 (d, 1H, ^3J = 7.5 Hz, CONH), 7.73 (dd, 2H, ^3J = 6.3 Hz, CH_{aryl}), 7.59 (d, 1H, ^3J = 7.7 Hz, CONH), 7.38 (dt, 4H, ^3J =7.4 Hz, ^4J = 1.5 Hz, CH_{aryl}), 4.52 (dt, 1H, ^3J = 7.8, 6.5 Hz, CH), 4.28–4.19 (m, 4H, CH, CH_2), 4.15–4.09 (m, 1H, CH), 2.72–2.56 (m, 2H, CH_2), 2.00–1.93 (m, 1H, CH), 1.20 (d, 3H, ^3J = 7.1 Hz, CH_3), 0.83 (dd, 6H, ^3J = 7.1, 6.8 Hz, CH_3) (see ESI, Fig. 21†).

^{13}C-NMR ((Fmoc-AVD-OH) 250 MHz, dmso-D_6): δ (ppm) = 172.8, 172.7, 172.1, 171.1, 156.1, 144.3, 141.2, 128.1, 127.6, 125.8, 120.6, 66.0, 57.4, 50.4, 49.0, 47.1, 36.3, 31.5, 19.6, 18.7, 18.3 (see ESI, Fig. 22†).

^{1}H-NMR ((ac-FIID-OH) 300 MHz, dmso-D_6): δ (ppm) = 12.53 (s, 2H, COOH), 8.19–8.12 (m, 3H, CONH),7.81 (d, 1H, ^3J = 9.0, CONH), 7.25–7.20 (m, 4H, CH_{aryl}), 7.19–7.15 (m, 1H, CH_{aryl}), 4.65 (dd, 1H, ^3J = 8.0, 5.9 Hz, CH), 4.51 (dd, 1H, ^3J = 8.0, 5.9 Hz, CH), 4.18 (dd, 1H, ^3J = 8.9, 7.3 Hz, CH), 2.91 (dd, ^3J = 7.3, 5.7 Hz, CH), 2.75–2.65 (m, 2H, CH_2), 2.55 (dd, 1H, ^3J = 7.1, 5.1 Hz, CH), 1.74 (s, 3H, CH_3), 1.70–1.63 (m, 2H, CH_2COOH), 1.42 (dqd, 1H, ^2J = 12.3 Hz, ^3J = 7.3, 3.2 Hz, CH_2), 1.23 (dqd, 1H, ^2J = 12.4 Hz, ^3J = 7.2, 3.3 Hz, CH_2), 1.05 (dqd, 1H, ^2J = 14.0 Hz, ^3J = 8.9, 7.2 Hz, CH_2), 0.92 (dqd, 1H, ^2J = 14.1 Hz, ^3J = 8.8, 7.1 Hz, CH_2), 0.82–0.71 (m, 12H, CH_3) (see ESI, Fig. 23†).

^{13}C-NMR ((ac-FIID-OH) 250 MHz, dmso-D_6): δ (ppm) = 127.7, 172.1, 171.6, 171.1, 169.4, 138.2, 129.7, 128.4, 126.7, 57.0, 54.3, 48.9, 38.7, 37.1, 36.7, 36.3, 24.5, 22.9, 15.8, 11.4 (see ESI, Fig. 24†).

^{1}H-NMR ((Fmoc-AAC(NBD)D-OH) 300 MHz, dmso-D_6): δ (ppm) = 12.83 (s, 1H, COOH), 12.50 (s, 1H, COOH), 8.56–8.49 (m, 2H, CONH), 8.35 (d, 1H, ^3J = 8.2 Hz, CH_{aryl}CNO$_2$), 8.06 (d, 1H, ^3J = 7.0 Hz, CH_{aryl}CS), 7.87 (d, 2H, ^3J = 7.8 Hz,NH), 7.71 (dd, 2H, ^3J = 11.5, 7.0 Hz, CH_{aryl}), 7.56 (dd, 2H, ^3J = 8.4 Hz, CH_{aryl}), 7.4 (td, 2H, ^3J = 7.5 Hz, ^4J = 2.6 Hz, CH_{aryl}), 7.35–7.30 (m, 2H, CH_{aryl}), 4.78–4.53 (m, 2H, CH_2CHCH$_{aryl}$), 4.26–4.18 (m, 3H, CH), 3.72–3.49 (m, 2H, CH_2S), 2.73–2.67 (m, 2H, CH_2COOH), 1.20 (d, 6H, ^3J = 7.2 Hz, CH_3CH) (see ESI, Fig. 25†).

Dynamic light scattering (DLS)

The critical aggregation concentration (CAC) was determined on a Malvern Zetasizer Nano ZS using a laser wavelength of 633 nm and disposable cuvettes (PS), setting the method of 5

acquisition times of 20 seconds per measurement. A series of low peptide precursor acid concentration was fueled with 500 mM EDC (375 μL of × mM peptide precursor acid solution fueled with 125 μL of a 2000 mM EDC solution, prepared directly in the cuvette) to observe a significant increase in the scattering rate. All measurements were performed in triplicate.

Rheology

We studied the gelation behavior of the peptide assemblies using a commercial shear rheometer (MCR 302, Anton Paar, Graz, Austria) and a plate–plate geometry (bottom plate: P-PTD200/80-I, Anton Paar, equipped with a Ø 55 mm polystyrene Petri-dish (VWR, Radnor, USA); Ø 25 mm steel measuring head: PP25, 79044, Anton Paar). For each measurement, the required sample volume was 180 μL as the plate separation was set to 0.3 mm. A solvent trap (a chamber containing a water-soaked sponge, covered with a lid) as well as a temperature control of the bottom plate (set to 21 °C) was employed for all measurements. All measurements were recorded in triplicate.

Electron spray ionisation-mass spectrometry (ESI-MS)

All samples were investigated by ESI-MS on an LCQ Fleet Ion Trap Mass Spectrometer (Thermo Scientific) in positive mode. All recorded MS data was analyzed in the Thermo Xcalibur Qual Browser 2.2 SP1.48 software.

HRMS (ESI) (Fmoc-AAD-OH) m/z calcd. for $C_{25}H_{27}N_3O_8$: 497.2; found: 497.9 $[M_w + H]^+$, 520.2 $[M_w + Na]^+$, 1016.6 $[2M_w + Na]^+$ (see ESI, Fig. 26†).

HRMS (ESI) (Fmoc-AVD-OH) m/z calcd. for $C_{27}H_{31}N_3O_8$: 525.2; found: 525.9 $[M_w + H]^+$, 1050.7 $[2 M_w + H]^+$, 1072.5 $[M_w + Na]^+$ (see ESI, Fig. 27†).

HRMS (ESI) (ac-FIID-OH) m/z calcd. for $C_{27}H_{40}N_4O_8$: 548.6; found: 549.3 $[M_w + H]^+$, 571.4 $[M_w + Na]^+$, 1118.8 $[2M_w + Na]^+$ (see ESI, Fig. 28†).

HRMS (ESI) (Fmoc-AAC(NBD)D-OH) m/z calcd. for $C_{34}H_{33}N_7O_{12}S$: 763.7; found: 764.1 $[M_w + H]^+$, 786.3 $[M_w + Na]^+$, 802.1 $[M_w + K]^+$ (see ESI, Fig. 29†).

Cryogenic-transmission electron microscopy (cryo-TEM)

We freshly prepared samples of a 50 μL reaction volume for Cryo-TEM. Cryo-TEM imaging was operated on a Tecnai Spirit microscope (FEI/Thermo Fisher) at 120 kV. Herein, the images were recorded in a low-dose mode on a CCD camera. The samples were prepared on Cu-grids (C-flat, 2.0 μm hole size, 2.0 μm hole spacing, 400 mesh) that were freshly glow discharged for 90 seconds at 45 mA and $3 \cdot 10^{-2}$ mbar before use. Samples were prepared as described before. 5 μL of the sample was pipetted on to the Cu-grids in a FEI/Thermo Fisher Vitrobot set to 22 °C and a relative humidity of 100%. The blotting conditions were set to a waiting time of 30 seconds, a blot time of 2.5 seconds and a blot force of −1. Thereafter, grids are plunged into liquid ethane (pre-cooled by liquid nitrogen). The cryo-TEM grids were transferred and stored in liquid nitrogen until they were placed into a Gatan cryo-transfer-specimen holder for imaging. The specimen temperature was maintained at −170 °C

during the whole process. All experiments were performed in triplicate.

UV-Vis spectroscopy

On a Multiskan FC microplate reader (Thermo Fisher), UV-Vis measurements were performed using a 96-well plate (tissue culture plate, non-treated) at 600 nm and 25 °C. All experiments were performed in triplicates.

Data availability

All authors confirm that the data supporting the studies are available within the article and its ESI.†

Author contributions

J. B. and M. A. W. wrote the manuscript, J. R.-F., M. A. W., B. R., A. M. B., M. K. performed the experiments, J. R.-F. and M. A. W. equally contributed to the work. J. B. and O. L. supervised the research.

Conflicts of interest

There are no conflicts to declare.

Acknowledgements

References

1 J. C. Stendahl, M. S. Rao, M. O. Guler and S. I. Stupp, *Adv. Funct. Mater.*, 2006, **16**, 499–508.

2 J. D. Hartgerink, E. R. Zubarev and S. I. Stupp, *Curr. Opin. Solid State Mater. Sci.*, 2001, **5**, 355–361.

3 J. H. K. K. Hirschberg, L. Brunsveld, A. Ramzi, J. A. J. M. Vekemans, R. P. Sijbesma and E. W. Meijer, *Nature*, 2000, **407**, 167–170.

4 D. B. Amabilino, D. K. Smith and J. W. Steed, *Chem. Soc. Rev.*, 2017, **46**, 2404–2420.

5 D. Samanta and R. Klajn, *Adv. Opt. Mater.*, 2016, **4**, 1373–1377.

6 S. O. Krabbenborg, J. Veerbeek and J. Huskens, *Eur. J. Chem.*, 2015, **21**, 9638–9644.

7 R. Freeman, M. Han, Z. Álvarez, J. A. Lewis, J. R. Wester, N. Stephanopoulos, M. T. McClendon, C. Lynsky, J. M. Godbe and H. Sangji, *Science*, 2018, **362**, 808–813.

8 J.-M. Lehn, *Chem. Soc. Rev.*, 2007, **36**, 151–160.

9 K. Liu, Y. Kang, Z. Wang and X. Zhang, *Adv. Mater.*, 2013, **25**, 5530–5548.

10 A. Walther, *Adv. Mater.*, 2020, **32**, 1905111.

11 R. Merindol and A. Walther, *Chem. Soc. Rev.*, 2017, **46**, 5588–5619.

12 T. Heuser, E. Weyandt and A. Walther, *Angew. Chem., Int. Ed.*, 2015, **54**, 13258–13262.

13 G. Wang and S. Liu, *ChemSystemsChem*, 2020, **2**, e1900046.

14 N. Singh, G. J. M. Formon, S. De Piccoli and T. M. Hermans, *Adv. Mater.*, 2020, **32**, 1906834.

15 B. Rieß, R. K. Grötsch and J. Boekhoven, *Chem*, 2020, **6**, 552–578.

16 S. De and R. Klajn, *Adv. Mater.*, 2018, **30**, 1706750.

17 C. A. Angulo-Pachón and J. F. Miravet, *Chem. Commun.*, 2016, **52**, 5398–5401.

18 C. G. Pappas, I. R. Sasselli and R. V. Ulijn, *Angew. Chem.*, 2015, **127**, 8237–8241.

19 D. Pei, B. Liu, S. Zhao, X. Shu, J. Nie and Y. Chang, *ACS Appl. Bio Mater.*, 2021, **4**, 3532–3538.

20 G. Ragazzon and L. J. Prins, *Nat. Nanotechnol.*, 2018, **13**, 882–889.

21 C. Wanzke, M. Tena-Solsona, B. Rieß, L. Tebcharani and J. Boekhoven, *Mater. Horiz.*, 2020, **7**, 1397–1403.

22 M. A. Würbser, P. S. Schwarz, J. Heckel, A. M. Bergmann, A. Walther and J. Boekhoven, *ChemSystemsChem*, 2021, **3**, e2100015.

23 P. S. Schwarz, L. Tebcharani, J. E. Heger, P. Müller-Buschbaum and J. Boekhoven, *Chem. Sci.*, 2021, **12**, 9969–9976.

24 B. G. P. van Ravensteijn, W. E. Hendriksen, R. Eelkema, J. H. van Esch and W. K. Kegel, *J. Am. Chem. Soc.*, 2017, **139**, 9763–9766.

25 T. Heuser, R. Merindol, S. Loescher, A. Klaus and A. Walther, *Adv. Mater.*, 2017, **29**, 1606842.

26 S. P. Afrose, S. Bal, A. Chatterjee, K. Das and D. Das, *Angew. Chem., Int. Ed.*, 2019, **58**, 15783–15787.

27 M. Tena-Solsona, C. Wanzke, B. Riess, A. R. Bausch and J. Boekhoven, *Nat. Commun.*, 2018, **9**, 1–8.

28 S. Debnath, S. Roy and R. V. Ulijn, *J. Am. Chem. Soc.*, 2013, **135**, 16789–16792.

29 S. Chandrabhas, S. Maiti, I. Fortunati, C. Ferrante, L. Gabrielli and L. J. Prins, *Angew. Chem., Int. Ed.*, 2020, **59**, 22223–22229.

30 H. Che, S. Cao and J. C. M. van Hest, *J. Am. Chem. Soc.*, 2018, **140**, 5356–5359.

31 R. K. Grötsch, A. Angı, Y. G. Mideksa, C. Wanzke, M. Tena-Solsona, M. J. Feige, B. Rieger and J. Boekhoven, *Angew. Chem., Int. Ed.*, 2018, **57**, 14608–14612.

32 R. Klajn, P. J. Wesson, K. J. M. Bishop and B. A. Grzybowski, *Angew. Chem., Int. Ed.*, 2009, **48**, 7035–7039.

33 B. Rieß and J. Boekhoven, *ChemNanoMat*, 2018, **4**, 710–719.

34 E. Olivieri, B. Gasch, G. Quintard, J.-V. Naubron and A. Quintard, *ACS Appl. Mater. Interfaces*, 2022, **14**, 24720–24728.

35 M. Grzelczak, J. Vermant, E. M. Furst and L. M. Liz-Marzán, *ACS Nano*, 2010, **4**, 3591–3605.

36 L. Schaedel, K. John, J. Gaillard, M. V. Nachury, L. Blanchoin and M. Théry, *Nat. Mater.*, 2015, **14**, 1156–1163.

37 B. M. Mulder and M. E. Janson, *Nat. Mater.*, 2015, **14**, 1080–1081.

38 J. Boekhoven, W. E. Hendriksen, G. J. M. Koper, R. Eelkema and J. H. v. Esch, *Science*, 2015, **349**, 1075–1079.

39 M. Tena-Solsona, B. Rieß, R. K. Grötsch, F. C. Löhrer, C. Wanzke, B. Käsdorf, A. R. Bausch, P. Müller-Buschbaum, O. Lieleg and J. Boekhoven, *Nat. Commun.*, 2017, **8**, 15895.

40 B. A. K. Kriebisch, A. Jussupow, A. M. Bergmann, F. Kohler, H. Dietz, V. R. I. Kaila and J. Boekhoven, *J. Am. Chem. Soc.*, 2020, **142**, 20837–20844.

41 F. Schnitter and J. Boekhoven, *ChemSystemsChem*, 2021, **3**, e2000037.

42 B. Kriebisch, C. Kriebisch, A. Bergmann, C. Wanzke, M. Tena-Solsona and J. Boekhoven, 2022.

43 S. Martinotti and E. Ranzato, in *Epidermal Cells: Methods and Protocols*, ed. K. Turksen, Springer US, New York, NY, 2020, pp. 225–229. DOI: DOI: **10.1007/7651_2019_259**.

44 K. A. Main, C. M. Mikelis and C. L. Doçi, in *Epidermal Cells: Methods and Protocols*, ed. K. Turksen, Springer US, New York, NY, 2020, pp. 147–154, DOI: DOI: **10.1007/7651_2019_235**.

45 M. Kretschmer, B. Winkeljann, B. A. Kriebisch, J. Boekhoven and O. Lieleg, *Commun. Mater.*, 2021, **2**, 1–10.

46 J. M. A. Carnall, C. A. Waudby, A. M. Belenguer, M. C. A. Stuart, J. J.-P. Peyralans and S. Otto, *Science*, 2010, **327**, 1502–1506.

47 M. Colomb-Delsuc, E. Mattia, J. W. Sadownik and S. Otto, *Nat. Commun.*, 2015, **6**, 7427.

48 K. Dai, J. R. Fores, C. Wanzke, B. Winkeljann, A. M. Bergmann, O. Lieleg and J. Boekhoven, *J. Am. Chem. Soc.*, 2020, **142**, 14142–14149.

A chemically fueled supramolecular glue for self-healing gels†

Jennifer Rodon-Fores[1‡], Michaela A. Würbser[1‡], Martin Kretschmer[2,3], Benedikt Rieß[1], Alexander M. Bergmann[1], Oliver Lieleg[2,3], Job Boekhoven[1*]

‡ Co-first authorship, the two authors have contributed equally to the paper.

[1] Department of Chemistry, Technical University of Munich, Lichtenbergstrasse 4, 85748 Garching, Germany.

[2] TUM School of Engineering and Design, Department for Materials Engineering, Technical University of Munich, Boltzmannstr. 15, 85748, Garching, Germany.

[3] Center for Protein Assemblies (CPA) & Munich Institute of Biomedical Engineering (MIBE), Technical University of Munich, Ernst-Otto-Fischer-Str. 8, 85748 Garching.

Supporting tables

Supporting Table S1. Characterization of synthesized peptide precursors (and commercially available benzylamine and EDC HCl).

Substance (abb.)	Structure	Mass M_w calculated [gmol^{-1}]	Mass found [gmol^{-1}]	Retention time [min]	Calibration value [mAUmM^{-1}] (2uL)
Fmoc-AAD-OH		497.2 $C_{25}H_{27}N_3O_8$	497.9 [M_w+H]$^+$ 520.2 [M_w+Na]$^+$ 1016.6 [2M_w+Na]$^+$	9.7	16.65 (220 nm)
Fmoc-AVD-OH		525.2 $C_{27}H_{31}N_3O_8$	525.9 [M_w+H]$^+$ 1050.7 [2M_w+H]$^+$ 1072.5 [2M_w+Na]$^+$	11.1	12.51 (220 nm)
Ac-FIID-OH		548.6 $C_{27}H_{40}N_4O_8$	549.3 [M_w+H]$^+$ 571.4 [M_w+Na]$^+$ 1118. 8 [2M_w+Na]$^+$	8.9	7.72 (220 nm)
Fmoc-AAC(NBD)D-OH		763.7 $C_{34}H_{33}N_7O_{12}S$	764.1 [M_w+H]$^+$ 786.3 [M_w+Na]$^+$ 802.1 [M_w+K]$^+$	11.7	-
EDC· HCl		191.7 $C_8H_{17}N_3$ · HCl	-	1.38	1.75 (220 nm)
BA		107.2 C_7H_9N	-	2.38	0.37 (220 nm)

Supporting Table S2: Summary of rate constants of the peptide precursor acids for the reaction cycle using the kinetic model.

Peptide precursor/ order of rate	k_0 [s^{-1}]	k_1 [$M^{-1}s^{-1}$]	k_2 [s^{-1}]	k_3 [s^{-1}]	k_4 [s^{-1}]	Half-life (anhydride) [s] $\tau_{1/2} = \ln(2)/k_4$
Order	1st	2nd	1st	1st	1st	-
[a]**Fmoc-AAD-OH**	1.35×10^{-6}	0.045	0.8	0.35	0.015	46
[b]**Fmoc-AVD-OH**	7.0×10^{-6}	0.280	$2 \times k_1$	$2.5 \times k_1$	0.015	46
[c]**Ac-FIID-OH**	1.35×10^{-6}	0.95×10^{-2}	$2 \times k_1$	$2 \times k_1$	0.75×10^{-2}	92

a.   10 mM Fmoc-AAD-OH fueled with 500 mM EDC.
b.   10 mM Fmoc-AVD-OH fueled with 100 mM EDC.[1]
c.   15 mM ac-FIID-OH fueled with 25 mM EDC.[2]

Supporting figures
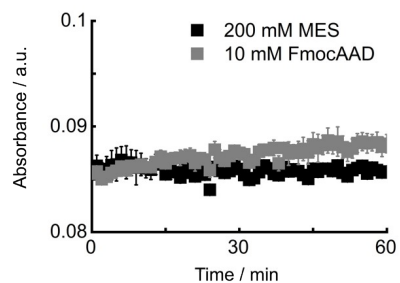
Fig. 1: UV/Vis absorbance at 600 nm over time of 200 mM MES buffer (black) and 10 mM peptide precursor acid Fmoc-AAD-OH in 200 mM MES without fuel (grey). All experiments were performed in triplicate.
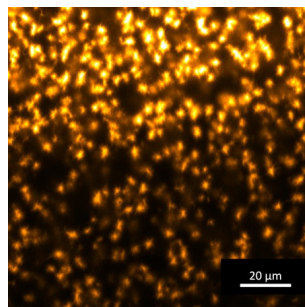
Fig. 2: Confocal fluorescence micrograph of 10 mM peptide precursor acid Fmoc-AAD-OH fueled with 500 mM EDC showing a dense network of fiber bundles.
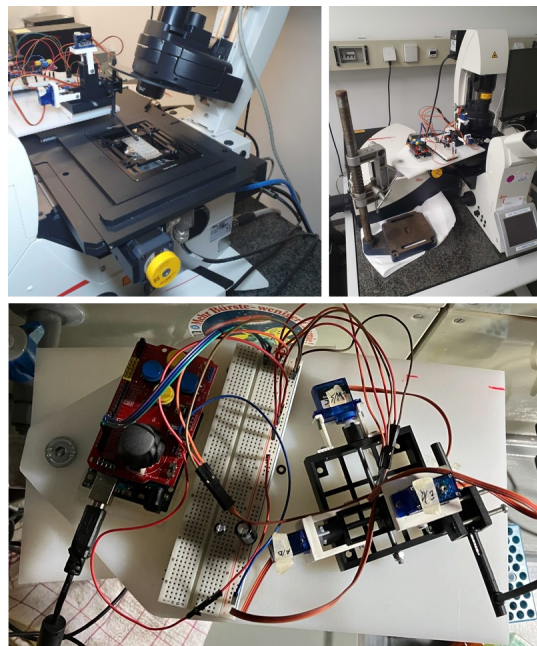
Fig. 3:Photographs of the micromanipulator while performing a scratch through a hydrogel (10 mM Fmoc-AAD-OH fueled with 500 mM EDC) (left) and the entire micromanipulator in wholesome profile view (right) and top view (bottom).
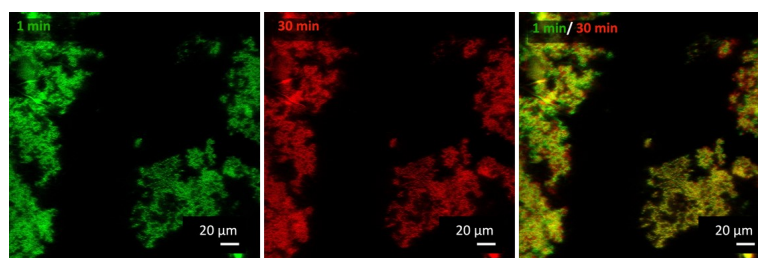
Fig. 4: Confocal micrographs of 10 mM Fmoc-AAD-OH acidified with 500 mM 1 minute (green) after performing a scratch 13 minutes after fuel addition and after 30 minutes (red). The composites showed no healing of the network after 30 minutes. The acidification took place in a faster manner compared to fueling with EDC resulting in nanofibers, but in a more agglomerated assembly structure leading to an uneven scratch. All experiments were performed in triplicate.
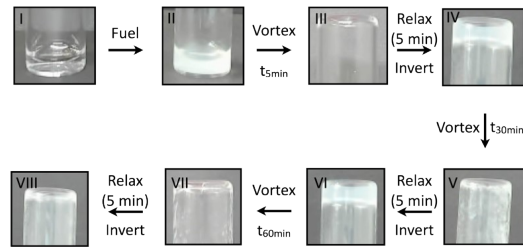
Fig. 5: Vial inversion test of 10 mM Fmoc-AAD-OH (I) fueled with 500 mM EDC (II). The hydrogel was vortex mixed for 20 seconds 5 minutes after fuel addition (III) showing the full liquification of the gel. It was then set to relax for 5 min and inverted resulting again in a self-supporting gel (IV). This procedure was repeated at the time intervals t = 30 min (V, VI) and 60 minutes (VII, VIII). All experiments were carried out in triplicate.
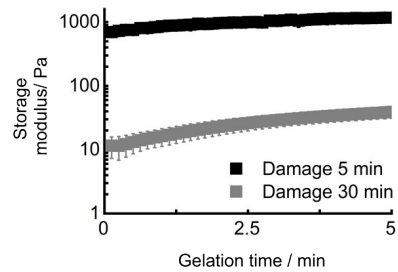

Fig. 6: Storage modulus recovery of 10 mM Fmoc-AAD-OH fueled with 500 mM EDC over a gelation time of 5 minutes after damaging the gel 5 minutes (black) and 30 minutes after fuel addition (grey). All experiments were performed in triplicate.
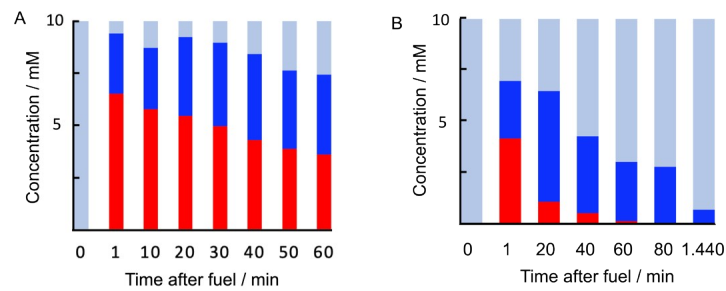

Fig. 7: Precursor remains kinetically trapped in fibers. The concentration of peptide precursor acid in the fiber assembly (blue), peptide product in the fiber assembly (red) and the peptide in solution (light blue) were determined by ¹H-NMR spectroscopy of 10 mM Fmoc-AAD-OH fueled with 500 mM EDC (A) or with 100 mM EDC (B). All experiments were performed in triplicate.
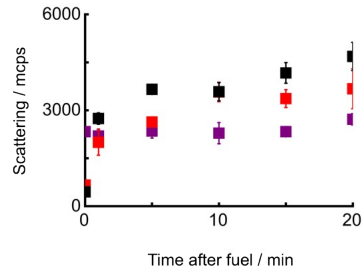
Fig. 8: Critical aggregation concentration of peptide precursor acid Fmoc-AAD-OH according to an increased scattering rate over time determined by DLS. Compared to 500 mM EDC in 200 mM MES buffer (purple), a significant increase in the scattering at t = 15 minutes was observed between 0.6 mM (red) and 0.8 mM (black) Fmoc-AAD-OH fueled with 500 mM EDC. Markers represent DLS data. The error bars show the standard deviation from the average (n = 3).
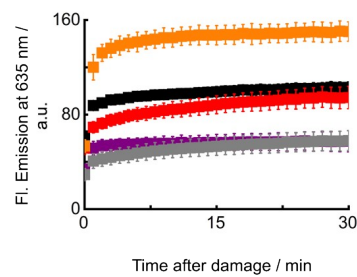

Fig. 9: NBD fluorescence intensity at 635 nm after excitation at 488 nm over time after the damage as a measure for the positive incorporation of Fmoc-AAC(NBD)D-OH into the Fmoc-AAD-OH network after an externally induced damage. A gel consisting of a mixture of 10 mM Fmoc-AAD-OH and 0.5 mM Fmoc-AAC(NBD)D-OH fueled with 500 mM EDC without damage (grey) showed a similar fluorescence emission as performing 0.5 mM Fmoc-AAC(NBD)D-OH with 500 mM EDC (aq.) with no damage (purple). In contrast, vortex mixing (red) or ultrasonication (black) of the hydrogel (10 mM Fmoc-AAD-OH fueled with 500 mM EDC) after 13 minutes and adding a mixture of Fmoc-AAD with 0.5 mM Fmoc-AAC(NBD)D-OH, led to an increased intensity (and thus to the incorporation of NBD-building blocks). The highest intensity (positive control) was achieved by directly preparing the hydrogel using 10 mM Fmoc-AAD-OH with 0.5 mM Fmoc-AAC(NBD)D-OH fueled with 500 mM EDC (orange). All markers represent experimental data in triplicate.
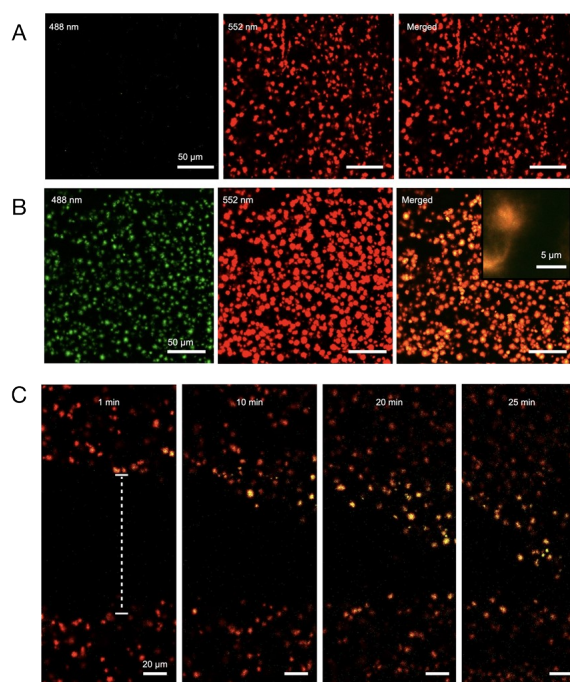
Fig. 10: Incorporation of NBD-based peptide in damaged gels. A) Confocal micrographs of the undamaged gel (10 mM Fmoc-AAD fueled with 500 mM EDC, stained with 0.1 μM Nile Red). 1 μL of a 10:1 mixture of Fmoc-AAD-OH and Fmoc-AAC(NBD)D-OH was added on top of the preformed gel. **B)** Confocal micrographs of the damaged gel (10 mM Fmoc-AAD fueled with 500 mM EDC, stained with 0.1 μM Nile Red). 1 μL of a 10:1 mixture of Fmoc-AAD-OH to Fmoc-AAC(NBD)D-OH was added on top of the preformed gel and damaged by ultrasonication for 2 minutes (13 minutes after fuel addition). **C)** Confocal micrographs of 10 mM Fmoc-AAD fueled with 500 mM EDC. After 13 minutes, a scratch was performed by applying a needle topped with 1 μL of a 10:1 mixture of Fmoc-AAD-OH and Fmoc-AAC(NBD)D-OH. The incorporation of the NBD-labeled peptide was observed over time. All experiments were carried out in triplicate.
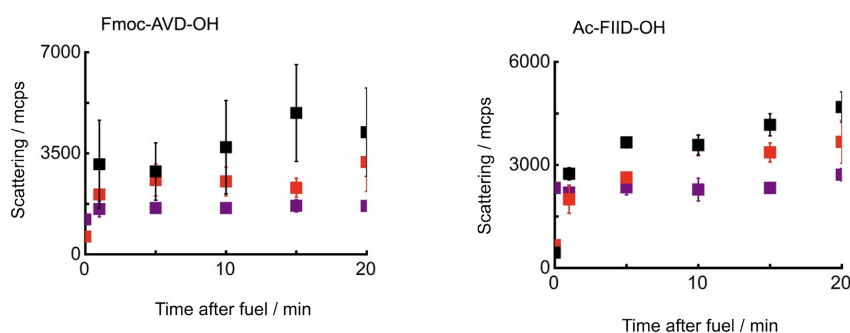

Fig. 11: Critical aggregation concentration of peptide precursor acid Fmoc-AVD-OH (left) and ac-FIID-OH (right) as measured by an increased scattering rate over time determined by DLS. Compared to 500 mM EDC in 200 mM MES buffer (purple), a significant increase in the scattering at t = 15 minutes was observed between 0.1 mM (red) and 0.3 mM (black) Fmoc-AVD-OH fueled with 500 mM EDC. Compared to 500 mM EDC in 200 mM MES buffer (purple), a significant increase in the scattering at t = 15 minutes was observed between 0.2 mM (red) and 0.3 mM (black) for ac-FIID-OH fueled with 500 mM EDC. Markers represent DLS data. The error bars show the standard deviation from the average (n = 3).
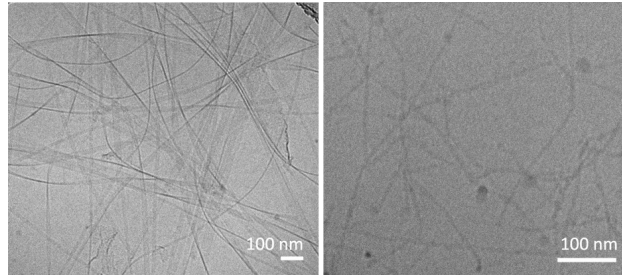
Fig. 12: Cyro-TEM micrographs of 10 mM Fmoc-AVD-OH fueled with 10 mM EDC (left) and 15 mM ac-FIID-OH fueled with 25 mM EDC (right). The micrographs were taken 1 minute after fuel addition. Both peptides formed a nanofibrillar network. All experiments were performed in triplicate.
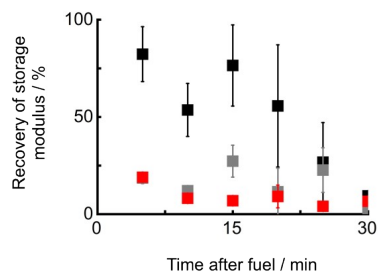

Fig. 13: Recovery of storage modulus of 10 mM peptide precursor acids Fmoc-AAD-OH (black), Fmoc-AVD-OH (grey) and ac-FIID-OH (red) fueled with 500 mM EDC damaging at various time intervals after fuel addition. Markers represent storage modulus data. The error bars show the standard deviation from the average (n = 3).
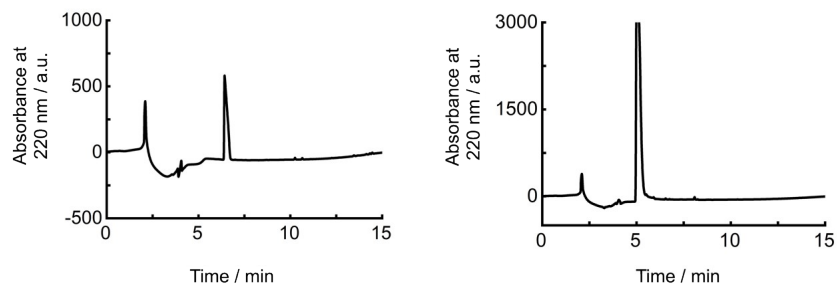

Fig. 14: HPLC chromatograms of 500 mM BA (left) and 500 mM EDC measured at 220 nm (injection volume 2 µL).

Fig. 15: HPLC chromatograms of 10 mM Fmoc-AAD-OH (left) and the entire reaction cycle 5 minutes after fuel addition (right) measured at 220 nm (injection volume 2μL).
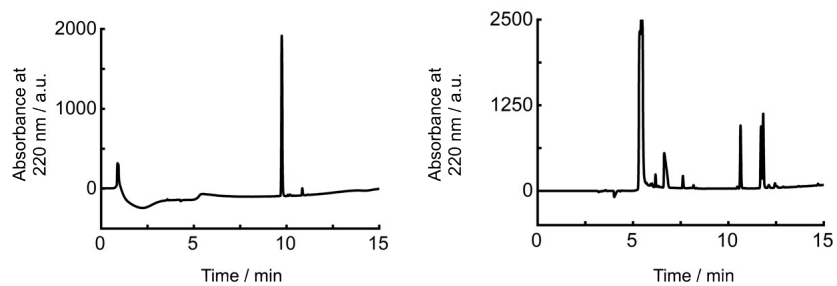

Fig. 16: HPLC chromatograms of 10 mM Fmoc-AVD-OH (left) and the entire reaction cycle 5 minutes after fuel addition (right) measured at 220 nm (injection volume 2 μL).
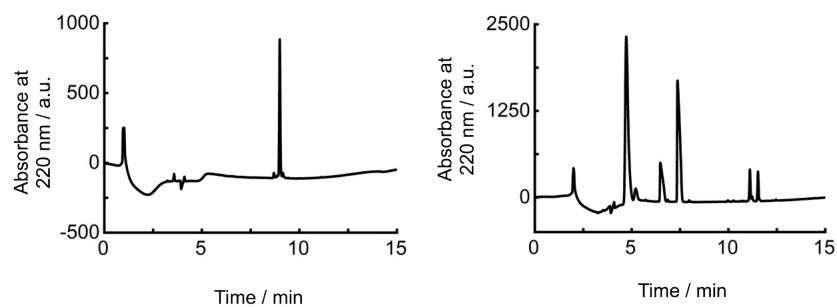
Fig. 17: HPLC chromatograms of 10 mM ac-FIID-OH (left) and the entire reaction cycle 5 minutes after fuel addition (right) measured at 220 nm (injection volume 2).
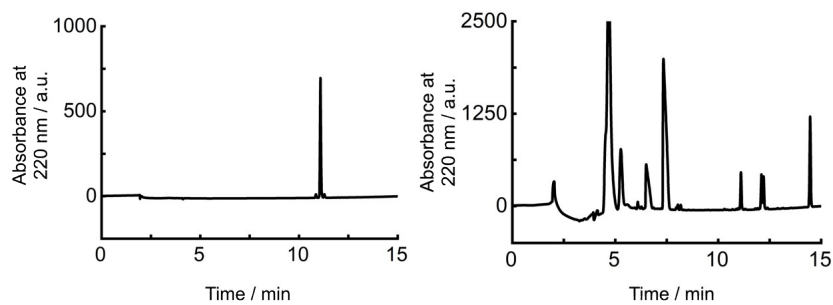
.
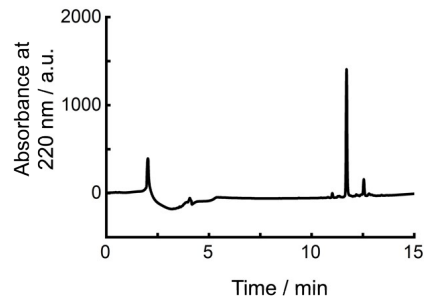
Fig. 18: HPLC chromatograms of 10 mM Fmoc-AAC(NBD)D measured at 220 nm (injection volume 2 μL).

Fig. 19: ¹H-NMR (dmso-D₆, 300 MHz, 25 °C) spectrum of Fmoc-AAD-OH in dmso-D₆.

Fig. 20: ^{13}C-NMR (dmso-D$_6$, 250 MHz, 25 °C) spectrum of Fmoc-AAD-OH in dmso-D$_6$.
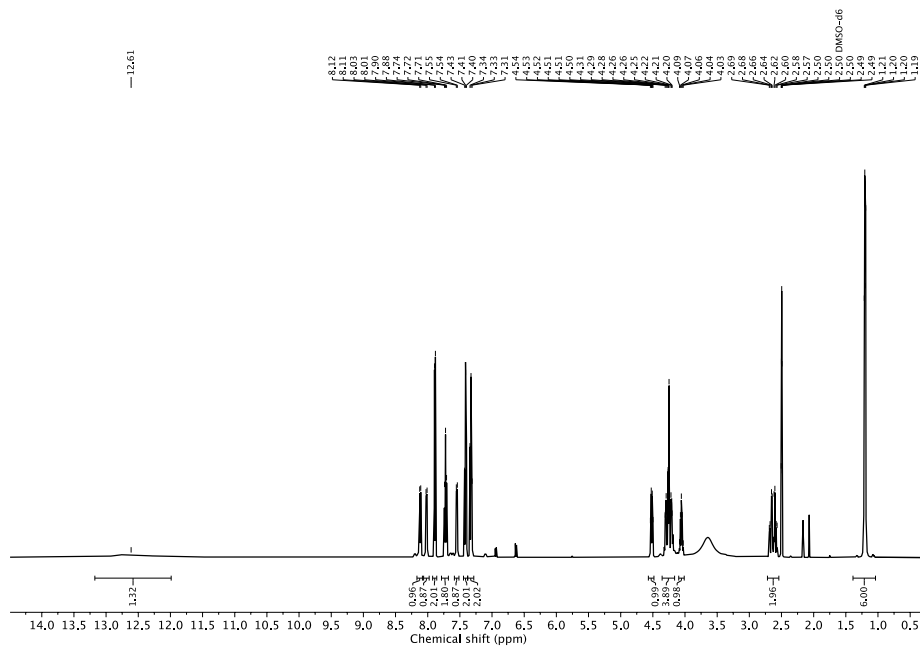
Fig. 21: ^{1}H-NMR (dmso-D$_6$, 300 MHz, 25 °C) spectrum of Fmoc-AVD-OH in dmso-D$_6$.
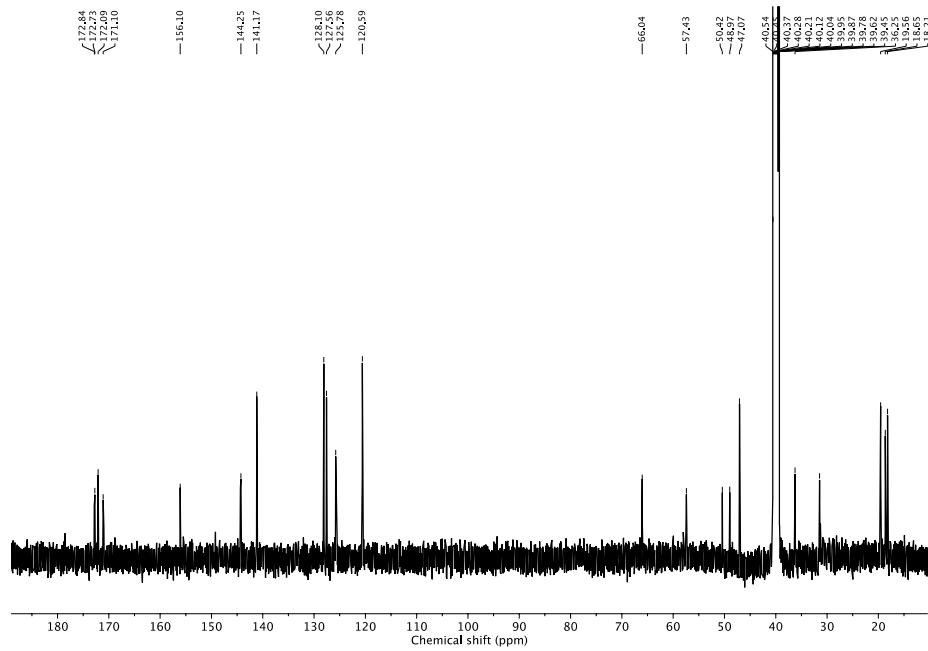
Fig. 22: ^{13}C-NMR (dmso-D$_6$, 250 MHz, 25 °C) spectrum of Fmoc-AVD-OH in dmso-D$_6$.
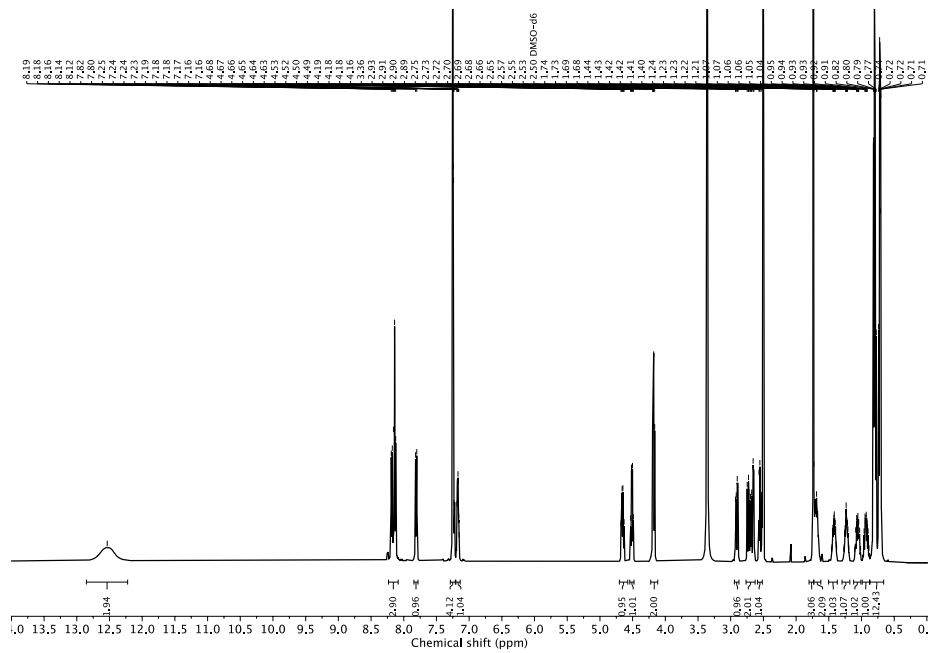
Fig. 23: ^{1}H-NMR (dmso-D$_6$, 300 MHz, 25 °C) spectrum of ac-FIID-OH in dmso-D$_6$.
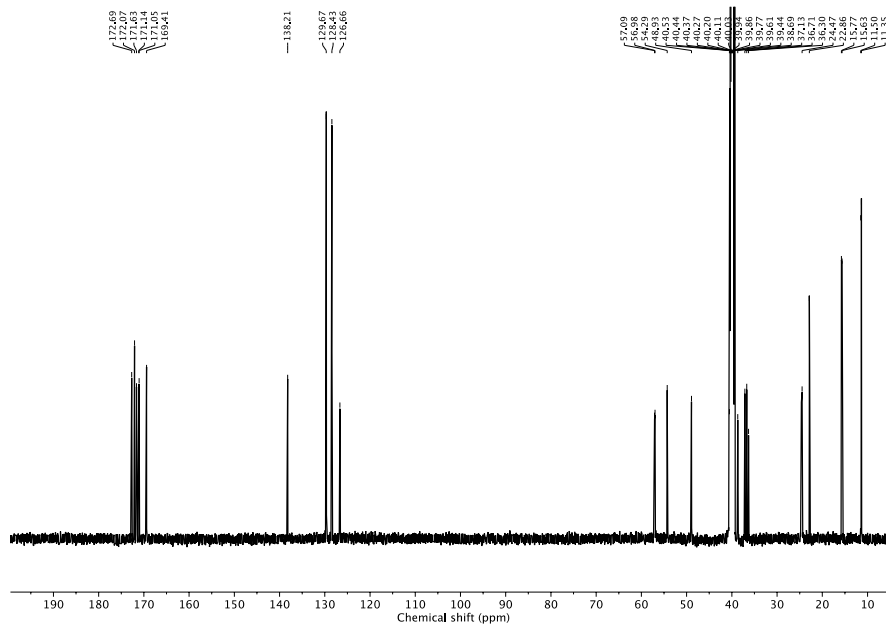
Fig. 24: ^{13}C-NMR (dmso-D$_6$, 250 MHz, 25 °C) spectrum of ac-FIID-OH in dmso-D$_6$.
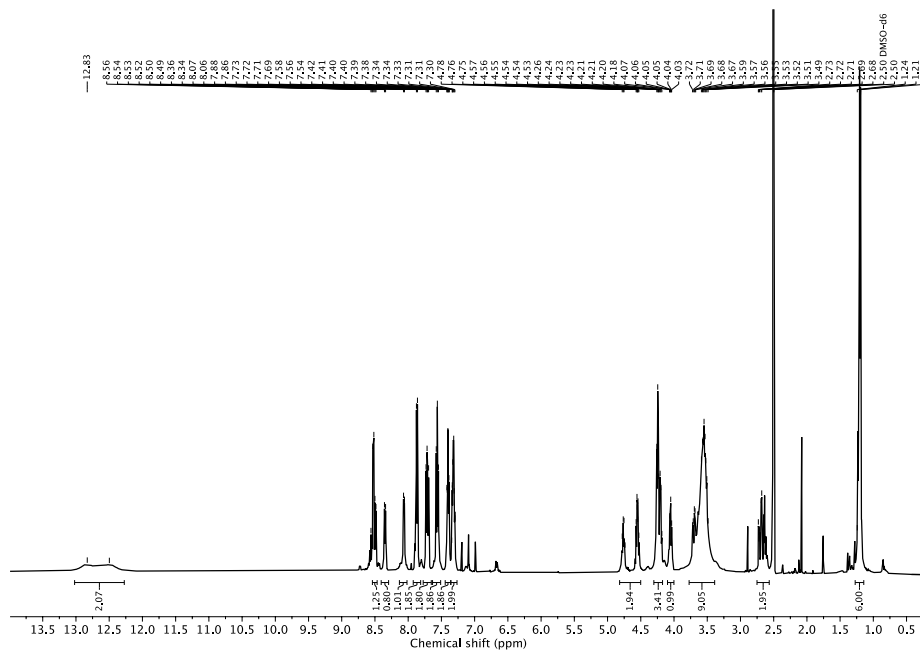
Fig. 25: ^{1}H-NMR (dmso-D$_6$, 300 MHz, 25 °C) spectrum of Fmoc-AAC(NBD)D-OH in dmso-D$_6$.
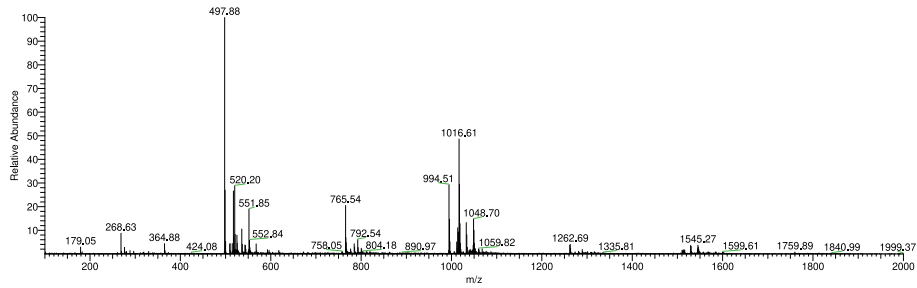
Fig. 26: ESI-MS characterization of peptide precursor acid Fmoc-AAD-OH.
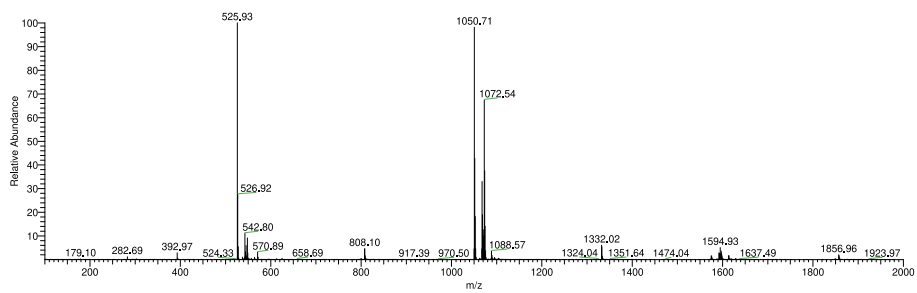
Fig. 27: ESI-MS characterization of peptide precursor acid Fmoc-AVD-OH.
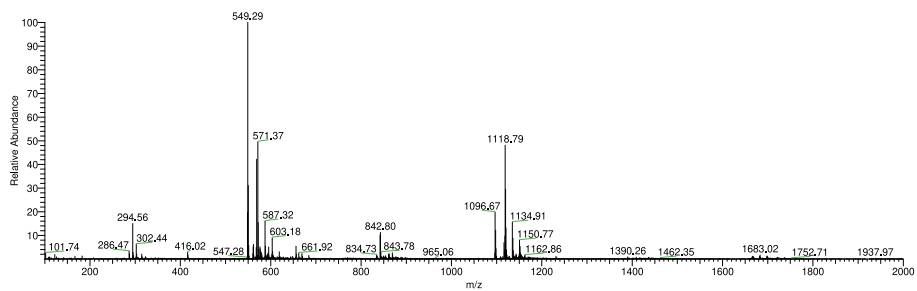
Fig. 28: ESI-MS characterization of peptide precursor acid ac-FIID-OH.
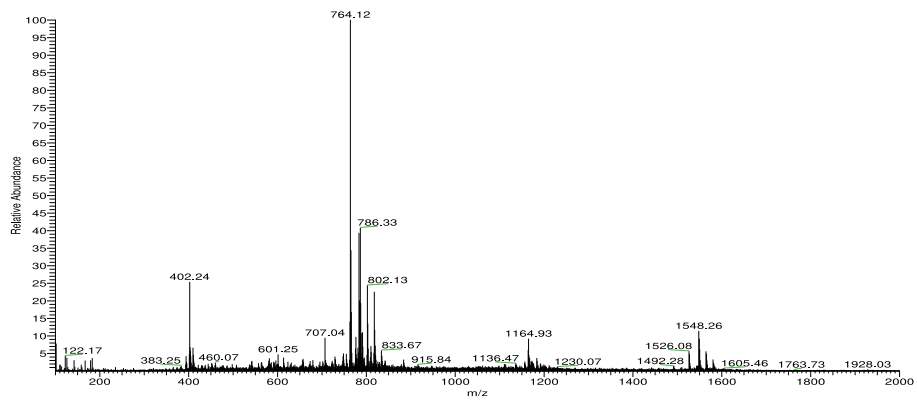
Fig. 29: ESI-MS characterization of peptide precursor acid Fmoc-AAC(NBD)D-OH.

Supporting notes

Description of the kinetic model. We used a *Matlab* code as kinetic model to calculate the concentrations of each reactant for every second i in the reaction cycle (peptide precursor acid, carbodiimide fuel, intermediate product, peptide product). Herein, the model consists of five differential equations which represent the five underlying chemical reactions: (1) the pseudo first-order hydrolysis reaction of EDC r_0, (2) the second-order reaction of the peptide precursor acid with the carbodiimide fuel to form the intermediate product, (3) the first-order peptide anhydride formation reaction r_2, (4) the pseudo first-order hydrolysis reaction of the intermediate product r_3, (5) the pseudo-first order hydrolysis reaction of the peptide anhydride product r_4. The rate constants k_0 and k_1 were investigated using the experimental HPLC data by monitoring the EDC concentration over time. The rate constants k_2, k_3 and k_4 were determined by fitting using the kinetic model.
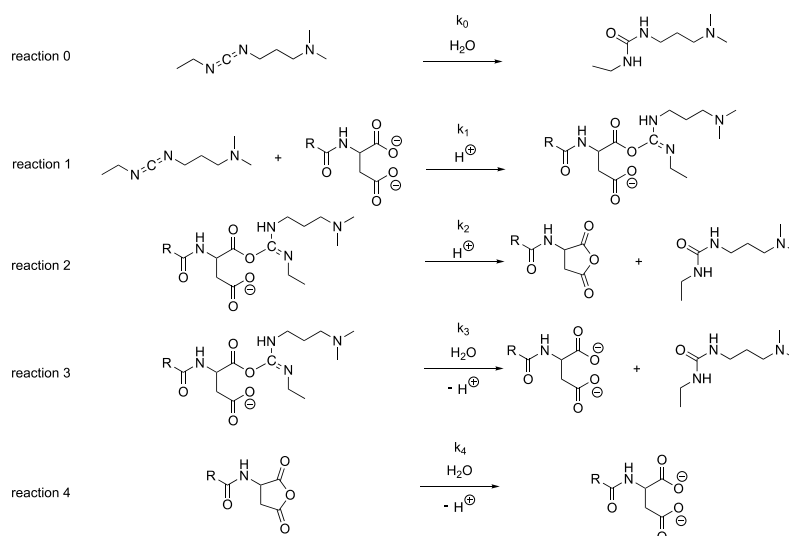
Scheme 1: Schematic representation of the chemical reactions of the kinetic model in the EDC-driven reaction cycle of peptide precursor acids. (reaction 0) Pseudo-first order hydrolysis reaction of EDC. (reaction 1) Second order reaction of the peptide precursor with EDC to form the intermediate product *O*-acylisourea. (reaction 2) First-order reaction of the intermediate product *O*-acylisourea to the anhydride product and urea waste product. (reaction 3) Pseudo first-order hydrolysis reaction of the intermediate product O-acylisourea to form the initial peptide precursor and urea waste product. (reaction 4) Pseudo-first order hydrolysis reaction of the peptide anhydride product to form the initial peptide precursor acid. See Supporting notes for a detailed discussion on the rates and rate constants.

$$r_0(i) = k_0 \cdot EDC(i) \tag{1}$$

$$r_1(i) = k_1 \cdot EDC(i) \cdot COOH(i) \tag{2}$$

$$r_2(i) = k_2 \cdot COOEDC(i) \tag{3}$$

$$r_3(i) = k_3 \cdot COOEDC(i) \tag{4}$$

- 91 -

$$r_4(i) = k_4 \cdot COOOC(i), \tag{5}$$

References

1.   B. A. K. Kriebisch, A. Jussupow, A. M. Bergmann, F. Kohler, H. Dietz, V. R. I. Kaila and J. Boekhoven, *J. Am. Chem. Soc.*, 2020, **142**, 20837-20844.
2.   K. Dai, J. R. Fores, C. Wanzke, B. Winkeljann, A. M. Bergmann, O. Lieleg and J. Boekhoven, *J. Am. Chem. Soc.*, 2020, **142**, 14142-14149.

7 Conclusion and outlook

This thesis aimed for the design of supramolecular materials that display life-like behavior by coupling a chemical fuel conversion to the material formation process.

Life is highly complex, therefore, in chapter one, I introduced diverse concepts of nature, showing how sophisticated functions, *e.g.*, responsiveness, sensing, self-healing, or temporal control, can emerge.

Chapter two dealt with the aims of my thesis.

In chapter three, I had a closer look at dissipative, out-of-equilibrium pathways. Since the self-assembly process is coupled to energy consumption, materials can be endowed with unique properties. Specifically, by applying a chemical fuel as an energy source that a chemical reaction network can liberate, we can control where and when energy is released. As long as fuel is present, activation of the building blocks will drive the self-assembly process. At the same time, disassembly is initiated through a deactivation reaction of the building blocks leading to the structure's decay. This principle means that the material's structure formation or properties are transient, i.e., temporally controlled. The cytoskeleton's microtubule is one prominent biological example of functionality caused by dissipative self-assembly. Herein, the energy transduction is based on the hydrolysis of GTP to GDP. I reflected on several temporally regulated materials based on chemically fueled self-assembly and was especially convinced by applying a carbodiimide-driven reaction cycle, presenting a versatile and simple approach.

In chapter four, we used EDC-driven self-assembly of a diblock copolymer to create transient micellar nanoreactors. We showed that multiple activations of chemical building blocks within one polymer strain were feasible. This fuel-switchable change in amphiphilicity resulted in the self-assembly of transient micelles that were applied as nanoreactors to locally up-concentrate hydrophobic reagents of a Diels-Alder reaction. To our surprise, the micelles' lifetime and the yield of Diels-Alder product were tuned by the provided fuel amount.

We used this concept to design a material that possesses an even higher level of functionality, e.g., to create an adaptable material with self-healing properties. Therefore, in chapter five, I explained previous discoveries of artificial self-healing materials and that they can be categorized according to intrinsic or extrinsic, autonomous or non-autonomous self-healing. Moreover, man-made self-healing materials demonstrated that strategies, e.g., healing through microencapsulation, dynamic covalent bond formation or non-covalent interactions, was successful yet not comparable to the autonomous self-restoring abilities of biological systems. But it emphasized, that dynamic or reversible bond formation, as demonstrated by microtubules based on chemically fueled self-assembly, could be a key element. Indeed, one

rare synthetic material demonstrated self-healing based on chemical fuel-driven self-assembly, but the underlying mechanistic processes remained unclear.

Hence, in chapter six, we created a self-healing peptide fiber hydrogel induced by an EDC-driven self-assembly process. Interestingly, the gel only displayed dynamism in case of rupture compared to the undamaged state resulting in the self-healing of the fibrillar system. We hypothesized a concept of a chemical-fueled molecular glue assisting the healing process. The building blocks are activated and self-assembled by applying a high fuel amount. We assume that a small peptide concentration under the critical aggregation concentration remains in solution, and is activated but does not result in assemblies. The fibers' damage drastically increases the number of nucleation sites, enhancing the incorporation of the building blocks, i.e., they act as a molecular glue. We also investigated other peptide systems and found an important correlation between the system's CAC and its healing efficiency.

Overall, approaching life-like materials by a chemical fuel-driven self-assembly process is a versatile tool to introduce unique properties to a material. It demonstrates that the fuel concentration can accurately tune a material's lifetime, and the inherently dynamic fashion of the system can induce the ability to self-heal.

The discussed studies mainly focused on soft matter featuring life-like properties. Specifically, the presented self-healing hydrogel could inspire the creation of materials in the field of, e.g., regenerative medicine or tissue engineering, if applied in a more biocompatible and bioactive fashion. Moreover, the applied chemical fuel-driven approach created an intrinsically self-healing hydrogel displaying tunable structural, mechanical, and rheological features. This could be especially appealing regarding 3D printing, soft robotics, or assisted health technology, where mechanical robustness yet high intrinsic self-healing efficiency is strongly demanded. Correct design adjustments and under consideration of the presented underlying self-healing mechanisms could create a material that balances sufficient mechanical robustness with great self-healing ability.
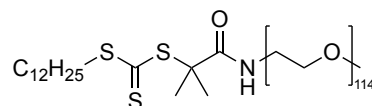
8 Materials and methods

Materials

We purchased α-amino,ω-methoxy-poly(ethylene glycol) (mPEG$_{114}$-NH, M_n = 5000 gmol^{-1}), 2-(dodecylthio-carbonothioylthio)-2-methylpropionic acid (DDMAT, 98%), maleic anhydride (>99%), 2,2 azobis(2-methyl-propionitril) (AIBN, 98%), 2-(*N*-morpholino)ethane sulfonic acid (MES buffer, 99.5%), styrene (>99%), 1-ethyl-3(3-dimethylaminopropyl)carbo-diimide hydrochloride (EDC · HCl, 99%), Nile Red (MQ 100), (*E/E*)-2,4-hexadiene acid ethyl ester (**2b**, >98%), (*E/E*)-2,4-Hexadien-1-ol (**2a**, >97%), *N*-benzyl maleimide (**1**, 99%), benzylamine (BA, 99%), dichloromethane (DCM, >99%), deuterated dimethyl oxide (DMSO-D$_6$, 100%, 99.96 atom % D), deuterium oxide (D$_2$O, 99.96 atom % D), deuterated chloroform-d$_1$ (99.8 atom % D), *N,N'*-diisopropyl-carbodiimide (DIC, 99%), 37w.%. hydrochloric acid (HCl, MQ 200), 2-(*N*-morpho-lino)ethane sulfonic acid (MES, 99.5%), piperidine (99%), Fmoc-D(O*t*Bu)-wang resin (100-200 Mesh size, loading 0.67 mmol.g^{-1}), protected amino acids (Fmoc- A-OH (95%), Fmoc-V-OH (>98%), Ac-F-OH (98%), Fmoc-I-OH (98%)), sodium hydroxide (NaOH, >98%), *N,N*-dimethylformamide (DMF, 99.8%), diethyl ether (Et$_2$O, >99%) trifluoroacetic acid (TFA, 99%), triisopropylsilane (TIPS, 99%), *N*-Ethyldiisopropylamine (99%, DIEA), 4-chloro-7-nitrobenzo-furazan (NBD-Cl, 98%), ß-mercaptoethanol (>99%) and 4-methyl-morpholine (NMM, 99%) from *Sigma-Aldrich*. Oxalyl chloride (98%) was purchased from *ABCR*. We purchased triethylamine (NEt$_3$, >99.5%) from *Carl Roth*. High-performance liquid chromatography (HPLC) grade acetonitrile (ACN) was purchased from *VWR*. We removed the contained inhibitors of styrene by passing over basic alumina. Hydroquinone (99%) was purchased from *Thermo Fisher Scientific* and oxyma (97%) from *Novabiochem*. All chemicals were used without any further purification unless stated differently.

Synthesis

Preparation of pegylated RAFT-agent (PEG$_{114}$-DDMAT).

To a solution of DDMAT (2-(dodecylthiocarbonothioylthio)-2-methylpropionic acid, 1.53 g, 4.20 mmol) in DCM (20 mL), oxalyl chloride (1.07 g, 8.43 mmol, 2.0 eq.) was added dropwise at 0 °C, followed by the addition of catalytic amount of DMF (20.0 µL, 18.9 mg, 0.26 mmol, 0.06 eq.). The reaction mixture was stirred at 0 °C for 2 hours, after which the solvent and residual oxalyl chloride were removed under reduced pressure. The residue was dissolved in

DCM (20 mL), and cooled to 0°C. To this, a solution of mPEG$_{114}$-NH (α-amino,ω-methoxy poly(ethylene glycol), M_n = 5000 gmol^{-1}, 2.10 g, 0.42 mmol, 0.1 eq.) and NEt$_3$ (0.58 mL, 425 mg, 4.20 mmol, 1.0 eq) in DCM (20 mL) was added dropwise and the reaction mixture was stirred at 0 °C for 30 minutes, followed by stirring at ambient temperature for 16 hours. The reaction mixture was concentrated under reduced pressure to a total volume of approximately 20 mL and the polymer was purified by precipitation from cold ^{i}PrOH (-30 °C, 3 x 200 mL) and pentane (200 mL) with redissolution in DCM (20 mL). After drying at HV, PEG$_{114}$-DDMAT was obtained as a yellow solid. Dispersity was determined via SEC in DMAc (see Supporting Figure S18). Yield: 0.95 g (43% with respect to mPEG, $Đ_{SEC}$ = 1.10, degree of functionalization $d_f \approx$ 100 %).

Preparation of poly(ethylene glycol)-block-poly(styrene-alt-maleic anhydride) block copolymer (BCP1)[145]

A 50 mL round-bottom flask equipped with a stir bar was charged with mPEG$_{114}$-DDMAT (0.95 g, 177.0 µmol), maleic anhydride (3.48 g, 3.55 mmol, 200 eq.), styrene (3.70 g, 3.55 mmol, 200 eq.), AIBN (5.8 mg, 35 µmol, 0.2 eq., from 2 mg/mL stock solution in dioxane), dioxane (26 mL) and trioxane (80 mg as an internal standard for ^{1}H-NMR). The flask was sealed with a rubber septum and the reaction mixture was purged with N$_2$ for 30 min. Polymerization was initiated by immerging the flask in an oil-bath thermostated at 70 °C. The polymerization was monitored via ^{1}H-NMR spectroscopy (CD$_3$CN) of aliquots taken at regular intervals to determine monomer conversion from the decrease of the maleic anhydride (7.16 ppm) and styrene vinyl (5.29, 5.84, 6.80 ppm) signals relative to the trioxane signal (5.15 ppm), which showed equal conversion for the two monomers. The reaction mixture was removed after 180 min and polymerization was stopped by exposure to air and immediate precipitation of the polymer from a tenfold excess of diethyl ether. The polymer was purified by dissolution in dioxane (10 wt% polymer) and precipitation from a tenfold excess of diethyl ether/dioxane (9/1, v/v). After drying at HV, the polymer **BCP1** was obtained as a yellow solid. A degree of polymerization of 40 for the PSMA block was determined via ^{1}H-NMR spectroscopy (CD$_3$CN) from the ratio of the aromatic styrene signal to the PEG CH_2 signal, assuming a degree of polymerization of 114 for the PEG block (see Supporting Figure S17). The same values were also used to calculate number-average molecular weights. Dispersities $Đ$ were determined from SEC in DMAc.

BCP1: $Đ_{SEC}$ = 1.18, $M_{n,NMR}$ = 13450 gmol^{-1}.

Preparation of Diels-Alder product 3.

3a,b

R_a =

R_b =

To a solution of *N*-benzyl maleimide (**1**, 0.598 g, 3.19 mmol, 1.0 eq.) in DCM (5 mL), (*E/E*)-2,4-hexadiene acid ethyl ester (**2b**) or (*E/E*)-2,4-Hexadien-1-ol (**2a**), (15.97 mmol, 5.0 eq.) was added and stirred at room temperature for 18 h. After evaporation of the solvent, the raw product was purified using reversed-phase chromatography (linear gradient of acetonitrile, 40 to 98%, and water with 0.1% TFA). The combined fractions were lyophilized *in vacuo.* The purified product was used for its calibration on the HPLC as reference for the Diels-Alder kinetics.

Synthesis of peptide precursor acids

Peptide precursor acids were prepared on a 0.250 mmol scale using a *CEM Liberty* microwave-assisted peptide-synthesizer and the Liberty Blue Application Software (Copyright CEM Corporation 2015, Version: 1.45.5794.20265). We used the preloaded wang resin with Fmoc-D(O*t*Bu)-OH as the first coupling step. The resin is pre-swollen outside the synthesizer for 15 min. Ahead of the amino acid coupling, the *N*-terminal Fmoc-protecting group was removed by adding a 20% v/v solution of piperidine (2x20 mL) in DMF. After heating in the microwave (1 minute, 90°C), the mixture was washed with DMF (2x10 mL). Next, the coupling step was performed using 4.0 eq. of Fmoc-A-OH, Fmoc-V-OH, Fmoc-F-OH or Fmoc-I-OH in DMF (200 mM, 10 mL), 4 eq. of DIC (500 mM, 4 mL) and 4 eq. of oxyma (1000 mM, 2 mL). The mixture was subsequently heated in the microwave (2 minutes, 90°C). The Fmoc-deprotection, washing, and the washing cycle was performed for each amino acid coupling. The peptide was cleaved from the resin by adding a mixture of 95% TFA (9.5 mL), 2.5% deionized water (0.25 mL) and 2.5% TIPS (0.25 mL). Afterwards, the solvent was removed under reduced pressure. The peptides were then precipitated out using diethyl ether. The

crude product was isolated by centrifugation. The resulting peptides were dissolved in ±50% MeCN in H_2O and purified by high-reversed-liquid-chromatography (RP-HPLC) (40% to 98% gradient, 0.1% TFA in H_2O and MeCN). The collected fractions were freeze-dried and stored at -20°C.

Fluorescent labelled peptide synthesis (Fmoc-AAC(NBD)D-OH): The anchoring of the first amino acid Fmoc-D(O*t*Bu) to the hydroxylic group of a wang resin was performed by the activated symmetric anhydride route. A solution (0.2 M) was prepared by dissolution of Fmoc-D(O*t*Bu)-OH (12.0 mmol) and DIC (6.0 mmol) in DMF at room temperature. The DIU side product was precipitated by cooling down the reaction mixture at – 20 °C for 60 min and filtered out before being brought to contact with the resin. All subsequent couplings steps were performed with the microwave-assisted peptide synthesizer. As a first step, the symmetric anhydride solution was added to the pre-swollen wang resin (0.5 mmol) together with DMAP in catalytic amounts to drive the acetylation reaction. Afterwards, the *N*-Terminal Fmoc protecting group was cleaved with piperidine solution at 20% v/v in DMF (2 x 20 mL) and Fmoc-C(Mmt)-OH and Fmoc-A-OH were added in the same way as described before.

The orthogonal deprotection of the Mmt protecting group was performed by using a low percentage of TFA (2%) with TIPS in DCM (7 x 10 mL) stirred for 10 min. The deprotection progress could be followed by the yellow trityl cations formation. At the last wash step, the solution is then colourless. To prevent the formation of disulphide bond, ß-mercaptoethanol with NMM were added to the solution as oxidizing agent. Then, the NBD-Cl was coupled to the cysteine. NBD-Cl (2.0 eq., 1.0 mmol) was added and followed by DIEA (1.0 eq. 0.5 mmol). The reaction is stirred at room temperature for 2 h in aluminium foil to prevent photobleaching of the dye. The cleavage of the peptide from the resin and its purification followed the same protocol as described earlier.

Sample preparation

Blockcopolymer nanoreactor: We suspended 6.72 mg of **BCP1** anhydride (1 mM monomeric maleic anhydride units) in 20 mL of a 10 mM MES solution at pH 9. The reaction mixture was shaken for 3 days for the complete hydrolysis of the maleic anhydride moieties. The reaction mixture was freeze-dried. Next, we added 20 mL of a 10 mM MES solution at pH 6.0 to adjust the overall pH to pH 6.0 and distributed the solution in 5 mL aliquots. The aliquots were again freeze-dried and stored at -20 °C until further usage. We added 1 mL MQ water to each aliquot before an experiment. The addition of 1 mL MQ water results in 5 mM BCP1 concentration (with respect to the monomeric maleic acid units) in 100 mM MES at pH 6.0.

Supramolecular glue: We dissolved the peptide precursor acids in 200 mM MES buffer resulting in a 13.3 mM stock solution, and adjusted the pH to pH 6.0. A 2000 mM EDC stock

solution was always freshly prepared in MQ water, and the reaction cycle was started by adding EDC to the peptide precursor acid solution. A 1000 mM benzylamine stock solution in acetonitrile was prepared freshly ahead of the quenching experiment. All experiments were performed at 25 (±0.5) °C and stored at 8 and -20 °C.

Quantification of anhydride

Blockcopolymer nanoreactor: We prepared 200 µL of 5 mM BCP1 stock solution into a screw cap HPLC vial with micro insert and added the appropriate amount of fuel by the addition of a highly concentrated EDC stock in MQ water. Next, 20 µL samples were taken at the respective timepoints and quenched with 20 µL of a 40 mM BA stock solution in MQ water following a previously reported protocol. The BA reacts irreversibly with the anhydride groups and inhibits the reaction with remaining EDC. We quantified the BA concentration at different time points in the reaction cycle and calculated the anhydride concentration from the consumption of BA using the relation $c(anhydride) = c_0(BA) - c(BA)$.

Supramolecular glue: We prepared 75 µL of a 13.3 mM stock solution of the precursor acid into a screw cap HPLC vial with a micro insert and added the appropriate amount of fuel by adding 25 µL of a 2000 mM EDC stock in MQ water. The reaction cycle is then quenched at the respective time points with 100 µL of a 1000 mM BA stock solution in acetonitrile following a previously reported protocol. The BA reacts irreversibly with the anhydride groups and inhibits the reaction with the remaining EDC. The formed BA-peptide derivative was trackable by HPLC (220 nm). This derivative concentration is equal to the formed anhydride concentration.

Determination of solubilities of dienes

A saturated solution of diene **2** was prepared (diene/100 mM MES buffer, 1/4). After mixing and ultrasonication for 10 minutes, the solution was equilibrated. This was followed by centrifugation (13500 rounds per minute, 5 min). The upper phase was removed, and the buffer phase analyzed by HPLC. In case of diene **2b**, phase separation in aqueous buffer solution was noticed even after 3 days. Therefore, the solubility was determined in respect to the equilibrated value of **2b** after 3 days under consideration of its hydrolyzed fraction.

Diels-Alder reaction

We prepared 200 µL of a 5 mM stock solution of **BCP1** in a screw cap HPLC with micro inset. Next, the reaction cycle was started by the addition of a highly concentrated EDC stock solution as described above. The experiment was equilibrated for 10 min to form **BCP1** micelles. Afterwards, the Diels-Alder reaction was started by adding 0.4 µL of a 100 mM stock solution

of **1** and 2 µL of a 500 mM stock solution of **2**. We investigated the reaction kinetics via HPLC. Control experiments in 100 mM MES and 10 mM SDS were prepared as described above but without **BCP1**.

Quantification of migration rate

We quantified the migration rate using a classical method for wound healing scratch assays.[146, 147] Herein, we damaged our fiber network using a 200 µm thin needle that was attached to a manipulator set-up (ESI, Fig. 3†). The scratch was performed on a 10 µL volumed hydrogel (10 mM Fmoc-AAD-OH fueled with 500 mM EDC, stained with 2.5 µM Nile Red), preformed in an incubation chamber (ibidi) suitable for imaging by confocal fluorescence spectroscopy without drying effects. The scratch was performed at the respective time by inserting the needle in 45° to the hydrogel layer and subsequently instructing the manipulator to perform the scratch. The healing process was immediately monitored in x/y/z dimension (184 µm x 184µm with a z-stack of around 20 µm) over the migration time of 25 min. The analysis of the migration rate took place around 15 µm above the glass slide surface. Each scratch was performed in triplicate. We analyzed the scratch width collapse based on the manual distance measured by the software *ImageJ.* Herein, we took a width of the fibers front orthogonal to the scratch and compared the initial width at t = 0 minute to the one at t = 25 minutes. For each scratch, a triplicate of widths was analyzed over the whole scratch size (each width being in a distance of roughly 40 µm from each other). The healing in % was determined as follows:

$$Healing\ (\%) = \left(1 - \frac{W_t}{W_{t=0}}\right) \times 100 \tag{1}$$

The migration rate was determined by applying equation 2:

$$r_m = \frac{W_{t=0} - W_{t=25}}{t_{migrat.}} \tag{2}$$

Where r_m is the migration rate, W the width at different times t and t_{migrat} the time over which the network migration was studied (25 minutes).

Quantification of peptide precursor in solution and co-assembly ratio

The amount of peptide precursor in solution and the co-assembly ratio of peptide precursor to anhydride product was investigated over time using [1]H-Nuclear Resonance Spectroscopy (NMR) and analytical High-Performance Liquid Chromatography (HPLC). ^{1}H-NMR spectroscopy was used to determine the free peptide precursor concentration in solution and

the ratio of co-assembly of peptide precursor and product. We used an inner tube filled with an internal hydroquinone standard (50 mM dissolved in D_2O) and recorded the spectra according to water suppression. Herein, we compared the integral of the Fmoc-protons at 7.20 – 7.50 ppm to the integral of the hydroquinone standard at 6.70 ppm to determine the free peptide precursor concentration in the solution. We confirmed the co-assembly ratio by assuming that self-assembled molecules do not show NMR-activity and remain silent, in contrast to non-assembled ones that are visible.

In combination with the anhydride concentration that we obtained by HPLC, the peptide concentration in solution and the peptide precursor concentration was received as follows:

$$[peptide]_{sol.} = [peptide\ precursor]_{t=0.} - [peptide]_{ass.} \tag{3}$$

The amount of peptide precursor co-assembling in the fiber network was obtained according to:

$$[peptide\ precursor]_{ass.} = [peptide]_{ass.} - [product] \tag{4}$$

Where $[peptide]_{sol.}$ represents the concentration of peptide in solution, $[peptide\ precursor]_{t=0}$ the initial peptide precursor concentration, $[peptide]_{ass.}$ the concentration of peptide in the fiber assemblies, $[peptide\ precursor]_{ass.}$ the peptide precursor concentration in the fiber assemblies and $[product]$ the concentration of anhydride product analyzed by HPLC. Using the so obtained peptide concentration in solution and our kinetic model, we could define the amount of anhydride product in solution that we define as molecular glue concentration.

Spatial organization of Fmoc-AAC(NBD)D-OH

By confocal microscopy, we analyzed the spatial incorporation of the NBD-labeled peptide at the damaged network front. As a negative control (undamaged), we prepared 10 mM Fmoc-AAD-OH with 500 mM EDC (stained with 0.1 µM Nile Red) in the incubation chamber topped with 1 µL of a mixture (10:1 ratio) of Fmoc-AAD-OH and Fmoc-AAC(NBD)D-OH. We used an excitation at 488 nm for the NBD-labeled peptide and 552 nm for the Nile Red stained one. The gel was screened in x/y/z-dimension for 40 minutes.

Next, the damaged experiment was approached by preparing another Fmoc-AAD-OH gel in a vial topped with 1 µL of a mixture (10:1 ratio) of Fmoc-AAD-OH and Fmoc-AAC(NBD)D-OH. After 13 minutes the gel was ultrasonicated for 2 minutes, immediately transferred to the incubation chamber and screened as stated above.

Finally, the Fmoc-AAD-OH gel was prepared in the incubation chamber and scratched 13 minutes after fuel addition. The applied needle was topped with 1 µL of a mixture (10:1 ratio) of Fmoc-AAD-OH and Fmoc-AAC(NBD)D-OH, creating the direct contact of fiber damage sites and the NBD tagged peptide. All experiments were performed in triplicate.

Quantification of amounts of end caps per fiber

The change in the number of end caps per fiber upon damage of the fiber network was determined using cryo-Transmission Electron Microscopy (TEM). Due to the gel's strength, we decreased the fuel concentration to 10 mM by adding 25 µL of a 40 mM EDC stock solution to a 75 µL peptide precursor acid stock solution of 13.3 mM in a 2 mL vial. The damaged sample was destroyed by ultrasonication of the sample for 20 seconds at t = 1 minute and immediately pipetted onto the prepared grid in the Vitrobot. The same sample was then pipetted on a second grid after 25 minutes to compare for the recovery of destroyed fibers. As a control, an undamaged sample with the same conditions was prepared for the same timepoints without ultrasonicating it. Per condition, six micrographs were used to determine the average end cap per fiver ratio. All experiments were performed in triplicate.

High performance liquid chromatography (HPLC)

Blockcopolymer nanoreactor: We monitored the kinetics of the reaction cycle and Diels-Alder reaction by analytical HPLC (*ThermoFisher* Vanquish Duo UHPLC) with a Hypersil Gold 100 x 2.1 mm C18 column (3 µm pore size). We prepared 200 µL of the reaction mixture into a screw cap HPLC vial with micro inset following the sample preparation protocol described above. All samples were directly injected without any further dilution from the HPLC vial. We injected 1 µL for the detection of BA, 0.1 µL for the detection of EDC and 3 µL for the detection of **1**, **2a** and **2b** and the respective Diels-Alder products **3a** and **3b**. We used a UV/Vis detector at 254 nm for the quantification of BA, **2a** and **3a** and 220 nm for the quantification of all other reagents. Calibration curves for the EDC (in MQ water), benzylamine (in MQ water), **1** (in MES buffer), **2a** (in ACN), **2b** (in ACN) and Diels-Alder products **3a** and **3b** (in ACN) were performed with the corresponding methods in triplicate. Retention times and calibration values are given in Supporting Table S1, S4 and S5. We used the following methods for the separation of the compounds:

HPLC method 1: H_2O: ACN from 95:5 to 75:25 in 3 min, from 75:25 to 2:98 in 0.5 min, 2:98 from 3.5 min to 6 min, from 2:98 to 95:5 in 0.5 min, 95:5 from 6.5 min to 10 min.

HPLC method 2: H_2O: ACN from 95:5 to 2:98 in 5 min, 2:98 from 5 min to 6.5 min, from 2:98 to 95:5 in 0.5 min, 95:5 from 7 min to 10 min.

HPLC method 3: H_2O: ACN from 60:40 to 2:98 in 5 min, 2:98 from 5 min to 6.5 min, from 2:98 to 60:40 in 0.5 min, 60:40 from 7 min to 10 min.

Supramolecular glue: We monitored the kinetics of the reaction cycle by analytical HPLC (*ThermoFisher* Vanquish Duo UHPLC) with a Hypersil Gold 100 x 2.1 mm C18 column (3 µm pore size). We prepared 200 µL of the reaction mixture into a screw cap HPLC vial with micro inset following the sample preparation protocol described above. All samples were directly injected without any further dilution from the HPLC vial. We injected 2 µL for the detection of EDC, BA and for the detection of the peptide precursor acids. We used a UV/Vis detector at 220 nm and 254 nm for the quantification of all reagents. Calibration curves for the EDC (in MQ water), BA (in acetonitrile), peptide precursor acids (in MES buffer) were performed with the corresponding method in triplicate. Retention times and calibration values are given in ESI Table 1†. We used the following method for the separation of the compounds:

HPLC method: H_2O: ACN from 98:2 to 2:98 in 12 minutes, 2:98 for 1 minute, 2:98 to 98:2 in 1 minute and 98:2 for 1 minute resulting in a 15 minute long method.

HPLC: R_t (Fmoc-AAD-OH) = 9.7 min. (see ESI, Fig. 15†)

HPLC: R_t (Fmoc-AVD-OH) = 11.1 min. (see ESI, Fig. 16†)

HPLC: R_t (ac-FIID-OH) = 8.9 min. (see ESI, Fig. 17†)

HPLC: R_t (Fmoc-AAC(NBD)D-OH) = 11.7 min. (see ESI, Fig. 18†)

Reversed-phase high-performance liquid chromatography (RP-HPLC)

Blockcopolymer nanoreactor: The Diels-Alder raw products **3a** and **3b** were purified on reversed-phase HPLC (*Thermofisher*, Hypersil Gold 250 x 20mm, 5 µm pore size, C18 column) with a linear gradient of acetonitrile (ACN, 40 to 98%) and water with 0.1% trifluoroacetic acid.

Supramolecular glue: The peptide precursor acids were purified on reversed-phase HPLC (*Thermofisher*, Hypersil Gold 250 x 20mm, 5 µm pore size, C18 column) with a linear gradient of acetonitrile (ACN, 40 to 98%) and water with 0.1% trifluoroacetic acid. UV-Vis detection was conducted using 220 and 254 nm.

Size-exclusion chromatography (SEC)

SEC was performed using an *Agilent* 1200 system equipped with a 1260 series isocratic pump and a refractive index detector. The stationary phase consisted of a pre-column and three GRAM gel columns (8 x 300 mm, *Polymer Standard Services*) with pore sizes of 30, 1000, and 1000 Å, respectively. Chromatography was performed at 50°C at a flowrate of 1 mLmin^{-1} DMAc

+ 0.5 wt% LiBr. Narrowly distributed poly(methyl methacrylate) standards were used for calibration (*Polymer Standard Services*). Samples were prepared at polymer concentrations of 1.0 gL^{-1}.

Kinetic model

We used a *Matlab* kinetic model for the calculation of the concentrations of reactants. For a detailed explanation, please see the Supporting Information in the ESIs of the discussed publications.

Time-lapse photography

Blockcopolymer nanoreactor: In a 2 mL HPLC vial, 500 µL of the polymer precursor solution fueled with or without EDC were imaged with a high-definition camera. Time-lapse software was programed to image the sample in a 5 min interval. The investigation of the **BCP1**'s foaminess was performed by vortexing the solution for 1 min prior to the time-lapse video.

Supramolecular glue: The vial inversion experiment was performed in a 2 mL HPLC vial and imaged with a high-definition camera. Time-lapse software was programmed to image the sample in a 30-second interval. We started the hydrogel formation by adding 125 µL of a 2000 mM EDC stock solution to 375 µL of 13.3 mM peptide precursor acid solution (pH 6, 200 mM MES). At the respective time, the hydrogel was destroyed using a vortex mixer for 20 seconds resulting in the liquification of the gel. After giving the gel time to relax for 5 minutes, the vial was inverted and imaged to demonstrate the gel's ability to self-heal. All experiments were performed in triplicate.

Self-healing measure by rheology

We studied the gelation behavior of the peptide assemblies using a commercial shear rheometer (MCR 302, *Anton Paar*, Graz, Austria) and a plate-plate geometry (bottom plate: P-PTD200/80-I, *Anton Paar*, equipped with a Ø55 mm polystyrene petri-dish (VWR, Radnor, USA); Ø 25 mm steel measuring head: PP25, 79044, Anton Paar). For each measurement, the required sample volume was 180 µL as the plate separation was set to 0.3 mm. A solvent trap (a chamber containing a water-soaked sponge, covered with a lid) as well as a temperature control of the bottom plate (set to 21°C) was employed for all measurements. All measurements were recorded in triplicate.

We obtained the initial gelation morphology by adding 50 µL of a 2000 mM EDC stock solution to a 150 µL of a 13.3 mM peptide precursor acid in the rheometer. To ensure linear material response during the gelation process of the samples, the measurements were performed in torque-controlled mode (by applying small torques of 0.5 µNm and a constant oscillation

frequency of 1 Hz). The storage and loss moduli were determined for 5 minutes, and one measurement point was recorded every 7.5 seconds. To determine the self-healing behavior of the peptides, the samples were prepared in a vial using the conditions stated above. At the respective time intervals, the gel was destroyed by a vortex mixer (20 seconds) and immediately transferred to the rheometer plate. The rheological measurement was conducted as described above to test for the mechanical recovery abilities of the sample over time.

Confocal fluorescence microscopy

We imaged the behavior of the fiber assemblies on a microscopic level using a Leica DMi8 microscope, including a 63x water immersion objective. We prepared the hydrogels of a total reaction volume of 10 μL directly in incubation chambers (ibidi chamber). The assemblies were stained with 2.5 μM Nile Red. Samples were excited at 552 nm (488 nm in the case of Fmoc-AAC(NBD)-OH) and imaged at 577-650 nm.

Interfacial surface tension (IFT)

The interfacial surface tension between the aqueous **BCP1** system and air was determined using the video-based optical contact angle measuring system *OCA 25* (*Dataphysics*), using the software *SCA-22* pendant drop right. 1 mL *Braun* disposable syringes and a regular needle of 0.8 mm radii were used. The measurements occurred at the stated time points and were repeated 10 times.

Fluorescence spectroscopy

Blockcopolymer nanoreactor: Nile Red assay studies were performed on a Jasco FP-8300 fluorescence spectrophotometer with an external temperature control (*Jasco MCB-100*). The samples were directly prepared in a 10 mm quartz cuvette from *Precision Cells Inc.* by mixing 5 mM **BCP1** solution with 5 mM EDC and 2.5 μM Nile Red. The fluorescence intensities were measured over time, each minute, at 635 nm with an excitation at 550 nm. The normalized values were obtained by division through the blank prebleached fluorescence intensity values. *Supramolecular glue:* Nile Red assay studies were performed on a *Jasco FP-8300* fluorescence spectrophotometer with external temperature control (*Jasco MCB-100*). The fluorescence intensities were measured over time, each minute, at 635 nm with an excitation at 488 nm. The Fmoc-AAC(NBD)D-OH incorporation experiment was performed by preparing a hydrogel (135 μL of a 13.3 mM Fmoc-AAD-OH solution fueled with 45 μL of a 2000 mM EDC solution) in a vial. After 13 minutes, the gel was damaged (vortex mixed or ultrasonicated for 20 seconds) and pipetted to a 10 mm quartz cuvette from *Precision Cells Inc.* On top of the damaged gel, 20 μL of a 10:1 mixture of Fmoc-AAD-OH to Fmoc-AAC(NBD)D-OH was added.

The increase in fluorescence intensity was observed over time. All experiments were performed in triplicate.

Dynamic light scattering (DLS)

Blockcopolymer nanoreactor: The scattering behavior of the micellar assemblies was detected on a *Malvern Zetasizer Nano ZS* using a laser wavelength of 633 nm in disposable cuvettes (PS). The measurement for 5 mM **BCP1** solution with and without 5 mM EDC were performed using 5 acquisition times of 20 s.

Supramolecular glue: The critical aggregation concentration (CAC) was determined on a *Malvern Zetasizer Nano ZS* using a laser wavelength of 633 nm and disposable cuvettes (PS), setting the method of 5 acquisition times of 20 seconds per measurement. A series of low peptide precursor acid concentration was fueled with 500 mM EDC (375 µL of x mM peptide precursor acid solution fueled with 125 µL of a 2000 mM EDC solution, prepared directly in the cuvette) to observe a significant increase in the scattering rate. All measurements were performed in triplicates.

Cryogenic-transmission electron microscopy (cryo-TEM)

Blockcopolymer nanoreactor: Samples for TEM measurement were prepared as stated above. The grids (Quantifoil R2/2 on Cu-grid 400 mesh) were freshly glow-discharged for 30 s before use. Preparation of the grids was performed in an *FEI/Thermo Fisher* Vitrobot at 25 °C with the relative humidity set to 100%. **BCP1** (5 µL) was incubated for 30 s, blotted twice for 3.5 s with a blotting force set to -5. This was followed by plunging of the sample into liquid ethane (pre-cooled by liquid nitrogen). For the measurement and unless not stored in liquid nitrogen, the cryo-TEM grids were transferred into a *Gatan* cryo-transfer specimen holder to insert into the microscope. A temperature of -170 °C of the holder was ensured during the measurement. Cryo-TEM pictures were obtained using a *Jeol JEM-1400 plus* operating at 120 kV and were recorded in a low-dose mode using a CCD camera.

Supramolecular glue: We freshly prepared samples of a 50 µL reaction volume for Cryo-TEM. Cryo-TEM imaging was operated on a Tecnai Spirit microscope (FEI/*Thermo Fisher*) at 120 kV. Herein, the images were recorded in a low-dose mode on a CCD camera. The samples were prepared on Cu-grids (C-flat, 2.0 µm hole size, 2.0 µm hole spacing, 400 mesh) that were freshly glow discharged for 90 seconds at 45 mA and $3 \cdot 10^{-2}$ mbar before use. Samples were prepared as described before. 5 µL of the sample was pipetted on to the Cu-grids in a FEI/Thermo Fisher Vitrobot set to 22°C and a relative humidity of 100%. The blotting conditions were set to a waiting time of 30 seconds, a blot time of 2.5 seconds and a blot force of -1. Thereafter, grids are plunged into liquid ethane (pre-cooled by liquid nitrogen). The cryo-TEM

grids were transferred and stored in liquid nitrogen until they were placed into a Gatan cryo-transfer-specimen holder for imaging. The specimen temperature was maintained at -170 °C during the whole process. All experiments were performed in triplicate.

Nuclear resonance spectroscopy (NMR)

Blockcopolymer nanoreactor: NMR spectra were recorded on *a Bruker AVIII-300*, *Bruker ARX 300* and *AVIII-500-cryo* spectrometer by *Bruker Analytik* at 25 °C and a frequency of 300/300/500 MHz, respectively. Chemical shifts δ are reported in ppm and are referred to the residual solvent peak of the used deuterated solvent (in case of chloroform-d_1 7.26 ppm (^{1}H) and 77.2 ppm (^{13}C), acetonitrile-d_3 1.94 ppm (^{1}H)). The abbreviation of the signal multiplets are as followed: s-singulet, d-dublet, t-triplet, m-multiplet. The coupling constant J is stated as average value in Hz and refers to coupling between two protons. The degree of polymerization refers to the amount of monomer units found comparing the ratio of the styrene (Aryl-H) and PEG (CH$_2$) signal in the ^{1}H-NMR spectrum. *Endo/exo* diastereomer distinguishment as well as *endo/exo*-ratio was determined referring to the *J*-coupling and the integration of the CH-group at 2.56 ppm.

Supramolecular glue: NMR spectra were recorded on *a Bruker AVIII-300*, *Bruker ARX 300* and *AVIII-500-cryo* spectrometer by *Bruker Analytik* at 25 °C and a frequency of 300/300/500 MHz, respectively. Chemical shifts δ are reported in ppm and are referred to the residual solvent peak of the used deuterated solvent (D$_2$O (4.79 (^{1}H)) and dmso-D$_6$ (2.50 (^{1}H)) and 39.5 ppm (^{13}C)). The abbreviation of the signal multiplets are stated as followed: s-singulet, d-dublet, t-triplet, q-quartet, m-multiplet. The coupling constant J referred to the average value in Hz and the coupling between two protons. The analysis of all received spectra was performed using *MestReNova*© software (Version 11.0.0.-17609).

Electrospray ionization mass spectrometry (ESI-MS)

The ESI-MS spectrum was recorded on a *Thermo Scientific LGC Fleet* spectrometer by *Thermo Fischer Scientific*. The analysis of mass was carried out with the *time-of-flight* method.

UV-Vis spectroscopy

On a Multiskan FC microplate reader (*Thermofisher*), UV-Vis measurements were performed using a 96-well plate (tissue culture plate, non-treated) at 600 nm and 25°C. All experiments were performed in triplicates.

9 Further publications

I also contributed to other publications besides the two publications reprinted above. A list of all my publications is given below.

Publications

[1]   M. A. Würbser,* P. S. Schwarz,* J. Heckel, A. M. Bergmann, A. Walther, J. Boekhoven, *ChemSystemsChem* **2021**, *3*, e2100015.

[2]   J. Rodon-Fores,* M. A. Würbser,* M. Kretschmer, B. Rieß, A. M. Bergmann, O. Lieleg, J. Boekhoven, *Chem. Sci.* **2022**, *13*, 11411-11421.

[3]   M. Kretschmer, E. N. Hayta, M. J. Ertelt, M. A. Würbser, J. Boekhoven, O. Lieleg, *Biotechnol. Bioeng.* **2022,** *119*, 895-906.

[4]   X. Chen,* M. A. Würbser,* J. Boekhoven, *Acc. Mater. Res.* **2023**, accepted.

*These authors contributed equally.

10 Acknowledgments

I sincerely thank you, Job, for taking me in and giving me the opportunity to complete my Ph.D. in your lab. Throughout the years, I can certainly say that I developed and learned many things, on a scientific level (due to multiple sub-group meetings, group meetings, or journal clubs), but also interpersonally by working in your team. Though the number of meetings we had was almost overwhelming sometimes, the key message to me will remain for a long time, that communication and persistent work is gold. Thank you for taking your time during our meetings and writing sessions and guiding the paper writing process with your expertise and experience, I appreciate it.

Furthermore, I am really grateful to my collaboration partners, doing a great contribution to successfully finishing up our projects: Prof. Oliver Lieleg, Dr. Martin Kretschmer, Jonas Heckel, Prof. Andreas Walther, Dr. Patrick Schwarz, Dr. Jennifer Rodon-Fores, Xiaoyao Chen and Alexander Bergmann. Padi, thank you for being the calm and relaxed counterpart for the nano-reactor paper, I could hang on till the end mostly because of that. Jenny, working with you for almost two years on our healing gel, we had a lot of ups and downs to face. But I truly enjoyed it and learned a lot from you, many thanks. I know for sure that wherever you go and which career path you embark, it will be a success. Xiaoyao, I know it has been a crazy time during which we wrote the review, but thank you for hanging on and making it easy and uncomplicated to work with you. And Alex, I guess everyone will thank you a lot for taking all cryo-TEM pictures and doing the needed experiments. Thank you, I know, it was time-consuming and, at some parts, not easy. You did a great job.

Thank you, to all my lab mates throughout the years: Caren, Martha, Rapha, Benno, Schnitti, Padi, Carsten, Kun, Alex, Laura, Jenny, Savannah, Xiaoyao, Judit, Michele, Spabi, Brigitte, Christine, Anna-Lena, Moni, Simone, Oleksii, and Pablo. Thank you, Jennifer, Ruth and Corinna, for handling administrative things. Guys, I especially enjoyed our lunchbreaks, eating wraps or ice cream, chit-chatting, watching cooking videos, having hotpot, playing with Savannah. I really missed that in the last years. But also thank you for helping me out in lab or with scientific questions.

And now, my beloved friends and family.

Meine liebe Juli, dass aus einem recht zufälligen Nebeneinandersitzen in der 7. Klasse eine so schöne und enge Freundschaft wird, hätte ich kaum gedacht. Ich bin so dankbar, dass du da bist. Auf viel gutes, gemeinsames Essen und Lachen.

Zuletzt danke ich besonders meiner lieben Familie. Das Maß an Stress, gelegentliches überfordert sein, und die Teufelsspirale aus bodenlosem Hunger und dadurch wiederum unerträglich sein, ihr habt es ertragen und seid einfach da gewesen. Papa, ohne dein hervorragendes

Essen, wo wäre deine Stressamsel wohl heute. Danke Chrisi, dass du mir immer dein Ohr geliehen hast. Und Mamilein, ich danke dir unendlich für deinen Einsatz (wie z.B. in Form von unzähligen Kuchenstücken vom Tullio), deine Hingabe (den Hugendubel leer zu kaufen), deine bedingungslose Liebe (u. A. in Form von etlichen Bussis). Du bist wunderbar.

Und Padi. Ich bin so froh, dass wir uns während des Studiums kennenlernen durften. Du hast mich so erlebt und vor allem akzeptiert, wie ich bin, und warst zu allen Zeiten, besonders den sehr schweren, einfach da. Dafür werde ich dir immer zutiefst dankbar sein, ich liebe dich.

11 References

1. A. Priimägi and S. Hecht, *Adv. Mater.*, 2020, **32**.
2. E. Reyssat and L. Mahadevan, *J. R. Soc. Interface*, 2009, **6**, 951-957.
3. R. Elbaum, L. Zaltzman, I. Burgert and P. Fratzl, *Science*, 2007, **316**, 884-886.
4. Y. Forterre, J. M. Skotheim, J. Dumais and L. Mahadevan, *Nature*, 2005, **433**, 421-425.
5. A. Walther, *Adv. Mater.*, 2020, **32**, 1905111.
6. H. Lee, C. Xia and N. X. Fang, *Soft Matter*, 2010, **6**, 4342-4345.
7. S. Timoshenko, *Josa*, 1925, **11**, 233-255.
8. A. Pavlovič, L. u. Slováková, C. Pandolfi and S. Mancuso, *J. Exp. Bot.*, 2011, **62**, 1991-2000.
9. S. Poppinga and M. Joyeux, *Phys. Rev. E*, 2011, **84**, 041928.
10. A. Volkov and R. Haack, *Bioelectrochem. Bioenerg.*, 1995, **37**, 55-60.
11. A. G. Volkov, H. Carrell, A. Baldwin and V. S. Markin, *Bioelectrochemistry*, 2009, **75**, 142-147.
12. A. G. Volkov, T. Adesina, V. S. Markin and E. Jovanov, *Plant Physiol.*, 2008, **146**, 694.
13. B. J. Haas and J. L. Whited, *Trends Genet.*, 2017, **33**, 553-565.
14. J. Boekhoven and S. I. Stupp, *Adv. Mater.*, 2014, **26**, 1642-1659.
15. J. L. Whited and C. J. Tabin, *J. Biol.*, 2009, **8**, 1-4.
16. M. Kragl, D. Knapp, E. Nacu, S. Khattak, M. Maden, H. H. Epperlein and E. M. Tanaka, *Nature*, 2009, **460**, 60-65.
17. R. N. Christensen and R. A. Tassava, *Dev. Dyn.*, 2000, **217**, 216-224.
18. L. J. Campbell and C. M. Crews, *Cell. Mol. Life Sci.*, 2007, **65**, 73.
19. D. L. Stocum, *Differ.*, 1984, **27**, 13-28.
20. S. Calve, S. J. Odelberg and H.-G. Simon, *Dev. Biol.*, 2010, **344**, 259-271.
21. C. S. Pittendrigh, 1960.
22. D. A. Paranjpe and V. Kumar Sharma, *J. Circadian Rhythms*, 2005, **3**, 7.
23. H. Okamura, S. Yamaguchi and K. Yagita, *Cell Tissue Res.*, 2002, **309**, 47-56.
24. A. Sehgal, *Cell*, 2017, **171**, 1232-1235.
25. R. Merindol and A. Walther, *Chem. Soc. Rev.*, 2017, **46**, 5588-5619.
26. C. S. Pittendrigh, *Proc. Natl. Acad. Sci.*, 1954, **40**, 1018-1029.
27. H. Kalmus, *Biol. Gen.*, 1935, **11**, 93-114.
28. P. J. DeCoursey, 2004.
29. T.-H. Kang, J. T. Reardon, M. Kemp and A. Sancar, *Proc. Natl. Acad. Sci.*, 2009, **106**, 2864-2867.
30. C. H. Ko and J. S. Takahashi, *Hum. Mol. Genet.*, 2006, **15**, R271-R277.
31. J. C. Dunlap, *Cell*, 1999, **96**, 271-290.
32. R. Stanewsky, *J. Neurobiol.*, 2003, **54**, 111-147.
33. N. R. Glossop, J. H. Houl, H. Zheng, F. S. Ng, S. M. Dudek and P. E. Hardin, *Neuron*, 2003, **37**, 249-261.
34. T.-H. Kang, L. A. Lindsey-Boltz, J. T. Reardon and A. Sancar, *Proc. Natl. Acad. Sci.*, 2010, **107**, 4890-4895.
35. C. L. Partch, C. B. Green and J. S. Takahashi, *Trends Cell Biol.*, 2014, **24**, 90-99.
36. S. Zhang, *Biotechnol. Adv.*, 2002, **20**, 321-339.
37. J. L. Atwood and J. W. Steed, *Supramolecular chemistry*, John Wiley & Sons, 2009.
38. G. M. Whitesides, J. P. Mathias and C. T. Seto, *Science*, 1991, **254**, 1312-1319.
39. J.-M. Lehn, *Science*, 1993, **260**, 1762-1763.
40. D. Fujita, Y. Ueda, S. Sato, N. Mizuno, T. Kumasaka and M. Fujita, *Nature*, 2016, **540**, 563-566.
41. B. Wei, M. Dai and P. Yin, *Nature*, 2012, **485**, 623-626.
42. E. Schrodinger, *Journal*, 1942.
43. K. R. Dronamraju, *Genetics*, 1999, **153**, 1071-1076.
44. T. L. Hill, *Free Energy Transduction and Biochemical Cycle Kinetics*, Dover Publications, 2005.
45. M. Weißenfels, J. Gemen and R. Klajn, *Chem*, 2021, **7**, 23-37.

46. G. Ragazzon and L. J. Prins, *Nat. Nanotechnol.*, 2018, **13**, 882-889.
47. D. Del Giudice, F. Frateloreto, C. Sappino and S. Di Stefano, *Eur. J. Org. Chem.*, 2022, **2022**.
48. S. A. van Rossum, M. Tena-Solsona, J. H. van Esch, R. Eelkema and J. Boekhoven, *Chem. Soc. Rev.*, 2017, **46**, 5519-5535.
49. H. Liu, Y. Xu, F. Li, Y. Yang, W. Wang, Y. Song and D. Liu, *Angew. Chem. Int. Ed.*, 2007, **46**, 2515-2517.
50. R. Klajn, K. J. M. Bishop and B. A. Grzybowski, *Proc. Natl. Acad. Sci.*, 2007, **104**, 10305-10309.
51. R. Klajn, P. J. Wesson, K. J. M. Bishop and B. A. Grzybowski, *Angew. Chem. Int. Ed.*, 2009, **48**, 7035-7039.
52. P. S. Schwarz, M. Tena-Solsona, K. Dai and J. Boekhoven, *Chem. Commun.*, 2022, **58**, 1284-1297.
53. H. Hulett, *Nature*, 1970, **225**, 1248-1249.
54. A. Sorrenti, J. Leira-Iglesias, A. Sato and T. M. Hermans, *Nat. Commun.*, 2017, **8**, 1-8.
55. S. Maiti, I. Fortunati, C. Ferrante, P. Scrimin and L. J. Prins, *Nat. Chem.*, 2016, **8**, 725-731.
56. L. Heinen and A. Walther, *Sci. Adv.*, 2019, **5**, eaaw0590.
57. B. Fan, Y. Men, S. A. van Rossum, G. Li and R. Eelkema, *ChemSystemsChem*, 2020, **2**, e1900028.
58. S. Yang, G. Schaeffer, E. Mattia, O. Markovitch, K. Liu, A. S. Hussain, J. Ottelé, A. Sood and S. Otto, *Angew. Chem. Int. Ed.*, 2021, **60**, 11344-11349.
59. S. Debnath, S. Roy and R. V. Ulijn, *J. Am. Chem. Soc.*, 2013, **135**, 16789-16792.
60. J. McIntosh, *Mod. Cell Biol.*, 1983, **2**, 115-142.
61. L. Schaedel, K. John, J. Gaillard, M. V. Nachury, L. Blanchoin and M. Théry, *Nat. Mater.*, 2015, **14**, 1156-1163.
62. D. A. Fletcher and R. D. Mullins, *Nature*, 2010, **463**, 485-492.
63. E. Kliuchnikov, E. Klyshko, M. S. Kelly, A. Zhmurov, R. I. Dima, K. A. Marx and V. Barsegov, *Comput. Struct. Biotechnol. J*, 2022, **20**, 953-974.
64. B. L. Goode, D. G. Drubin and G. Barnes, *Curr. Opin. Cell. Biol.*, 2000, **12**, 63-71.
65. T. Mitchison and M. Kirschner, *nature*, 1984, **312**, 237-242.
66. B. M. Mulder and M. E. Janson, *Nat. Mater.*, 2015, **14**, 1080-1081.
67. H. P. Erickson and E. T. O'Brien, *Annu. Rev. Biophys. Biomol. Struct.*, 1992, **21**, 145-166.
68. S. Inoué and E. D. Salmon, *Mol. Biol. Cell*, 1995, **6**, 1619-1640.
69. T. David-Pfeuty, H. P. Erickson and D. Pantaloni, *Proc. Natl. Acad. Sci.*, 1977, **74**, 5372-5376.
70. H. Bowne-Anderson, M. Zanic, M. Kauer and J. Howard, *BioEssays*, 2013, **35**, 452-461.
71. T. C. Michaels, S. Feng, H. Liang and L. Mahadevan, *Elife*, 2020, **9**.
72. J. Boekhoven, W. E. Hendriksen, G. J. M. Koper, R. Eelkema and J. H. van Esch, *Science*, 2015, **349**, 1075-1079.
73. T. Heuser, E. Weyandt and A. Walther, *Angew. Chem.*, 2015, **127**, 13456-13460.
74. J. Boekhoven, A. M. Brizard, K. N. K. Kowlgi, G. J. M. Koper, R. Eelkema and J. H. Van Esch, *Angew. Chem.*, 2010, **122**, 4935-4938.
75. M. Tena-Solsona, B. Rieß, R. K. Grötsch, F. C. Löhrer, C. Wanzke, B. Käsdorf, A. R. Bausch, P. Müller-Buschbaum, O. Lieleg and J. Boekhoven, *Nat. Commun.*, 2017, **8**, 15895.
76. M. A. Gilles, A. Q. Hudson and C. Borders Jr, *Anal. Biochem.*, 1990, **184**, 244-248.
77. J. S. Moore and S. I. Stupp, *Macromolecules*, 1990, **23**, 65-70.
78. B. Rieß, C. Wanzke, M. Tena-Solsona, R. K. Grötsch, C. Maity and J. Boekhoven, *Soft Matter*, 2018, **14**, 4852-4859.
79. C. Wanzke, M. Tena-Solsona, B. Rieß, L. Tebcharani and J. Boekhoven, *Mater. Horiz.*, 2020, **7**, 1397-1403.
80. B. Zhang, I. M. Jayalath, J. Ke, J. L. Sparks, C. S. Hartley and D. Konkolewicz, *Chem. Commun.*, 2019, **55**, 2086-2089.
81. M. D. Hager, P. Greil, C. Leyens, S. van der Zwaag and U. S. Schubert, *Adv. Mater.*, 2010, **22**, 5424-5430.
82. R. P. Wool, *Soft Matter*, 2008, **4**, 400-418.
83. Y. J. Tan, G. J. Susanto, H. P. Anwar Ali and B. C. Tee, *Adv. Mater.*, 2021, **33**, 2002800.

84. S. Palagi and P. Fischer, *Nat. Rev. Mater.*, 2018, **3**, 113-124.
85. M. D. Jackson, S. R. Mulcahy, H. Chen, Y. Li, Q. Li, P. Cappelletti and H.-R. Wenk, *Am. Mineral.*, 2017, **102**, 1435-1450.
86. F. B. Silva, N. Boon, N. D. Belie and W. Verstraete, *J. Commer. Biotechnol.*, 2015, **21**.
87. G. Cheeseman and B. Lawn, *Phys. Status Solidi*, 1970, **3**, 951-958.
88. S. Wiederhorn and P. Townsend, *J. Am. Ceram. Soc.*, 1970, **53**, 486-489.
89. B. Grabowski and C. C. Tasan, *Self-healing materials*, 2016, 387-407.
90. T. Broom, J. Molineux and V. Whittaker, *J. Inset. Met.*, 1956, **84**, 357-363.
91. N. van Dijk and S. van der Zwaag, *Adv. Mater. Interfaces*, 2018, **5**, 1800226.
92. S. Voyutskii and V. Vakula, *J. Appl. Polym. Sci.*, 1963, **7**, 475-491.
93. J. O. Outwater and D. J. Gerry, *J. Adhes.*, 1969, **1**, 290-298.
94. R. Wool, R. Bretzlaff, B. Li, C. Wang and R. Boyd, *J. Polym. Sci., Part B: Polym. Phys.*, 1986, **24**, 1039-1066.
95. L.-H. Lee, *Adhesion and adsorption of polymers*, Springer Science & Business Media, 2012.
96. R. A. Fall, Virginia Tech, 2001.
97. S. J. Kalista, J. R. Pflug and R. J. Varley, *Polym. Chem.*, 2013, **4**, 4910-4926.
98. R. Fall, T. Ward, J. Dillard, T. S. Clair and M. Siochi, 2001.
99. Y. Yang and M. W. Urban, *Adv. Mater. Interfaces*, 2018, **5**, 1800384.
100. M. Zhang, D. Xu, X. Yan, J. Chen, S. Dong, B. Zheng and F. Huang, *Angew. Chem. Int. Ed.*, 2012, **51**, 7011-7015.
101. N. K. Guimard, K. K. Oehlenschlaeger, J. Zhou, S. Hilf, F. G. Schmidt and C. Barner-Kowollik, *Macromol. Chem. Phys.*, 2012, **213**, 131-143.
102. C. M. Dry, 1992.
103. C. M. Dry and N. R. Sottos, 1993.
104. S. R. White, N. R. Sottos, P. H. Geubelle, J. S. Moore, M. R. Kessler, S. Sriram, E. N. Brown and S. Viswanathan, *Nature*, 2001, **409**, 794-797.
105. E. N. Brown, N. R. Sottos and S. R. White, *Exp. Mech.*, 2002, **42**, 372-379.
106. E. N. Brown, M. R. Kessler, N. R. Sottos and S. R. White, *J. Microencapsulation*, 2003, **20**, 719-730.
107. A. S. Jones, J. D. Rule, J. S. Moore, S. R. White and N. R. Sottos, *Chem. Mater.*, 2006, **18**, 1312-1317.
108. A. P. Esser-Kahn, S. A. Odom, N. R. Sottos, S. R. White and J. S. Moore, *Macromolecules*, 2011, **44**, 5539-5553.
109. S. Friedman and Y. Mualem, *Fertil. Res.*, 1994, **39**, 19-30.
110. S. E. Paramonov, E. M. Bachelder, T. T. Beaudette, S. M. Standley, C. C. Lee, J. Dashe and J. M. Fréchet, *Bioconjugate Chem.*, 2008, **19**, 911-919.
111. M. Goldberg and D. M. Kellner, *Journal*, 1993.
112. S.-H. Hu, C.-H. Tsai, C.-F. Liao, D.-M. Liu and S.-Y. Chen, *Langmuir*, 2008, **24**, 11811-11818.
113. A. P. Esser-Kahn, N. R. Sottos, S. R. White and J. S. Moore, *J. Am. Chem. Soc.*, 2010, **132**, 10266-10268.
114. X. Chen, M. A. Dam, K. Ono, A. Mal, H. Shen, S. R. Nutt, K. Sheran and F. Wudl, *Science*, 2002, **295**, 1698-1702.
115. K. S. Toohey, N. R. Sottos, J. A. Lewis, J. S. Moore and S. R. White, *Nat. Mater.*, 2007, **6**, 581-585.
116. N. Roy, B. Bruchmann and J.-M. Lehn, *Chem. Soc. Rev.*, 2015, **44**, 3786-3807.
117. J.-M. Lehn, *Prog. Polym. Sci.*, 2005, **30**, 814-831.
118. J.-M. Lehn, in *Hierarchical Macromolecular Structures: 60 Years after the Staudinger Nobel Prize I*, ed. V. Percec, Springer International Publishing, Cham, 2013, DOI: 10.1007/12_2013_267, pp. 155-172.
119. P. Reutenauer, E. Buhler, P. e. J. Boul, S. e. J. Candau and J. M. Lehn, *Eur. J. Chem.*, 2009, **15**, 1893-1900.
120. W. Alabiso and S. Schlögl, *Polymers*, 2020, **12**, 1660.
121. D. Montarnal, M. Capelot, F. Tournilhac and L. Leibler, *Science*, 2011, **334**, 965-968.
122. T. F. Scott, A. D. Schneider, W. D. Cook and C. N. Bowman, *Science*, 2005, **308**, 1615-1617.

123. Z. P. Zhang, M. Z. Rong and M. Q. Zhang, *Prog. Polym. Sci.*, 2018, **80**, 39-93.
124. C. N. Bowman and C. J. Kloxin, *Angew. Chem. Int. Ed.*, 2012, **51**, 4272-4274.
125. J. M. Winne, L. Leibler and F. E. Du Prez, *Polym. Chem.*, 2019, **10**, 6091-6108.
126. M. Guerre, C. Taplan, J. M. Winne and F. E. Du Prez, *Chem. Sci.*, 2020, **11**, 4855-4870.
127. P. Cordier, F. Tournilhac, C. Soulié-Ziakovic and L. Leibler, *Nature*, 2008, **451**, 977-980.
128. M. Capelot, D. Montarnal, F. Tournilhac and L. Leibler, *J. Am. Chem. Soc.*, 2012, **134**, 7664-7667.
129. R. F. Lange, M. Van Gurp and E. Meijer, *J. Polym. Sci., Part A: Polym. Chem.*, 1999, **37**, 3657-3670.
130. J. Lehn, *Supramol. Chem.*, 1995.
131. D. Montarnal, P. Cordier, C. Soulié-Ziakovic, F. Tournilhac and L. Leibler, *J. Polym. Sci., Part A: Polym. Chem.*, 2008, **46**, 7925-7936.
132. D. Montarnal, F. Tournilhac, M. Hidalgo, J.-L. Couturier and L. Leibler, *J. Am. Chem. Soc.*, 2009, **131**, 7966-7967.
133. S. Uman, A. Dhand and J. A. Burdick, *J. Appl. Polym. Sci.*, 2020, **137**, 48668.
134. M. Guvendiren, H. D. Lu and J. A. Burdick, *Soft matter*, 2012, **8**, 260-272.
135. M. M. Bastings, S. Koudstaal, R. E. Kieltyka, Y. Nakano, A. Pape, D. A. Feyen, F. J. Van Slochteren, P. A. Doevendans, J. P. Sluijter and E. Meijer, *Adv. Healthc. Mater.*, 2014, **3**, 70-78.
136. P. Ren, J. Li, L. Zhao, A. Wang, M. Wang, J. Li, H. Jian, X. Li, X. Yan and S. Bai, *ACS Appl. Mater. Interfaces*, 2020, **12**, 21433-21440.
137. L. Saunders and P. X. Ma, *Macromol. Biosci.*, 2019, **19**, 1800313.
138. M. Nakahata, Y. Takashima, H. Yamaguchi and A. Harada, *Nat. Commun.*, 2011, **2**, 511.
139. M. Burnworth, L. Tang, J. R. Kumpfer, A. J. Duncan, F. L. Beyer, G. L. Fiore, S. J. Rowan and C. Weder, *Nature*, 2011, **472**, 334-337.
140. H. Mohrbach, A. Johner and I. M. Kulić, *Eur. Biophys. J.*, 2012, **41**, 217-239.
141. D. A. Hoey, M. E. Downs and C. R. Jacobs, *J. Biomech.*, 2012, **45**, 17-26.
142. H. Sui and K. H. Downing, *Structure*, 2010, **18**, 1022-1031.
143. E.-M. Mandelkow, R. Schultheiß, R. Rapp, M. Müller and E. Mandelkow, *J. Cell. Biol.*, 1986, **102**, 1067-1073.
144. J. Boekhoven, W. E. Hendriksen, G. J. Koper, R. Eelkema and J. H. van Esch, *Science*, 2015, **349**, 1075-1079.
145. S. Harrisson and K. L. Wooley, *Chem. Commun.*, 2005, 3259-3261.
146. S. Martinotti and E. Ranzato, in *Epidermal cells*, Springer, 2019, pp. 225-229.
147. K. A. Main, C. M. Mikelis and C. L. Doçi, in *Epidermal Cells*, Springer, 2019, pp. 147-154.